RICE UNIVERSITY

Simulation of Dynamics of Radiation Belt Electrons during

Geomagnetic Storms Driven by High Speed Solar Wind Streams
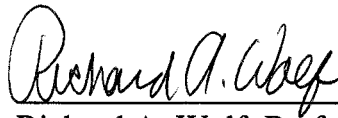

by

Bin Yu

A THESIS SUBMITTED
IN PARTIAL FULFILLMENT OF THE
REQUIREMENTS FOR THE DEGREE

Doctor of Philosophy

APPROVED, THESIS COMMITTEE:

Anthony A. Chan, Associate Professor, Chair
Physics and Astronomy

Richard A. Wolf, Professor Emeritus
Physics and Astronomy

Kartik Mohanram, Assistant Professor
Electrical and Computer Engineering

HOUSTON, TEXAS

April 2007

UMI Number: 3256768

INFORMATION TO USERS

The quality of this reproduction is dependent upon the quality of the copy submitted. Broken or indistinct print, colored or poor quality illustrations and photographs, print bleed-through, substandard margins, and improper alignment can adversely affect reproduction.

In the unlikely event that the author did not send a complete manuscript and there are missing pages, these will be noted. Also, if unauthorized copyright material had to be removed, a note will indicate the deletion.

UMI®

UMI Microform 3256768

Copyright 2007 by ProQuest Information and Learning Company.

All rights reserved. This microform edition is protected against unauthorized copying under Title 17, United States Code.

ProQuest Information and Learning Company
300 North Zeeb Road
P.O. Box 1346
Ann Arbor, MI 48106-1346

ABSTRACT

Simulation of Dynamics of Radiation Belt Electrons during Geomagnetic Storms

Driven by High Speed Solar Wind Streams

by

Bin Yu

Satellite observations have shown that fluxes of relativistic electrons in the earth's radiation belts can vary by orders of magnitude during periods of high solar activity. Understanding the dynamic behavior of these particles is very important because they can disrupt wireless communication, impair space exploration and affect GPS navigation.

We use two numerical methods to simulate the variations of energetic particles in the radiation belts. First, we develop a radial diffusion model with time-dependent boundary conditions and a *Kp*-dependent electron lifetime model. Using this model, we simulate a series of high-speed-stream declining-phase magnetic storm events. The results are consistent with spacecraft observations and show that radial diffusion can propagate the enhancement of phase space density from the outer boundary into the center of the outer radiation belt. The second part of the work adapts Nunn's Vlasov Hybrid Simulation method to an existing MHD-Particle simulation code, resulting in an efficient new method to calculate phase space density of energetic particles. We use the 1995 January storm event as a test case. Good agreement is obtained between the simulation results and measured phase space densities for this event. Simulating the dynamics of the radiation belts is one important part of global space weather modeling. The advance in

radiation belt modeling can help us to better understand the physics behind these interesting and important phenomena.

Acknowledgments

I would like to express my deep gratitude to my advisor Prof. Anthony Arthur Chan whose guidance, encouragement and kind support helped me in all the time of research for and writing of this thesis. I also want to express my gratefulness to Prof. Richard A. Wolf for his creative idea and significant contributions to this research work. Particular thanks to Scot R. Elkington for the collaborations and valuable discussions.

I also wish to thank Bonnie Hausman, Stanislav Sazykin, and Bob Spiro for their support of the simulation data. I wish to thank the faculty members and students in the magnetospheric theory group of Rice University, especially Yue Fei for the help with the coding and Xin Tao for polishing this thesis.

Sincerely thanks also to the following people: J. M. Albert for many helpful discussions and comments; Xinlin Li for his assistance with the outer boundary conditions; Jichun Zhang for his valuable discussion on SWMF; Kartik Mohanram for the service on the committee.

Also thanks to my wife and parents for supporting me through the past few years. Without them, this research work would even not be possible.

Contents

Abstract

Acknowledgments

Contents

Figures

Table

Figures

Table

Chapter 1

Introduction

In this thesis, a new radial transport model and a novel particle simulation method have been developed to simulate radiation belt dynamics. The Radiation belts are also called the Van Allen belts after their discoverer, James Van Allen. In early 1958, based on the measurements on satellites Explorer I and III he found a region of trapped high energy particles surrounding the earth, which was later named the inner radiation belt [*Van Allen et al.,* 1959; *Van Allen* and *Frank,* 1959]. Several months later, in December 1958, satellite Pioneer 3 detected the existence of another wider and more dynamic belt of energetic plasma, which is called the outer radiation belt. Soon after that, in 1959, another satellite Pioneer 4 confirmed the existence of the outer radiation belt.

Figure 1.1 is a schematic illustration of the radiation belts, which can be divided into two regions: the inner radiation belt and the outer radiation belt. The inner radiation belt is closer to the earth, ranging from 1.1 to 2.5 earth radii, and contains high intensity of protons with energies exceeding 100 MeV. The inner radiation belt is usually very stable and does not dramatically change during high solar activity. The outer radiation belt extends from 3 to 10 earth radii and mainly contains electrons with energies from a few hundred KeV to 10 MeV. In contrast to the inner radiation belt, the fluxes of these electrons in the outer radiation belt are more dynamic and can increase several orders of magnitude during large magnetic storms. The gap region between the inner radiation belt and outer radiation belt is usually considered to be the result of the pitch angle scattering of particles into the atmosphere by very low frequency (VLF) waves in the earth's magnetosphere.
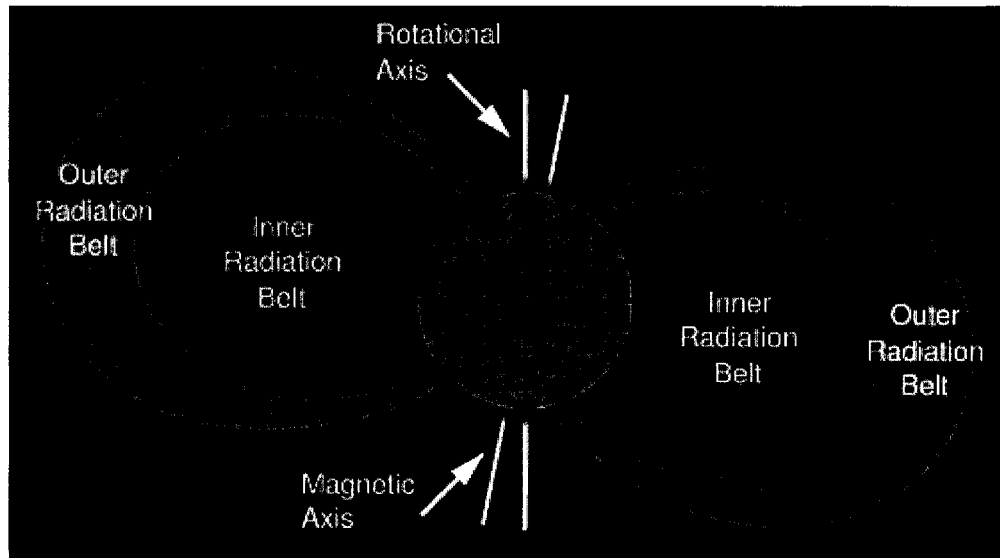
Figure 1.1 The schematic illustration of the radiation belts [from *Wikipedia*, the free encyclopedia].

Since the discovery of the radiation belts, the study of the fluxes of the energetic trapped particles has become an important topic in space physics. As human activities in space advance, more attention has been given to the variation of high energy electrons during geomagnetic storms. These high energy electrons are often called "killer electrons" since they constitute a threat to space exploration. These electrons can damage spacecraft instruments, cause operational problems and even cause complete loss of contact with spacecraft. Their high radiation is also very dangerous to astronauts. Some interesting statistical results show a possible relationship between the long-term changes of the climate and the outer belt electron precipitation [*Shirochkov A.V.* and *L. N. Makarova.*, 2006].

In this research work, we simulate the dynamics of energetic electrons in the outer radiation belt during high-speed-stream solar wind (a stream of electrified gas) events, using a new radial

transport model and a novel particle simulation method. We will show that reasonable agreement between the observations and simulated results can be obtained with these models.

Chapter one provides background information on space physics, including but not limited to a brief description of some of the phenomena and underlying physics in the field of radiation belt research. This chapter begins with an introduction to the earth's electric and magnetic fields and related topics, proceeds to a description of the motion of radiation belt particles trapped in the earth's magnetosphere, and finally reviews the history of efforts at modeling the radiation belts.

In chapter two, we focus on the introduction of our new radial transport model. In addition, we construct a model storm based on measurements and discuss the efficiency of the model storm in reproducing the characteristics of real high-speed-stream storm events. A series of test cases between 1995 and 1996 are used to study the effects of radial transport coefficients and the underlying magnetic field models.

A new MHD-Particle simulation method is presented in chapter three. By making more efficient use of the test particles, we successfully enhance the computational performance of traditional MHD-Particle simulation codes. Taking the January 1995 storm event as a test case, we show that both dynamic outer boundary conditions and a realistic lifetime model of energetic electrons are needed to capture the observed features of these electrons during this storm event. Finally, we calculate the diffusion coefficients from the power-spectrum obtained from global MHD simulations and rerun our radial transport model described in chapter two with the new diffusion coefficients.

Finally, in chapter four, we summarize the benefits and limitations of the two numerical methods and discuss possible future work in radiation belt studies.

1.1 The earth's magnetosphere

The earth's magnetosphere is the region of space which is dominated by the magnetic field of the earth. The magnitude and shape of the field are primarily controlled by the interaction of the earth's magnetic field and solar wind streams, which consist of fully-ionized plasma emitted from the sun. The earth's interior magnetic field is generated from electric currents in the earth's core. The inner part of the magnetic field of the magnetosphere is roughly dipolar with an intensity of 0.31 Gauss near the surface of the earth at the equator plane. However, over the region near the outer boundary of the magnetosphere, the dipole-like shape is highly distorted by the solar wind, especially during the period of geomagnetic storms.

The sun often ejects large numbers of hot charged particles from its surface. These particles, which form the solar wind, are frozen in the interplanetary magnetic field (IMF) and can travel with the IMF in all directions. If the direction is toward the earth, the solar wind will strike the earth's magnetosphere in a few days with an average velocity of 450 km/s and typical number density of 3~5 cm^{-3}. As a result, the dynamic pressure carried by the solar wind compresses the earth's magnetosphere on the dayside and deforms the magnetosphere. It is also believed that a large amount of energy is injected into the magnetosphere through the reconnection of the southward IMF and the geomagnetic field during geomagnetic storms.

Figure 1.2 illustrates the structure of the earth's magnetosphere. The supersonic solar wind stream forms a collisionless shock wave known as the bow shock in front of the magnetosphere. On the down stream side of the bow shock is the magnetosheath, which is a region filled with hot subsonic plasma. The outer boundary of the earth's internal magnetic field is called the magnetopause. Most of the hot plasma in the magnetosheath compresses the magnetopause on

the dayside and then flows around the magnetic obstacle. However, some of the plasma can leak into the inner part of the magnetosphere through the two polar cusps.

Inside the magnetopause, the inner magnetosphere can be divided into different plasma regions according to the characteristics (e.g., density, energy, flow direction, and species) of the plasma present. A variety of current systems can contribute to the configuration of the geomagnetic field. The magnetopause current, which is also known as the Chapman-Ferraro current, flows along the magnetopause eastward and separates the magnetic field of solar-origin from the earth's magnetic field. The dawn-dusk cross-tail current is another important current system which divides the magnetic tail into two lobes. The partial or closed ring current flows westward around the earth. It typically builds up during the main phase of a magnetic storm and decays to normal level during the recovery phase. The field-aligned current connects the high latitude auroral zone to the outer plasma sheet and the boundary layers.
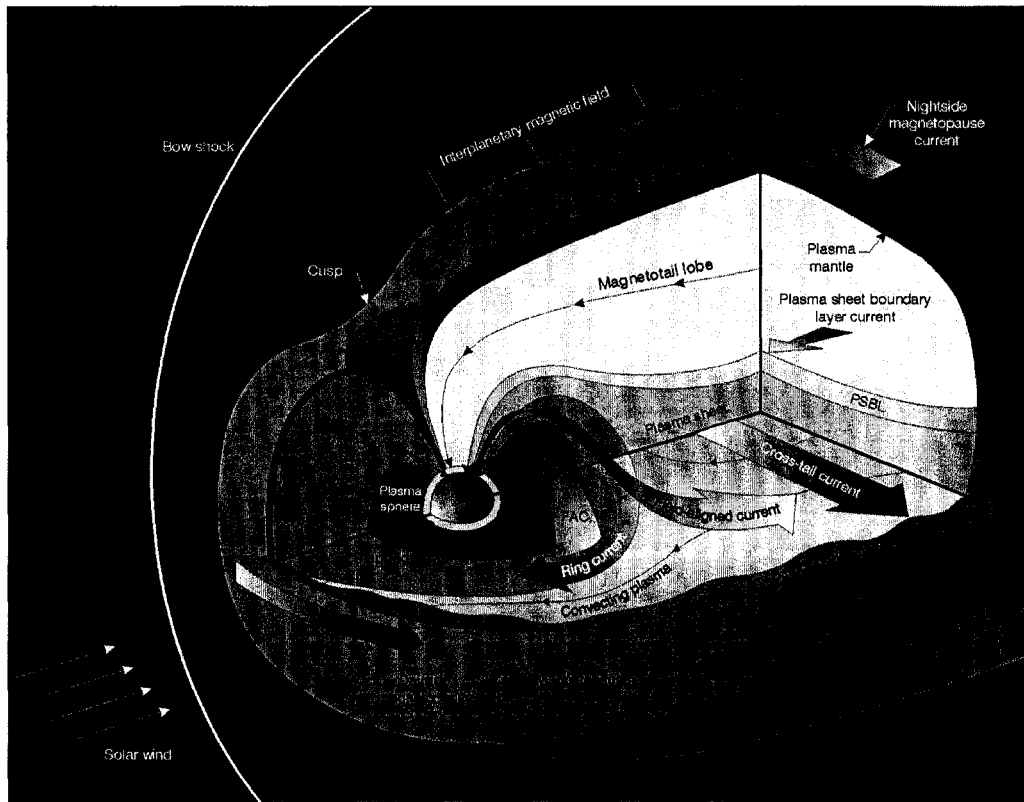
Figure 1.2 The earth's magnetosphere [*Jichun Zhang*, 2006].

1.2 Geomagnetic storms

The magnetosphere is highly dynamic and its structure often varies with solar activity. Even long before the space age, ground measurements had indicated the worldwide magnetic perturbations after some large solar flares. Based on these observations, the concept of the "geomagnetic storm" was introduced. A geomagnetic storm may be defined as the temporary fluctuation of magnetospheric electric and magnetic fields caused by the solar activity.

Figure 1.3 shows a typical magnetic storm event in September 1998 [*Fei Yue*, 2006]. In this figure, the magnetic activity index *Dst* represents the hourly average variations of the southward component of the magnetic field on the ground and is associated with the intensity of the

magnetospheric ring current. A classical magnetic storm usually begins with the sudden increase of the *Dst* index, which is known as a "sudden storm commencement (SSC)" and is usually due to the compression of the magnetic field by enhanced solar wind pressure. Following the SSC, some storm events can maintain a strengthened field for hours, a period that is called the "initial phase". After the initial phase, the storm enters the main phase. The *Dst* index decreases sharply within several hours to one day, indicating the intensification of the ring current. The *Dst* index then gradually returns to the pre-storm level over a period of tens of hours to a week. During this recovery phase, the ring current particles gradually decay to normal levels through various loss processes. In this storm, the minimum *Dst* of -200 nT indicates it is a major storm. Table 1.1 shows the relationship between the minimum *Dst* index and the storm strength.
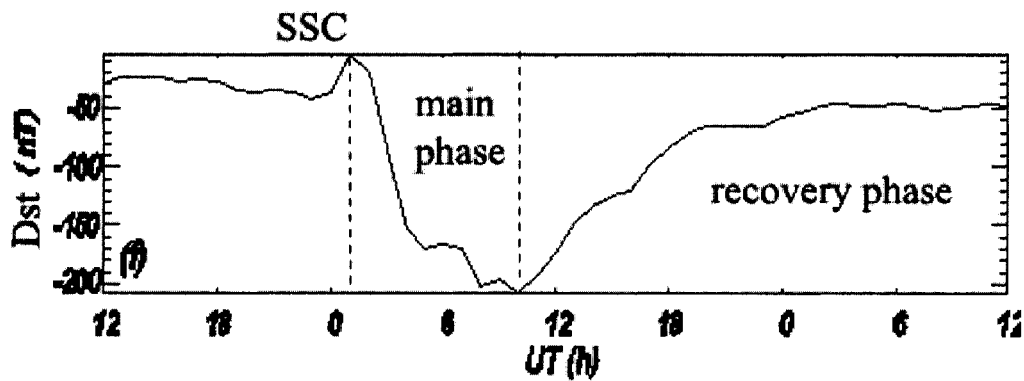
Figure 1.3 A typical major magnetic storm during September 24-26, 1998 [*Fei Yue*, 2006].

There are two specific types of storm events: storms driven by coronal mass ejections (CME storms) and storms driven by corotating interaction regions (CIR storms). The CME storms mostly occur close to the solar maximum and may contain a magnetic cloud. CME storms are more efficient at producing large *Dst* perturbations and can cause some large or even extreme

storm events [*J. E. Borovsky* and *M. H. Denton*, 2006]. In contrast, CIR storms are driven by the high speed solar wind streams associated with coronal holes. CIR storms are usually small or moderate, but can produce high fluxes of energetic electrons due to the long-lasting interaction between the fast solar wind streams and the magnetosphere. This research work focuses on the CIR storm events. In the subsequent chapters, we will present a model of CIR storm events and simulate the corresponding variations of radiation belt particles using a new radial transport model and a novel MHD-particle code.

Magnetic Storm Level	Dst index
Extreme	<-100 nT
High	-50 ~ -100 nT
Moderate	-20 ~ -50 nT
Small	>-20 nT

Table 1.1 The relationship between the magnetic storm level and *Dst* index [from *sprg.ssl.berkeley.edu/dst_index*].

1.3 The motion of charged particles in the magnetosphere

According to the Lorentz force equation, the motion of individual charged particles in given electric and magnetic fields can be described as:

$$\frac{d\vec{p}}{dt} = q\vec{E} + q\vec{v} \times \vec{B} . \qquad (1.1)$$

Here, $\vec{p}$ denotes the relativistic momentum, which is equal to $\gamma m \vec{v}$ and $\gamma = \dfrac{1}{\sqrt{1 - \dfrac{v^2}{c^2}}}$ is the

Lorentz factor.

Starting from this equation, assuming the magnetic field is homogenous and constant and no external electric field exists, the particle, whose pitch angle (the angle between the particle velocity and the local magnetic field) is near 90^0, will gyrate around the "guiding center" on the

magnetic field line with the gyration period $T = \dfrac{2\pi \gamma m}{B|q|}$ and the gyroradius $\rho = \dfrac{\gamma m v_\perp}{B|q|}$.

In the magnetosphere, the motion of a charged particle can be decomposed into the quick gyration around the guiding center and the drift motion of the guiding center itself. In general, the motion of the guiding center in the direction perpendicular to the magnetic field consists of the following three kinds of drift motions:

1) " $E \times B$ " drift motion, $\vec{V}_E = \dfrac{\vec{E} \times \vec{B}}{B^2}$, which is independent of the charge or energy of the

particle;

2) "gradient" drift motion, $\vec{V}_{grad} = \dfrac{\gamma m v_\perp^2}{2qB^3}(\vec{B} \times \nabla B)$;

3) "curvature" drift motion, $\vec{V}_{curv} = \dfrac{\gamma m v_{//}^2}{qB^3}(\vec{B} \times \dfrac{\partial \vec{B}}{\partial s})$; if $\nabla \times B = 0$, $\vec{V}_{curv} = \dfrac{\gamma m v_{//}^2}{qB^3}(\vec{B} \times \nabla B)$.

Here, $v_{//}$ represents the velocity parallel to the local magnetic field, $v_\perp$ is the perpendicular component of the total velocity, s is the distance along a magnetic field line.

In sum, the perpendicular component of the velocity of the "guiding center" can be described by the following equation:

$$\vec{V}_{GC\perp} = \vec{V}_E + \vec{V}_{grad} + \vec{V}_{curv} . \qquad (1.2)$$

It should be recognized that equation (1.2) is based on the assumption $\rho_{gyro}\dfrac{|\nabla B|}{B} \ll 1$, which is normally true for the particles in the outer radiation belt. Usually, for high energy particles in the radiation belt, $\vec{V}_{grad}$ and $\vec{V}_{curv}$ are the larger terms. The electric field drift motion, $\vec{V}_E$, is more important for low energy particles.

The parallel velocity of the "guiding center" can be approximated using the following equation:

$$\frac{dv_{GC//}}{dt} = -\frac{1}{2}\frac{v_\perp^2}{B^2}(\nabla B \bullet \vec{B}) . \qquad (1.3)$$

Equation (1.3) shows that for the parallel motion, the particle will be accelerated in a direction opposite to the gradient of the magnetic field. As a result, the "mirror force" tends to repel particles out of a region that has a stronger field, causing the bounce motion of trapped particles along the magnetic field line.

Combining the gyration around the "guiding center" and the motion of the "guiding center" itself, the orbits of trapped particles in the magnetosphere can be divided into three types of motion with distinct time periods, as illustrated in figure 1.4.
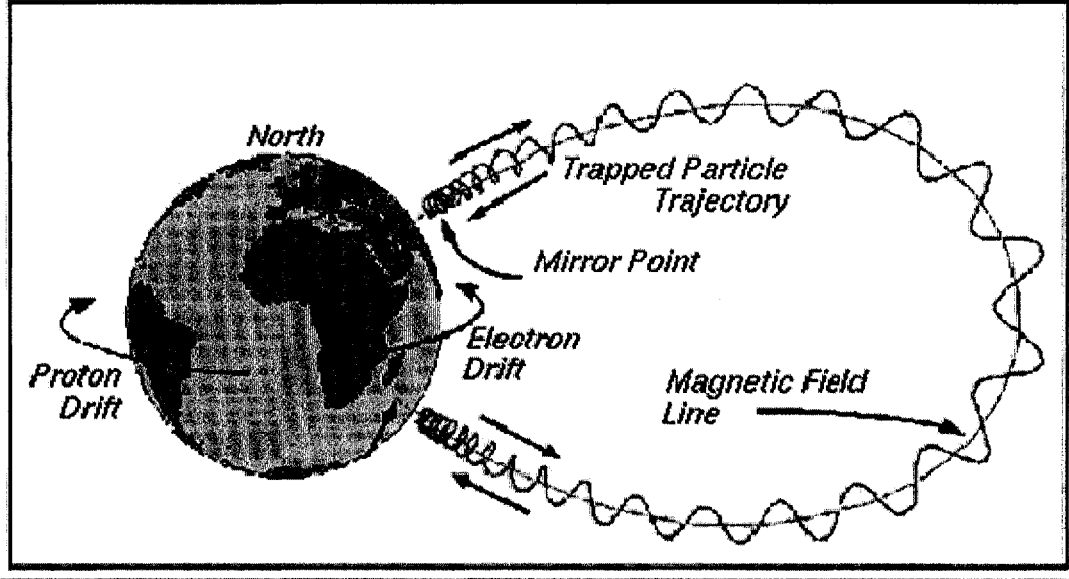
Figure 1.4 The motion of trapped particles in the magnetosphere [*Tascione*, 1988].

As sketched in figure 1.4, the overall motion of trapped particles includes gyration around the guiding center on magnetic field lines, bouncing between the two mirror points along magnetic field lines, and drifting around the earth. For MeV electrons, the typical time periods for the three kinds of motion are: milliseconds for the gyration, 0.1~1.0 second for the bounce motion, and roughly 1~10 minutes for the drift motion.

To quantitatively describe the motion of trapped particles, the concept of "adiabatic invariants" is introduced. Three invariants are associated with the three types of motion. Their values will be conserved if the earth's electric and magnetic fields change slightly over the period of the corresponding motion. The origin definition of an invariant is the integral of the canonical momentum over a periodic orbit [e.g., *Walt*, 1994]:

$$J_i = \frac{1}{2\pi} \oint (\vec{p} + q\vec{A}) \bullet d\vec{l} , \qquad i = 1,2,3 \qquad (1.4)$$

where $\vec{l}$ is the trajectory of the corresponding motion, $\vec{A}$ is the vector potential of the magnetic field, and $\vec{p} + q\vec{A}$ represents the canonical momentum.

However, it is usually more convenient to use the following new variables rather than J_i:

First invariant $$M = \frac{q}{m} J_1 = \frac{p_\perp^2}{2mB} \ , \qquad\qquad (1.5)$$

Integral invariant $$I = \frac{J_2}{2p} = \int_{sm1}^{sm2} \sqrt{1 - \frac{B(s)}{B_m}} ds \ , \qquad\qquad (1.6)$$

Magnetic flux $$\Phi = \frac{J_3}{q} = \oint \vec{B} \bullet d\vec{S} \ . \qquad\qquad (1.7)$$

Here s is the length along the magnetic field line, $sm1$ and $sm2$ are two mirror points specified in figure 1.4, $d\vec{S}$ is an element of the surface enclosed by the equatorial drift shell, and Φ represents the magnetic flux enclosed by the longitudinal drift motion of trapped particles.

The first invariant is associated with the gyration of particles and is conserved if the electric and magnetic fields change on a time scale compared to the gyroperiod. Since in the gyration, the direction of the force is always perpendicular to the direction of the velocity if the electric field is zero, the energy is conserved, meaning p^2 is constant. If a particle moves along the field line toward the earth, the intensity of the field increases. According to equation (1.5), $p_\perp^2$ must also increase to conserve M. Hence, $v_{//}$, the parallel velocity decreases. At the mirror point, the parallel velocity decreases to zero and the particle is reflected. Another important application of the first invariant is in tracing the longitudinal drift paths of equatorially trapped particles. If the electric field and so-called Shabansky orbit [*Shabansky*, 1970] can be ignored and the first

invariant is conserved along their trajectories, these particles will drift along contours of constant B, which will be discussed in appendix A in more detail.

The integral invariant associated with the bounce motion is very useful in defining the drift path of trapped particles. Under the condition that the integral invariant is conserved, the guiding center drift path is closed since at a given longitude I is a monotonic function of R, the distance from the center of the earth.

For the third invariant, it is usually not practical to directly calculate the flux enclosed by the drift shell due to the large and uncertain magnetic fields at the center of the earth. Instead, the flux outside the drift shell is integrated since it is equal to the flux inside the path (refer to appendix A for more details).

Magnetic flux is most useful to describe the drift path when the magnetic field does not have dramatic changes over the drift period. In this situation, the magnetic flux is invariant. As a response to the slow change of the geomagnetic field, the particles have to move in the radial direction to conserve the enclosed magnetic flux.

In addition to magnetic flux, another convenient variable, the Roederer L value, is also used in the study of radiation belt particles [*Roederer*, 1970]. The Roederer L value, which is associated with the drift motion of the particles in the geomagnetic field, is defined as

$$L^* = \frac{2\pi B_E R_E^2}{\Phi} ,$$

(1.8)

where B_E is the magnetic field at the earth's equator and roughly equals to 0.317 Gauss, and R_E is the earth's radius. For a dipolar magnetic field, the value of L^* is equal to the distance in earth

radii from the center of the earth to the equatorial crossing point of the field line. In this thesis, unless specifically noted, we use L rather than L^* for the Roederer L value.

1.4 Fluxes of particles & phase space density

In section 1.3, we described the motions of individual charged particles in the magnetosphere. However, this is not enough to represent the global characteristics of the radiation belt particles. The relevant concepts of particle fluxes and phase space density will be introduced in this section.

Many fluxes are used in the study of radiation belt particles. The basic one is the differential, directional flux, which is expressed as the function of location, energy and direction $j(E,\alpha)$ and is written in units of $cm^{-2}s^{-1}str^{-1}KeV^{-1}$. The exact definition of the differential, directional flux is:

$$dN(\vec{r},E,\alpha) = j(E,\alpha)dAdEd\Omega. \qquad (1.9)$$

Here α is the pitch angle, dA is the unit area, dE is the energy interval at energy E, $d\Omega$ is the unit solid angle in the α direction, and dN represents the number of particles with energies between E and $E+dE$ passing through dA in the α direction within $d\Omega$ solid angle in 1 second [e. g., Walt, 1994]. Figure 1.5 illustrates the definition of the differential, directional fluxes.
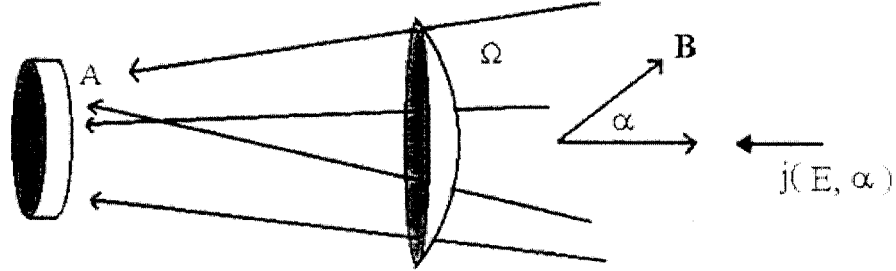
Figure 1.5 Diagram of the definition of the differential flux [from *galileo.ftecs.com*].

Two other important fluxes are defined as follows:

Energy Integral flux $\quad j(\alpha, E > E_0) = \int_{E_0}^{\infty} j(E,\alpha)dE$ $\qquad$ (1.10)

Omnidirectional flux $\quad j(E) = \int_{\Omega} j(E,\alpha)d\Omega = \int_{0}^{\pi} j(E,\alpha)2\pi\sin\alpha d\alpha$ $\qquad$ (1.11)

In addition to the above fluxes, another convenient variable used to designate distributions of trapped particles in the radiation belt is the phase space density (*PSD*). The phase space density is the number of particles per unit volume of six-dimensional phase space $f(\vec{r},\vec{p})$. The phase space density is closely related to the differential flux through the following equation:

$$f(\vec{r},\vec{p}) = \frac{j(E,\alpha)}{p^2}.$$ $\qquad$ (1.12)

There are many benefits describing the particle distributions in term of phase space density rather than the fluxes. One of them is that the phase space density is conserved along the trajectory of a particle according to Liouville's theorem. The following equation represents the theorem derived by Liouville:

$$\frac{df(\vec{r},\vec{p},t)}{dt} = \frac{\partial f}{\partial t} + \sum_{i=1}^{3} \frac{\partial f}{\partial r_i} \dot{r}_i + \sum_{i=1}^{3} \frac{\partial f}{\partial p_i} \dot{p}_i = 0. \qquad (1.13)$$

1.5 Diffusion theory and particle transport

As mentioned at the beginning of this chapter, the outer radiation belt is very dynamic and is controlled by solar activity. During some magnetic storms, fluxes of high energy electrons can vary by factors of several hundred.

Figure 1.6 plots the *Dst* index variations during one magnetic storm event in November 1993 and the corresponding flux changes for electrons of different energy levels. From this figure, we see that the electron fluxes for all four energy channels decreased during the main phase and increased up to 2 orders of magnitude over the pre-storm level during the recovery phase. Another obvious feature of figure 1.6 is the similarity between the variations of *Dst* index and the changes of electron fluxes. This is called the "Dst Effect" and is caused in part by the adiabatic response of relativistic electron fluxes to the dynamics of the magnetosphere during storm time.
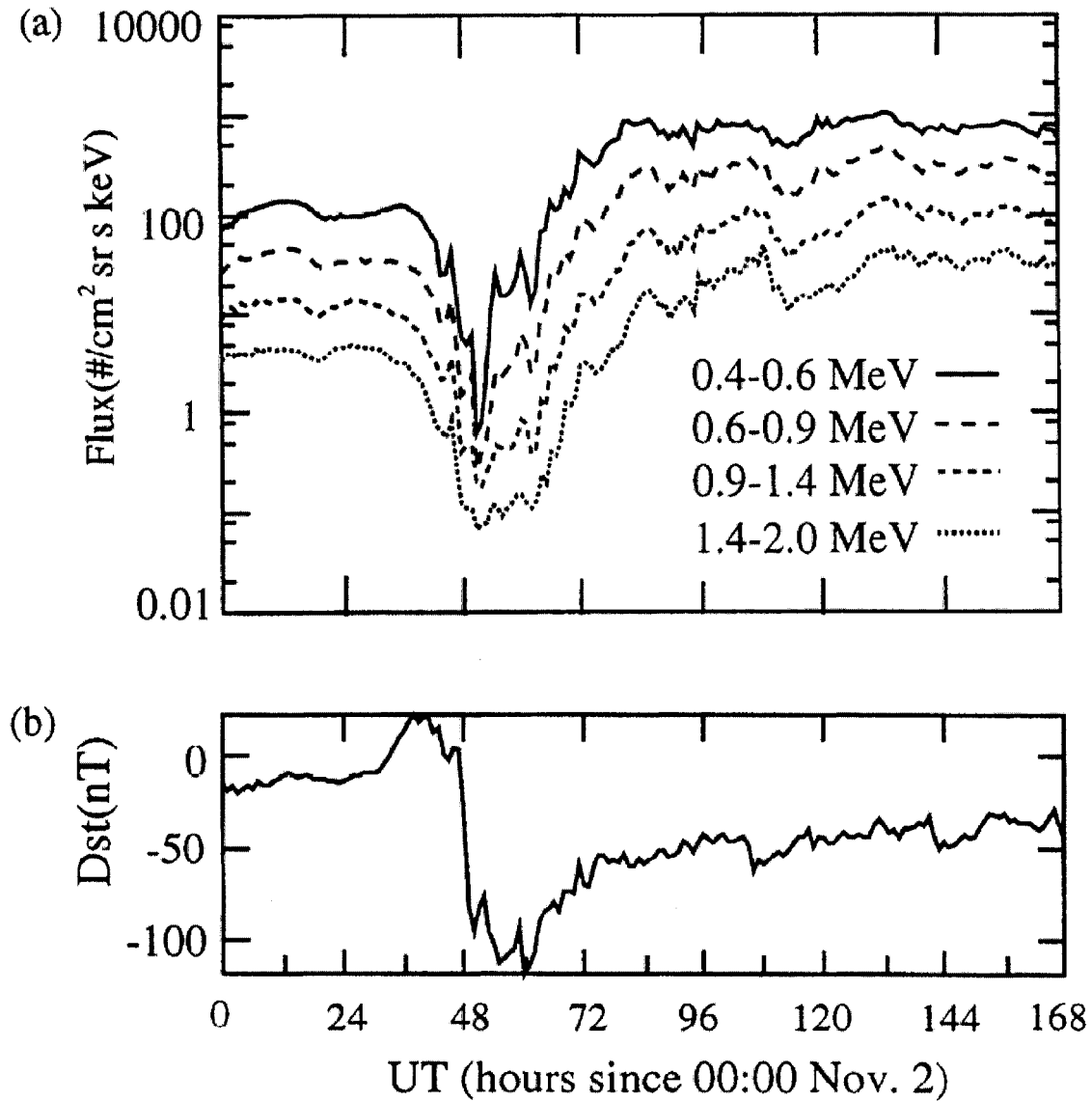
Figure 1.6 (a) Hourly average variations of the electron fluxes at geosynchronous orbit (R=6.6 R_E) for November 2~8, 1993, measured by the satellite LANL 1984-129; (b) the variations of *Dst* index for the same time period. [*H.J.Kim* and *A.A.Chan*, 1997].

Recently much attention has been given to different mechanisms responsible for the variations of high energy electrons. One important method, quasilinear diffusion theory, describes the time evolution of phase space density when one or more adiabatic invariants have

been violated. Particle transport due to the diffusion can be represented by the following Fokker-Planck equation [*Haerendel*, 1968]:

$$\frac{\partial f}{\partial t} + \sum_i \frac{\partial}{\partial J_i}[\Gamma_i f] = \sum_{i,j} \frac{\partial}{\partial J_i}\left[D_{ij}\frac{\partial f}{\partial J_j}\right] - \frac{f}{\tau} + S, \qquad (1.14)$$

where the second term on the left side stands for the coherent term, for example, a friction term, which is usually ignored in this research work. On the right side, the first term represents the diffusion term, and D_{ij} are diffusion coefficients; the loss and source terms are also included as the second and the third terms, and τ represents an average lifetime of energetic particles in the radiation belt.

As described previously, the period of longitudinal drift motion is much longer than the gyration and bounce motion. Therefore, the third invariant is more easily broken by fluctuations of fields. Assuming the first and the second invariants are conserved and only the third invariant is violated, the particles will only diffuse in the radial direction. This type of diffusion is termed "radial diffusion" and the Fokker-Planck equation can be simplified to the following equation:

$$\frac{\partial f}{\partial t} = L^2 \frac{\partial}{\partial L}\left(\frac{D_{LL}}{L^2}\frac{\partial f}{\partial L}\right) - \frac{f}{\tau} + S. \qquad (1.15)$$

Here L is the Roderer L; the radial diffusion coefficient $D_{LL} = \frac{\langle (\Delta L)^2 \rangle}{2}$ represents the rate of the radial transport and the bracket in the definition of D_{LL} denotes the averaged time rate of change in the squared increments of L.

1.6 Wave-Particle interactions

A variety of electromagnetic waves exist throughout the magnetosphere. These waves can have important effects on the distribution of the trapped particles. Assuming the wave growth rate is much less than the real wave frequency, the general local resonance relation between the waves and particles can be expressed as [*Kennel* and *Englemann*, 1966]

$$\omega - k_{//}v_{//} + m\Omega = 0. \qquad\qquad (1.16)$$

Here ω is the wave angular frequency, $k_{//}$ is the component of wave vector $\vec{k}$ along the local magnetic field direction, Ω is the gyro frequency, and ω and $\vec{k}$ can be related by a plasma dispersion equation.

In this research work, two types of waves, ultra low frequency waves (ULF waves) and very low frequency waves (VLF waves), are of particular importance. ULF waves, which have the same frequency range (~mHz) as the particles' drift frequencies, are directly relevant to the radial diffusion rate of the particles. During some magnetic storms, the enhancement of the power spectrum of ULF waves leads to the increase of the radial diffusion coefficients. This results in the quick redistribution of the particles from the outer boundary to the inner magnetosphere. In addition, these particles are accelerated by radial diffusion; hence the interactions between ULF waves and particles provide an external source acceleration mechanism.

Another important type of wave, VLF waves, has frequencies ranging from 0.3 to 3KHz. Through cyclotron-resonant interaction with particles, VLF waves can change the pitch angles of the particles. This process is called "pitch-angle diffusion" and plays an important role in the

precipitation of the particles into the atmosphere. In addition, recent observational evidence indicates that particles within geosynchronous orbit can be accelerated to relativistic energies by VLF wave-particle interactions, and then are redistributed through inward or outward diffusion processes [*Miyoshi et al.,* 2003; *Meredith et al.,* 2003]. Hence, VLF waves provide another important acceleration source, a local acceleration source.

1.7 Modeling the radiation belt

Since the discovery of the radiation belts, considerable effort has been invested in developing empirical and physical radiation belt models.

In the early 1970s, the NASA AE8/AP8 model was developed. This model is based on measurements collected by more than 20 satellites from the early sixties through the mid-seventies of the 20th century and can provide omnidirectional, integral fluxes of protons within the energy range of 0.1~400 MeV and electrons within the energy range of 0.04~7 MeV in the radiation belts. However, these empirical models can only provide time-averaged fluxes of these particles, a dynamic radiation belt model is needed for accurate predictions of the fluxes of particles during geomagnetic storms. Several approaches have been used to reproduce the dynamic characteristics of radiation belt particles. Some semi-empirical models applied linear and nonlinear filter techniques [*Vassiliadis et al.,* 2002; *Rigler et al.,* 2004] or neural networks [*Koons* and *Gorney,* 1991] to reproduce the observed spatial and temporal variations. The study on the radial diffusion process provides one important numerical method to simulate variations of radiation belt particles by solving equation (1.15). This will be discussed in chapter 2 in more detail [*Brautigam* and *Albert,* 2000; *Fok et al.,* 2001; *Fei et al.,* 2006]. Another important method,

MHD-Particle simulation, is used to trace the paths of the "guiding center" of particles in the

global MHD magnetic fields; this will be fully described in chapter 3 [*Hudson et al.*, 1996;

Elkington et al., 2002].

References

Borovsky, J. E., and M. H. Denton (2006), The differences between CME driven storms and CIR-driven storms, *J. Geophys. Res., 111,* A07S08.

Brautigam, D. H. and J. M. Albert (2000), Radial diffusion analysis of outer radiation belt electrons during the October 9, 1990, magnetic storm, *J. Geophys. Res., 105(A1),* 291.

Elkington, S.R., Hudson, M.K., Wiltberger, M.J., Lyon, J.G. (2002), MHD/Particle simulations of radiation belt dynamics, *Journal of Atmospheric and Solar Terrestrial Physics, 64,* 607.

Fei, Y. (2006), *Simulation of Radiation Belt Electron Diffusion,* Ph.D thesis.

Fei, Y., Chan, A.A., Elkington, S.R., Wiltberger, M.J. (2006), Radial diffusion and MHD particle simulations of relativistic electron transport by ULF waves in the September 1998 storm, *J. Geophys. Res., 111,* A12209.

Fok, M.C., Moore, T.E., Spjeldvik, W.N. (2001), Rapid enhancement of radiation belt electron fluxes due to substorm depolarization of the geomagnetic field, *J. Geophys. Res., 106(A3),* 3873.

Haerendel, G. (1968), *Diffusion theory of trapped particles and the observed proton distribution,* Reinhold, New York and London.

Hudson, M.K., Elkington, S.R., Lyon, J.G., Marchenko, V.A., Roth, I., Temerin, M., Gussenhoven, M.S. (1996), MHD/ Particle simulations of radiation belt formation during a storm sudden commencement. In: Lemaire, J.F., Heynderickx, D., Baker, D.N. (Eds.), Radiation Belts: Models and Standards, vol. 97. AGU, Washington, DC, p. 57.

Kennel, C. F. and F. Engelmann (1966), Velocity space diffusion from weak plasma turbulence in a magnetic field, *phys. Fluids, 9,* 2377.

Kim, H. J., and A. A. Chan (1997), Fully adiabatic changes in the storm time of relativistic electron fluxes, *J. Geophys. Res., 102,* 22107.

Koons, H.C., Gorney, D.J. (1991), A neural network model of the relativistic electron flux at geosynchronous orbit, *J. Geophys. Res, 96 (A4),* 5549.

Meredith, N. P., M. Cain, R. B. Horne, D. summers, B. J. Fraser, and R. R. Anderson (2003), Evidence for chorus-driven electron acceleration to relativistic energies from a survey of geomagnetically disturbed periods, *J. Geophys. Res., 108,* 1248.

Miyoshi, Y., a. Morioka, T. Obara, H. Misawa, T. Nagai, and Y. Kasahara (2003), Rebuilding process of the outer radiation belt during the 3 November 1993 magnetic storm: NOAA and Exos-D observations, *J. Geophys. Res., 108(A1),* 1004.

Rigler, E.J., Baker, D.N., Weigel, R.S., Vassiliadis, D., Klimas, A.J. (2004), Adaptive linear prediction of radiation belt electrons using the Kalman filter. *Space Weather 2* (S03003).

Roederer, J.G. (1970), *Dynamics of Geomagnetically Trapped Radiation,* Springer-Verlag.

Shirochkov, A.V., and L. N. Makarova (2006), Peculiarities of Long-Term Trends of Surface Temperature in Antarctica and Their Possible Connections with Outer Belt Electron Precipitation, *4th IAGA/ICMA/CAWSES Workshop "Long-Term Changes and Trends in the Atmosphere".*

Tascione, T. F. (1988), *Introduction to the Space Environment,* Orbit Book Company, Malabar, Florida.

Van allen , J. A., C. E. McIlwain, and G. H. Ludwig (1959), Radiation observations with satellite 1958 Epsilon, *J. Geophys. Res., 64,* 271.

Van allen , J. A., and L. A. Frank (1959), Radiation Around the Earth to a radial distance of 107,400 km, *Nature, 183,* 430.

Vassiliadis, D., Klimas, A. J., Kanekal, S. G., Baker, D. N., and Weigel, R. S. (2002), Long-term-average, solar cycle, and seasonal response of magnetospheric energetic electrons to the solar wind speed *J. Geophys. Res., 107 (A11),* 506.

Vette, J. (1991), *The AE-8 trapped electron model environment, National Space Science Data Center,* Report 91-24, Greenbelt, Maryland.

Walt, M. (1994), *Introduction to Geomagnetically Trapped Radiation,* Cambridge University Press.

Chapter 2

Radial Diffusion Model & Case Studies: Geomagnetic Storms Driven by High Speed Streams

2.1 Introduction

During the declining phase of the solar cycle, coronal holes can give rise to high-speed solar wind streams with 27-day periodicity. These high-speed stream structures in the solar wind result in recurring weak-to-moderate magnetospheric storms with substorm activity that can last for several days [*Tsurutani et al.*, 1995] and can generate large, sustained increases in radiation belt electron fluxes [e.g., *Paulikas and Blake*, 1979; *Baker et al.*, 1997].

Previous diffusion modeling efforts have concentrated on simulating the dynamics of radiation belt electrons during strong CME storms [e.g., *Bourdarie et al.*, 1996; *Brautigam and Albert*, 2000]. However, less attention has been given to the enhancements of MeV electron flux in the center of the outer radiation belt (~4 R_E) during moderate to weak storms driven by high-speed streams.

To identify specific mechanisms responsible for these enhancements, we constructed a radial diffusion model which uses a time-dependent radial diffusion coefficient parameterized by *Kp* from *Brautigam and Albert* [2000], a solar-wind-controlled geosynchronous orbit outer boundary condition from *Li et al.* [2001], and a *Kp*-dependent dynamic loss term from *Shprits and Thorne* [2004]. We primarily use the Hilmer-Voigt magnetic field that is driven by solar wind data and *Dst*, though we also compare results using the T01 magnetic field model [*Tsyganenko*, 2002] and a dipolar magnetic field. We use our model to investigate the effectiveness of radial transport,

together with electron loss, in simulating the dynamics of outer belt electrons during a typical declining-phase storm.

Rather than attempting to simulate the details of individual events, our goal is to simulate a typical HSS storm (as represented, in idealized form, by Figure 2.1). Although local acceleration of the radiation belt electrons by VLF waves can be important during these events, they are not included in the model. By performing simulations without local acceleration, but with radial transport and loss, we examine to what extent these latter processes account for observed PSD changes. For example, if local acceleration is strong for these events, our simulated PSD should be lower than the observed PSD and we would have to increase our model radial diffusion coefficient (D_{LL}) to obtain better agreement with observations.

2.2 Model inputs

Tsurutani et al. [1995] used a schematic sketch of solar wind and magnetosphere parameters to summarize the characteristics of a series of declining-phase high-speed-stream storms (also known as HILDCAAs). Using this sketch and typical numerical values from individual storms, we constructed a time series of solar wind and magnetosphere parameters for our high-speed-stream model storm, as shown in Figure 2.1.
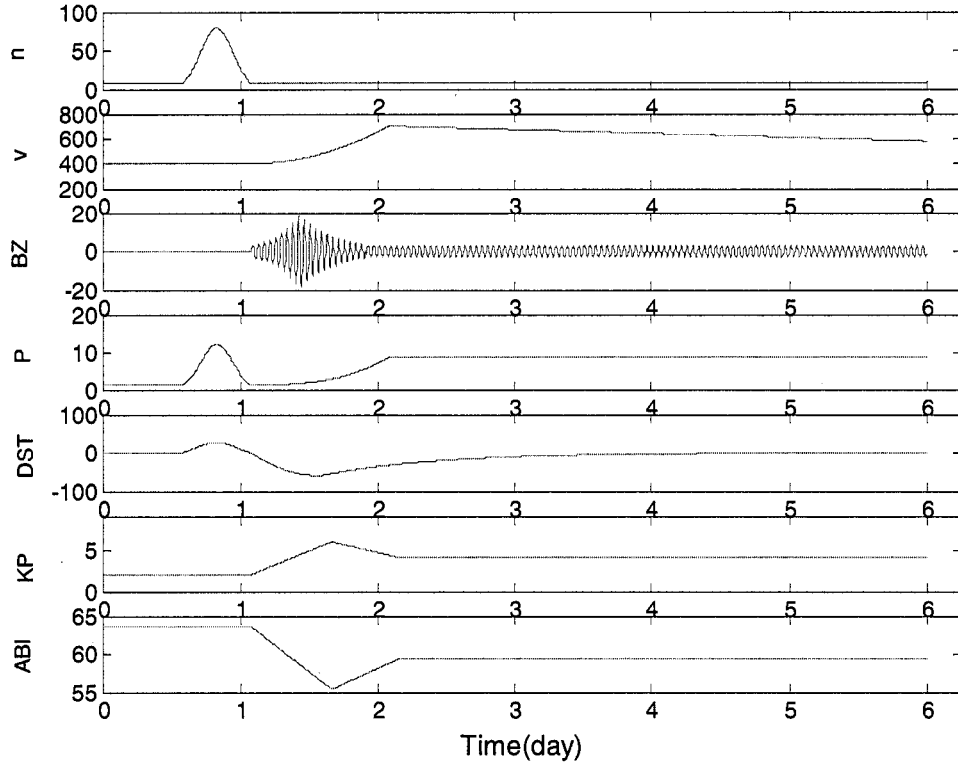
Figure 2.1 Input parameters for our idealized declining phase magnetic storm: (a) solar wind density (cm^{-3}), (b) solar wind velocity (km/s) , (c) IMF Bz (nT) , (d) solar wind ram pressure (nPa), (e) Dst index, (f) Kp index, (g) midnight equatorward boundary of the aurora (degrees).

Following the storm progression: first, the initial phase of the storm is caused by low-speed but high-density solar wind (V =400 km/s, n_{max} = 80 cm^{-3}) leading to significant positive Dst values. Next, as the solar wind speed increases, the Kp index gradually begins to increase and, during the main phase of the storm, there are large fluctuations of IMF Bz ($|Bz_{max}|$=20 nT). The minimum Dst around -70nT indicates this is a moderate storm. As the Earth is engulfed in a high-speed, low-density solar-wind stream (V_{max} = 700 km/s, n = 8 cm^{-3}), the Kp index continues to increase until it reaches the maximum value of 6. The recovery phase of the storm is long, slow and associated with a high-speed solar wind which decreases slightly from 700 km/s to

580km/s in roughly 4 days, at constant $Kp = 4$, with continuing small IMF Bz fluctuations ($|Bz_{max}|$=3 nT). The recovery phase of HSS storms is also characterized by prolonged substorm activity.

Our model requires Kp for the diffusion coefficient and electron lifetime and Kp was not parameterized in the Tsurutani's study. Therefore, we examined the relationship between the Kp and Dst indices for 11 well-defined HILDCAA events between December 1994 and September 1996 studied by *Hilmer et al.* [2000]. For all these events, Kp increased to a maximum value around the time when Dst was minimum, then Kp would decrease by about 2 units (over about 12 hours) and then maintain that value during the long, slow recovery phase.

Similarly, the equatorward boundary of the auroral oval at midnight (ABI, aurora boundary index) is not included in the *Tsurutani et al.* [1995] paper, but it is needed for the magnetic field model. We calculated it based on the formula published by *Gussenhoven et al.* [1983]:

$$ABI = 67.78 - 2.068 * Kp.$$ (2.1)

2.3 Model description

In our radiation belt model, we considered only equatorial radiation belt electrons. The electron differential flux $j(r, E)$ is converted to phase space density $f(M, L^*)$ using $f=j/p^2$, where M is the first adiabatic invariant, L^* is the Roederer L-shell [*Roederer*, 1970] and p is the relativistic momentum.

The first invariant M is divided into 60 MeV/G wide bins from 200 MeV/G to 6000 MeV/G. The Roederer L-shell L^* is divided into bins of width 0.05 from 2 to 7. As mentioned in chapter one, in this thesis we will use the symbol L for the Roederer L-shell value, rather than L^*.

Because our model is being developed as a module within the Space Weather Modeling Framework and is designed to run with a global MHD model [*Tóth et al.*, 2005], we attempted to primarily use solar-wind parameters as inputs. For example, instead of using actual GEO data, we used the solar-wind-driven predictive model of *Li et al.* [2001] for the outer boundary conditions (refer to appendix B for an introduction to the space weather modeling framework).

2.3.1 Kp-dependent D_{LL}

Our model uses the standard radial diffusion equation with a loss term [*Schulz and Lanzerotti*, 1974]:

$$\frac{\partial f}{\partial t} = L^2 \frac{\partial}{\partial L}\left(\frac{D_{LL}}{L^2}\frac{\partial f}{\partial L}\right) - \frac{f}{\tau_L}, \qquad (2.2)$$

where D_{LL} is the radial diffusion coefficient, and τ_L is the lifetime of relativistic electrons. Equation (2) is solved using the Crank-Nicholson method with a time step of 4 minutes. We used the radial diffusion coefficient developed by *Brautigam and Albert* [2000], which is based on the observational results and utilizes input parameters that are convenient for our purpose:

$$D_{LL} = D_{LL}^M + D_{LL}^E, \qquad (2.3)$$

where D_{LL}^M is the rate of radial diffusion due to the fluctuations of the magnetic field, and D_{LL}^E is derived from the electric field fluctuations. Both coefficients are *Kp*-related:

$$D_{LL}^M = 10^{(0.506KP-9.325)} L^{10}$$

$$D_{LL}^E = \frac{1}{4}\left(\frac{cE_{rms}}{B_0}\right)^2 \left[\frac{T}{1+(\omega_D T/2)^2}\right]L^6$$

$$\omega_D = \left(\frac{3Mc}{eL^2 R_E^2}\right)\left(1+\frac{2MB}{E_0}\right)^{-1/2}$$

$$E_{rms}(Kp) = 0.26(Kp-1)+0.1mV/m$$

(2.4)

where ω_D is the electron drift frequency, E_{rms} is the root mean square of the electric field amplitude, T is an exponential decay time (0.75 hour) and E_0 is the electron rest energy (0.511 MeV).

Figure 2.2(a) is a plot of D_{LL}^M vs. L for different Kp. Blue symbols are the results according to the above formula. Red Symbols represent the discrete values of D_{LL}^M at $L = 4.0$ and $L=6.6$ based on the measurements of ULF geomagnetic power at the ground stations near L=4 and at synchronous equatorial altitude [*Lanzerotti and Morgan*, 1973; *Lanzerotti et al.*, 1978]. These values are calculated from the power spectra of geomagnetic field variations, using the formula of *Falthammar* [1966] and a model magnetosphere [*Mead*, 1964]. In Figure 2.2(b), D_{LL}^E is plotted for $M = 2100$ MeV/G (~1 MeV at geosynchronous orbit) and different Kp values. Comparison of Figure 2.2(a) and 2.2(b) shows that, for the particles with $M=2100$ MeV/G, D_{LL}^M is higher than D_{LL}^E, especially at high L and for high Kp.
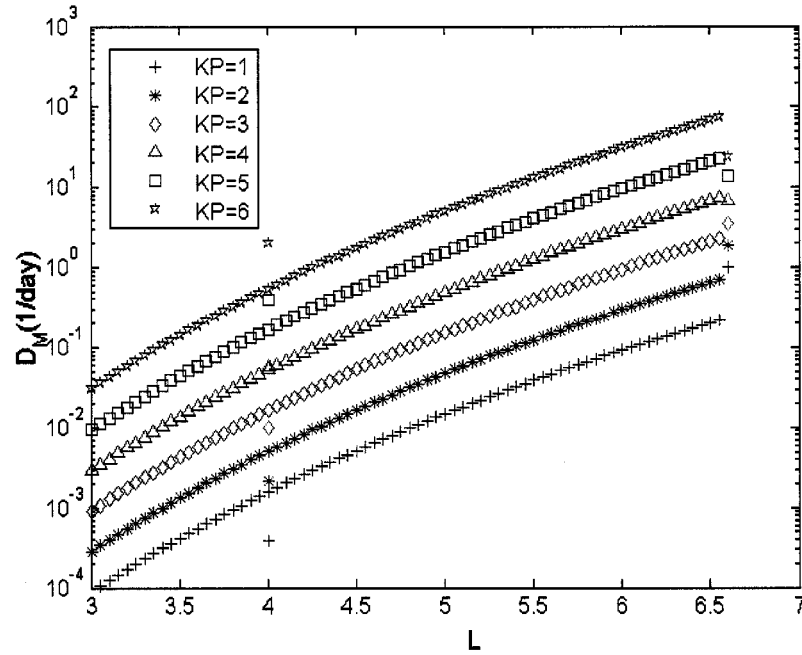
Figure 2.2(a) D_{LL}^{M} as a function of L, for Kp=1 to Kp=6.
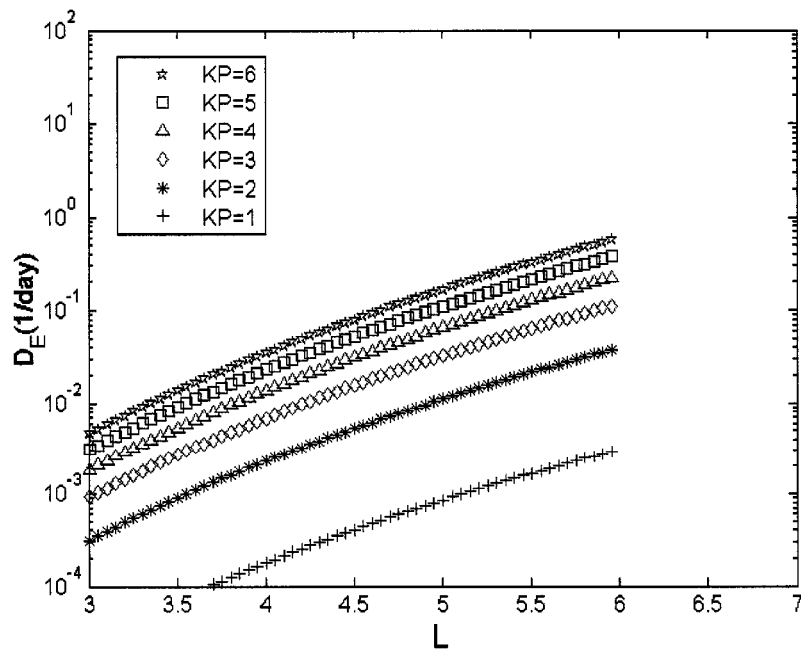
Figure 2.2(b) D_{LL}^{E} is plotted as a function of L, for Kp=1 to 6 and M=2100 MeV/G.

2.3.2 The Hilmer-Voigt magnetic field model

For the magnetic field, we used the *Hilmer-Voigt* [1995] magnetic field model developed for the Magnetospheric Specification Model (MSM) [*Freeman et al.*, 1994]. The Hilmer-Voigt model is flexible and analytic and thus can represent a wide variety of magnetic field configurations under different levels of magnetic activity. It contains contributions from a dipolar field, ring-current, tail current, and magnetopause current. It takes four input parameters: (1) dipole tilt, (2) magnetopause standoff distance, (3) midnight equatorward boundary of the aurora, and (4) *Dst* index. In our simulations, we assume the dipole tilt is zero, but the other three parameters vary according to the values in Figure 2.1.

Using the magnetic field model, we compute the Roederer L-shell using the standard formula [*Roederer*, 1970]:

$$L = \frac{2\pi\mu_E}{R_E\Phi},$$
(2.5)

where μ_E is the geomagnetic moment and can be regarded as a constant for the time scales considered here. Φ is the magnetic flux enclosed by a drift shell and is computed by mapping the drift shell (the contour of constant B on the equatorial plane) to the ionosphere and calculating the magnetic flux inside that curve (refer to Appendix A for more detail). .

2.3.3 Initial conditions and boundary conditions

For the initial phase-space density, we convert the flux j given by the AE8MIN Model [*Vette*, 1991] to phase-space density as a function of the adiabatic invariants using the Hilmer-Voigt magnetic field model.

The inner boundary is simply fixed at $L=2.0$ with the value calculated from the AE8MIN model. The location of the outer boundary is chosen to be the minimum of L_c vs. L_g, with L_c defined as the last closed drift shell multiplied by a factor of 0.9 in order to avoid Shabansky orbits [*Shabansky*, 1971] and L_g defined as the Roederer L-value of the drift orbit that crosses local midnight at 6.6 R_E. The time-dependent PSD at the outer boundary is calculated using the model of *Li et al.* [2001]. This model uses solar wind inputs to predict the MeV electron flux at geostationary orbit.

2.3.4 Electron lifetime and pitch angle diffusion

Pitch-angle diffusion is also important in radiation belt dynamics, but a detailed simulation of this process is beyond the scope of this work. Instead, to evaluate the effects of loss by pitch-angle diffusion, we divide the modeling grid into two regions using the plasmapause as the boundary. For the location of the plasmapause, we used the formula:

$$L_{pp} = 5.6 - 0.46\,Kp_{\max} \qquad (2.6)$$

where $Kp_{\max}$ is the maximum Kp value in the preceding 24 hours [*Carpenter and Anderson*, 1992].

Within the plasmapause during storm times we used CRRES observations to estimate the lifetime of energetic electrons [*Meredith et al.*, 2006]. The values range from 2.0-5.0 days for 510KeV electrons to 5.5-6.5 days for 1.09MeV electrons. For electrons with higher energy than 1.09MeV, we calculated their lifetimes by using piece-wise linear extrapolation. Figure 2.3 shows the lifetimes for 214KeV, 510KeV, 1.09MeV and 3.00MeV electrons within the plasmasphere following a magnetic storm.

Inside the plasmapause the lifetime of high energy electrons before the storm is scaled by multiplying 10 days by $(35/10)^2$, where we assume a nominal VLF wave amplitude of 10 pT for quiet time and 35 pT for the moderate storm.

For the zone outside the plasmapause, we used an estimate of the Kp-dependent energetic-electron lifetime τ_L given by *Shprits and Thorne* [2004]. In their model, τ_L varies linearly with Kp from $\tau_L = 3$ day when $Kp = 2$ to $\tau_L = 0.5$ day when $Kp = 6$. Also note that in their model, τ_L is independent of energy and L.
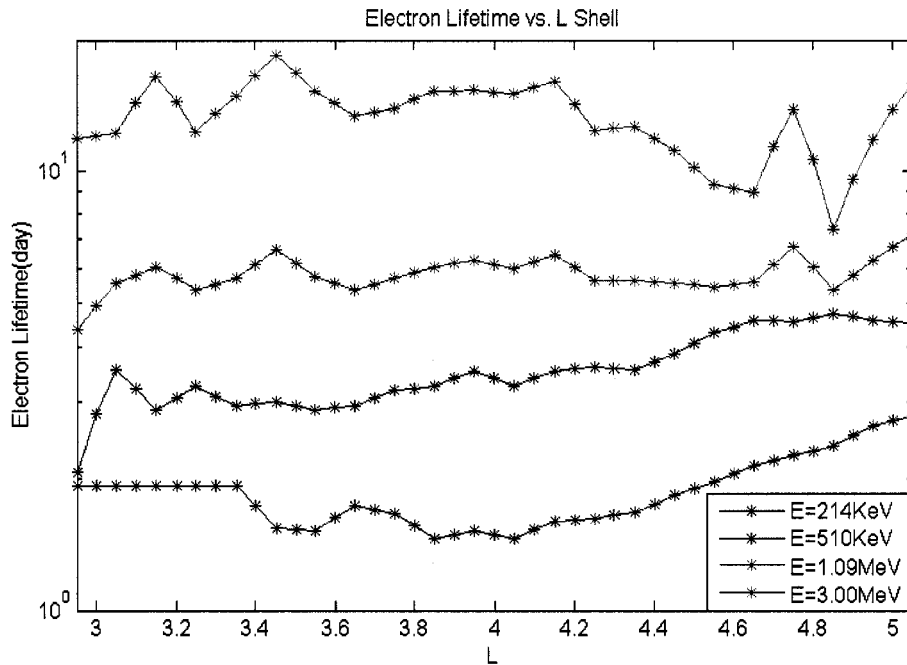
Figure 2.3 Electron Lifetimes for different energy electrons following a magnetic storm. Here the lifetimes for 214KeV, 510KeV, 1.09MeV electrons are measure results from CRRESS. Lifetime for 3.0MeV electron is calculated using linear extrapolation.

2.4 Simulation results

2.4.1 PSD vs. L and time

Figure 2.4 presents simulation results of the radiation belt model for M=2100MeV/G, which corresponds to 1 MeV at geosynchronous orbit in a dipole magnetic field. The top panel shows phase space density (PSD) computed including loss ($f_{LOSS}(L,t)$), while the second panel shows phase space density computed assuming no loss ($f(L,t)$). The third panel plots the ratio of f_{LOSS}/f. The white line shows L_c, 90 percent of the last closed drift orbit; the green line shows L_g, the Roederer L-value of the drift orbit that crosses local midnight at 6.6 R_E; and the blue line shows the location of the plasmapause. The outer boundary of the simulation region is L_{max} = min(L_c, L_g). In the region $L > L_{max}$ (outside the simulation region), we plot the value of the PSD at the outer boundary L_{max} in order to show the time variations of f (L_{max}), but these values should not be interpreted as the physical values of f for $L > L_{max}$.

In this figure, the PSD exhibits an almost static distribution with peak value at $L \approx 5 \sim 6$ for the period $t = 0$ to $t = 0.6$ day during quiet solar wind conditions. The first change occurs between t=0.6 day and t=1day when Dst is positive and increases slightly due to the increased solar wind pressure. During the time interval (t=0 to t=1.6) f_{LOSS} (computed including loss) and f (no loss) are very similar because the loss rate is too low to cause any observable change.

A period of high-speed, low density solar wind begins at about t=1.1 day. The negative value of Dst (minimum -70nT) indicates a moderate storm. The most dramatic solar wind change is the highly fluctuating B_z component. From about t=1.1 day to t=1.8 day, PSD decreases in the region $L \geq 4.4$ due to outward diffusion.

(a)
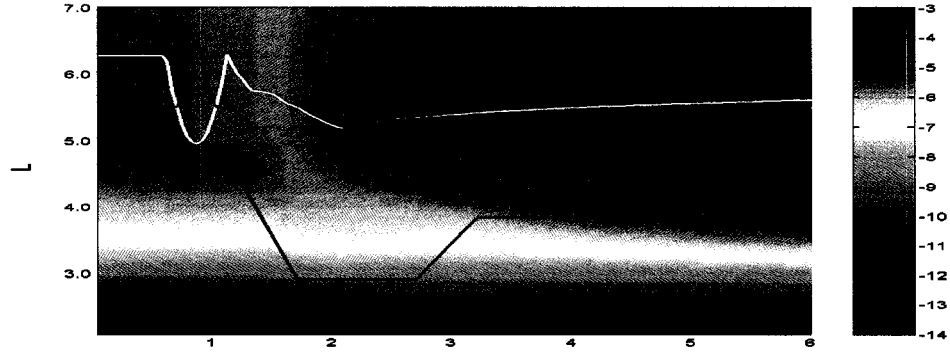
(b)
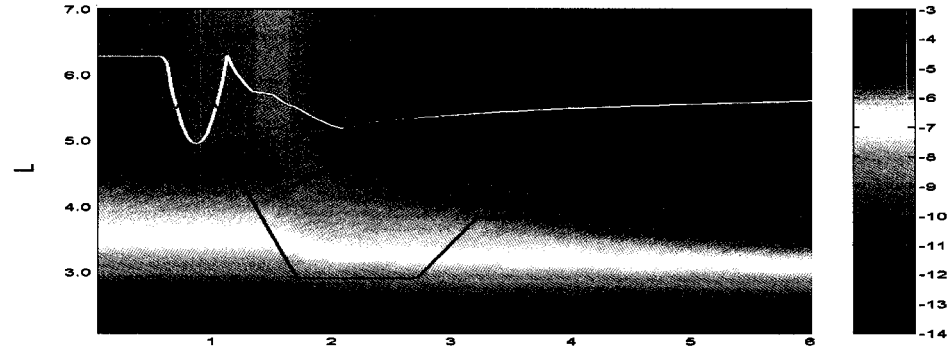
(c)
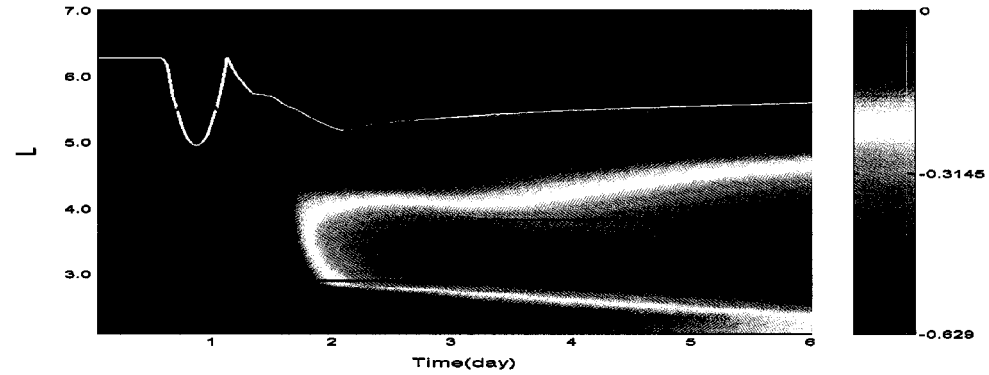
Figure 2.4 Modeling result for energetic electrons (M=2100MeV/G). The top panel shows $\log_{10}[f_{LOSS}(\text{cm}^{-2}\text{s}^{-1}\text{MeV}^{-2}\text{c}^{-1})]$ computed including estimated loss by precipitation (see text); the second panel shows $\log_{10}[f(\text{cm}^{-2}\ \text{s}^{-1}\ \text{MeV}^{-2}\text{c}^{-1})]$, which is computed assuming no loss. The third panel is $\text{Log}_{10}(f_{LOSS}/f)$. The white line represents L_c, the green line is L_g, and the blue line shows the location of the plasmapause. The time is in days.

An obvious increase of PSD at the outer boundary begins at $t = 1.9$ day when the storm has entered the recovery phase. The velocity of the solar wind has almost reached the maximum value (700 km/s) and Kp reaches the value of 6 at approximately the same time. In the early recovery phase ($t = 1.9$ to 3.3 day), the PSD has increased by a factor of 100 at $L>4$ and particles are quickly diffused to lower L values. By $t = 2.5$ day, a significant increase of PSD is observed at all $L>4.5$. The corresponding steep gradient (i.e., the region of transition from red to orange in Figure 2.4(a)) in PSD moves from $L \approx 4.5$ at $t = 2.5$ day to $L \approx 3.5$ at $t = 6$ day.

After $t = 3.5$ ($Kp=4$), the maximum difference between f and f_{LOSS} occurs at $L=3\sim3.5$ where f_{LOSS} is approximately four times smaller than f. However at $t = 4.5$ day f and f_{LOSS} have similar values for $L > 4$ and the simulation shows that the loss effect is not important in the region $4.2 \leq L \leq 6.6$. We will study the loss rates in this region in the next section.

The location of the plasmapause is shown by the blue curve. It decreases from $L= 4.68$ to $L= 3.76$ as Kp increases from 2 to 4. The bottom panel of figure 2.4 shows that the loss effect seems to be more important within the plasmapause during the later recovery phase of the storm. Overall the loss term doesn't have a strong effect on the simulation results for transport between geosynchronous and $L \sim 4.0$ because that again is dominated by radial transport.

2.4.2 PSD vs. time and comparison with observations

The top panel of Figure 2.5 from *Hilmer et al.* [2000] plots six-hour averages of phase space density near $R\sim6.6R_E$ from the Los Alamos spacecraft 1984-129, 1991-080, 1987-097, 1989-046, 1990-095, and 1994-084 for $M\sim2100$MeV/G SOPA data. Also plotted are PSD at $R\sim4.2R_E$ from the GPS Navstar NS-24 and NS-28 spacecraft for $M\sim1000$-3300 MeV/G, from BDD-II dosimeters. For 26 of the 31 HSS events studied, *Hilmer et al.* found that as long as the recovery-

phase average of Kp was above 3.25, the PSD at geosynchronous orbit was higher than at $R = 4.2$ R_E and that the changes at $R = 4.2$ R_E were consistent with inward radial diffusion from geosynchronous orbit. To compare with the *Hilmer et al.* PSD, we calculated the flux from the model PSD which uses the Hilmer-Voigt magnetic field and then used a dipole magnetic field to convert that model flux to PSD. Also the PSD values from *Hilmer et al.* at geosynchronous orbit are at radial distance $R=6.6R_E$ rather than Roederer $L=6.6$ and similarly the GPS location is $R=4.2R_E$ rather than $L=4.2$.

The middle panel is the model result for phase space density at $R{\sim}6.6$ R_E and $R{\sim}4.2$ R_E for the HSS solar-wind conditions of Figure 1. In the main phase of the storm, the phase space density at $6.6R_E$ has a small but apparent decrease in both data and model results. Similarly, at the beginning of the recovery phase, a sharp and large increase in both phase space densities is observed at 6.6 R_E. In both data and model results, the PSD increases in the recovery phase by a factor of ${\sim}100$ over its pre-storm value and maintains that high value for the rest of the recovery phase. The good agreement of observed and model PSD at $R = 6.6$ R_E confirms the accuracy of the *Li et al.* [2001] model at the outer boundary.
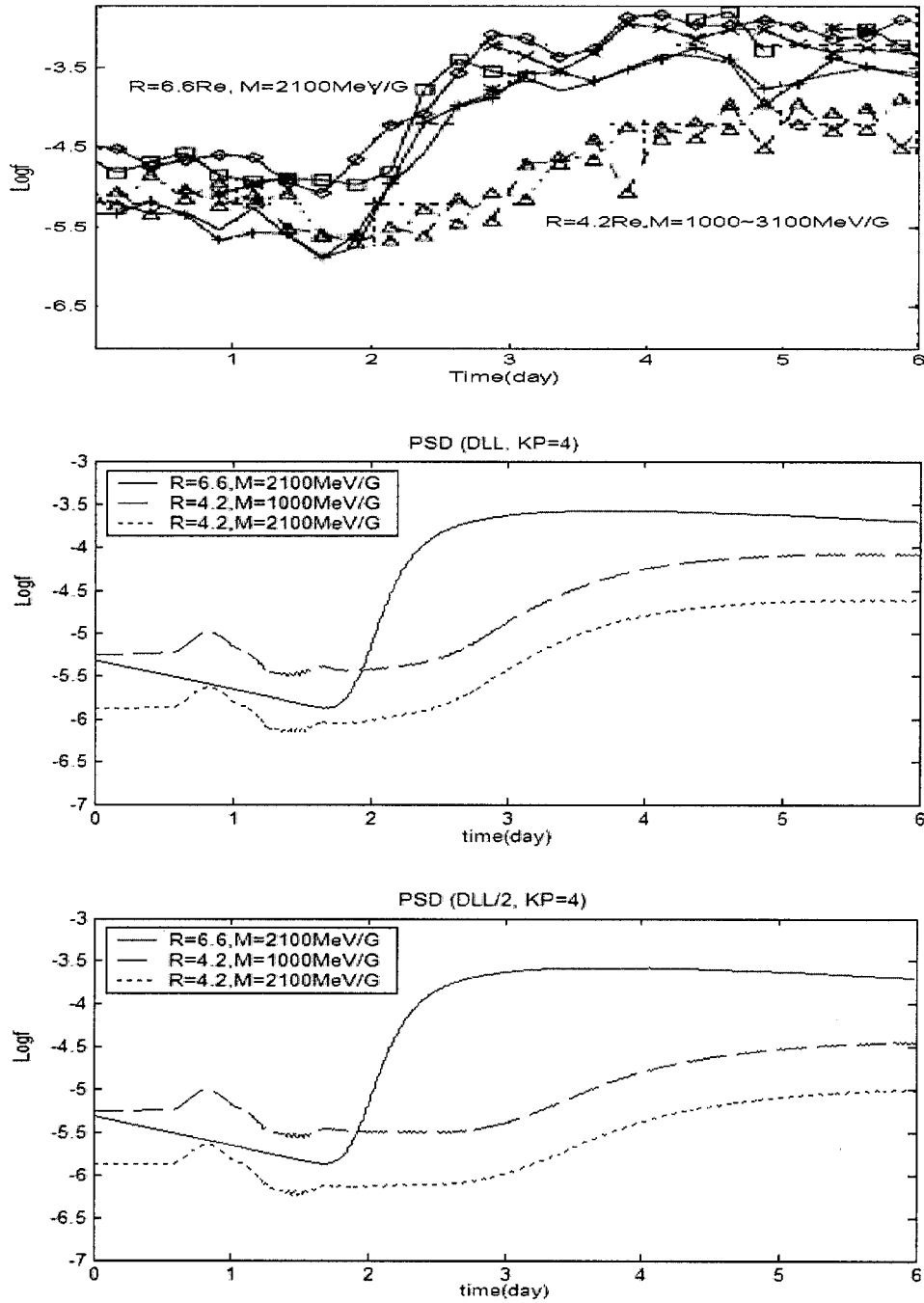
Figure 2.5 Model results compared with observations. (1) The top panel showssix-hour averages of phase space density near $R\sim6.6R_E$ ($M\sim2100$ MeV/G) and$R\sim4.2R_E$ ($M\sim1000$-2100MeV/G) from the observations of *Hilmer et al.* [2000] for Julian Day 28-34, 1995; the different curves refer to different spacecraft (see text). (2) Calculated phase space density f_L for ($R\sim6.6R_E$, $M\sim2100$), ($R\sim4.2$ R_E, $M\sim1000$),($R\sim4.2$ R_E, $M\sim2100$), using D_{LL} from equation 4; (3) Modeling result using $D_{LL}/2$

However, there are differences between the model and observations at R = 4.2 Re. Model results are plotted for M = 2100 MeV/G (the same value as the GEO PSD) and also for M = 1000 MeV/G. Because of the steep slope of the energy spectrum, the PSD from the M = 1000~3300 MeV/G GPS instruments is expected to be dominated by the M~1000 MeV/G particles. During the main phase, there is good agreement between model and data with both showing a weak drop. However, differences become apparent in the recovery phase. The simulation shows a slightly faster enhancement than the observations and reaches a higher final value. The simulation results show that the effect of the loss term is relatively weak between L =6.6 and L=4.2; these differences must be due to different radial diffusion rates.

To test the sensitivity of the model results to the radial-diffusion coefficient D_{LL}, we divided the *Brautigam and Albert* [2001] formula by a factor of 2. As shown in the bottom panel of Figure 5, the simulation results then reproduce the observational results more accurately by improving both the rate of increase of PSD and the final value.

To further study the evolution of phase space density at R = 4.2 R_E, we compared our simulation results with another high-speed-stream event in July 1995 from *Hilmer et al.* [2001] where the observations show no growth of phase space density at this location. To investigate *Hilmer et al.*'s conclusion that the growth rate in phase space density at R=4.2 R_E depended crucially on the average of the *Kp* index, the simulation was rerun with the *Kp* maximum reduced from 6 to 5 and the *Kp* values during the recovery phase reduced from 4 to 3.
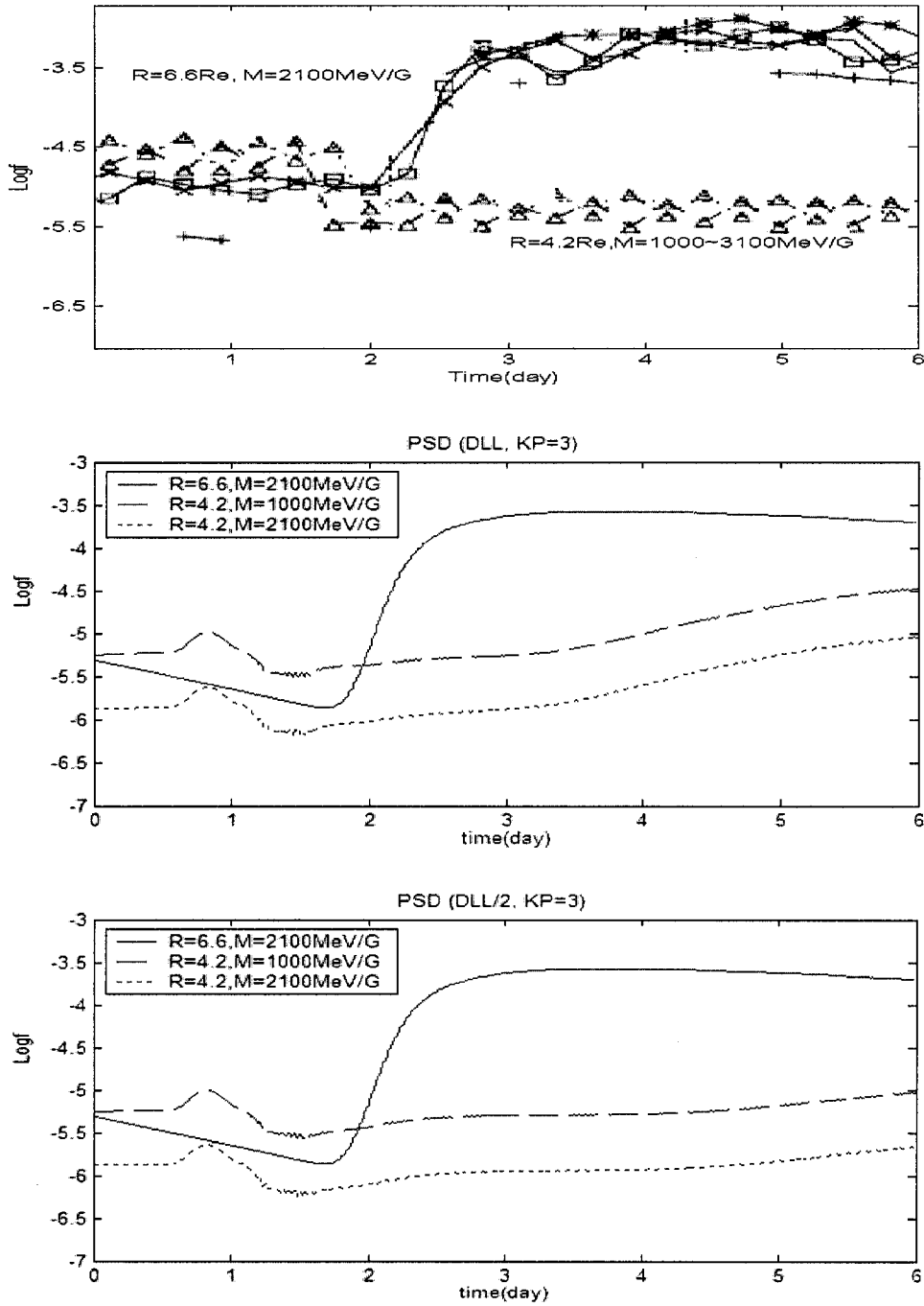
Figure 2.6 Model results compared with observations. (1) The top panel shows *Hilmer et al.* [2000] observations for Julian Day 195-201, 1995; the points are six-hour averages of phase space density near $R\sim6.6$ R_E ($M\sim2100$ MeV/G) and $R\sim4.2$ R_E ($M\sim1000$-2100MeV/G). (2) The second panel shows simulated values of f_L for ($R\sim6.6$ R_E, $M\sim2100$), ($R\sim4.2$ R_E, $M\sim1000$), ($R\sim4.2$ R_E, $M\sim2100$), using D_{LL}; (3) The bottom panel shows the modeling result for $D_{LL}/2$.

These results from the run, shown in Figure 2.6, illustrate the same pattern as the previous simulation run. That is, the model PSD at $R = 4.2$ R_E using the full Brautigam-Albert D_{LL} (middle panel) increases substantially, but with the Brautigam-Albert D_{LL} reduced by a factor of 2 (bottom panel), the PSD stays fairly flat as shown in the observations. Thus the simulation results are consistent with our previous conclusion: the model results agree better with observations if we divide the *Brautigam and Albert* [2000] diffusion coefficient by 2.

2.4.3 Rate of Growth

To compare various model results with measurements, we calculated the rate of increase of electron PSD at $R = 4.2$ R_E (from *Hilmer et al.* [2000]) by

$$\lambda = \frac{1}{t_{max} - t_0} \ln[\frac{f_{max}}{f_0}] \qquad (2.7)$$

where t_0 is the time when the phase space density begins to increase and has value f_0. t_{max} is the time when the phase space density has reached the value f_{max}. During the recovery phase, PSD usually first grows quickly, then either stays constant or has a very slow increase. We used two straight line to fit the PSD during these two stages and define f_{max} to be the value of PSD at the intersection point of the two straight lines.
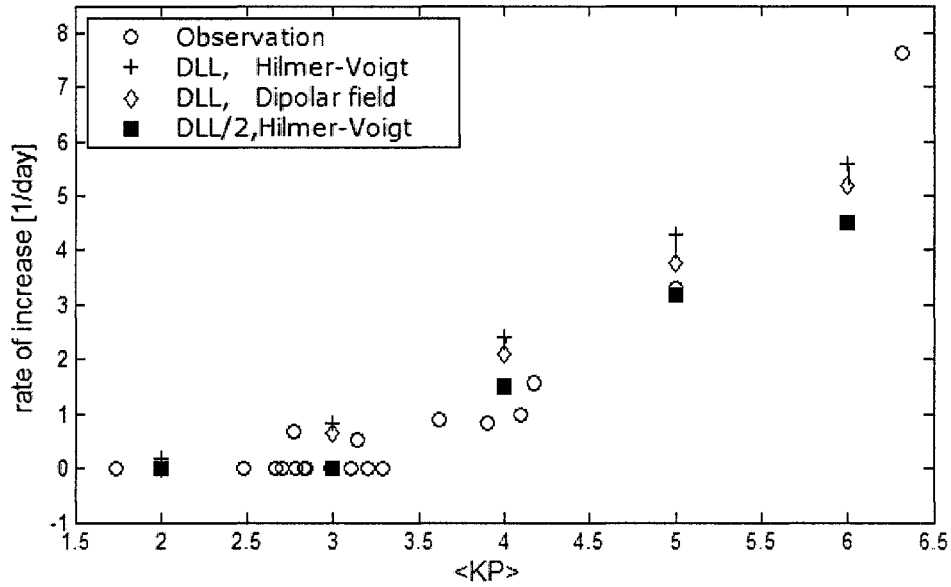
Figure 2.7 Comparison of observed rate of change of PSD (λ) vs. recovery-phase *Kp*, as tabulated by *Hilmer et al.* [2000], with model runs using Hilmer-Voigt magnetic field and a dipolar magnetic field, and both the nominal Brautigam-Albert diffusion coefficient and that coefficient divided by 2.

Figure 2.7 shows rates of PSD increase λ, for several values of the recovery-phase *Kp*. The circles denote measured values from *Hilmer et al.* [2000]. Also shown are model results computed assuming the full Brautigam-Albert diffusion coefficient D_{LL} (using the Hilmer-Voigt magnetic field model and a dipolar magnetic field) and also assuming that the Brautigam and Albert D_{LL} has been reduced by a factor of 2. The differences between the Hilmer-Voigt and dipole field values show the effect of the ring current contribution to the magnetic field model which will be examined more closely in the next section.

The model runs in Figure 2.7 use the same input parameters shown in Figure 1, but with a range of *Kp* values. Because other parameters in the *Hilmer et al.* observations do not change

significantly compared to our model storm, we changed only the recovery-phase Kp. The initial Kp is not changed, but we assume the maximum Kp is two units higher than the recovery-phase Kp. The λ values for recovery-phase Kp values of 4 and 3 are obtained from previous runs shown as Figures 5 and 6, respectively.

This plot shows again that dividing the Brautigam-Albert diffusion coefficients by a factor of 2 produces better agreement between model and observation. The model results with $D_{LL}/2$ also reproduce the observed result that PSD does not increase significantly unless Kp is greater than about 3.25. Note that for $Kp \sim 6$, the simulated λ is significantly smaller than the observed result. However, this event (event 8 in the *Hilmer et al.* paper) is not a typical HSS event because B_z remains negative for a substantial portion of the event and does not change sign multiple times as in a typical HSS event. We used this event because it is the only observational point available at $Kp \sim 6$.).

2.4.4 Sensitivity to magnetic field model

To understand the sensitivity of our simulation results to the underlying magnetic field model, we compared simulation results calculated using three different magnetic field models: the Hilmer-Voigt [*Hilmer et al.*, 1995] model described in section 3, the T01 model [*Tsyganenko*, 2002], and a dipolar magnetic field.

The three panels of figure 2.8 show qualitatively similar results during the recovery phase, but there are quantitative differences during the main phase and the early recovery phase which are most likely due to differences in the ring current field of the different magnetic field models.
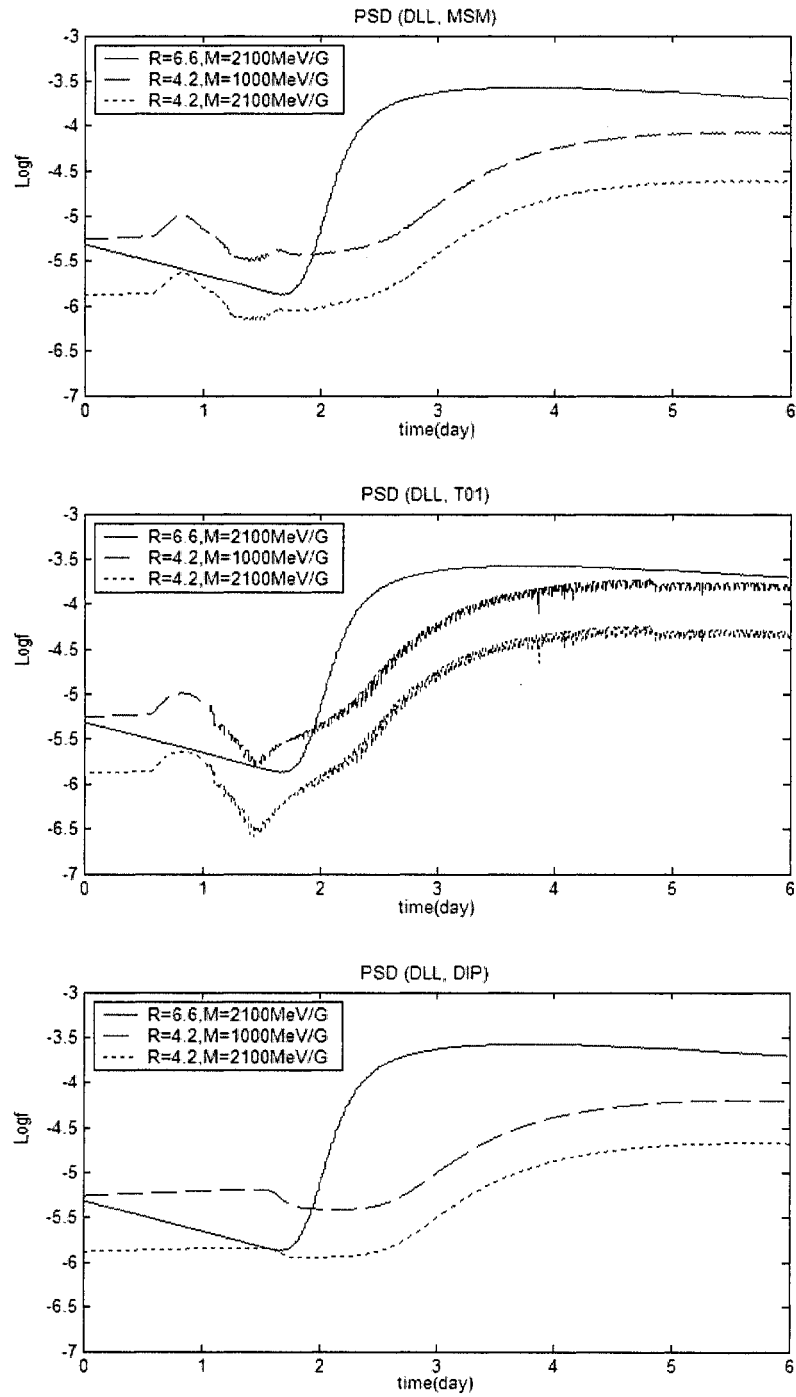
Figure2.8 Simulation results using different magnetic field models: (a) the Hilmer-Voigt

model; (b) the T01 Model; (c) a dipolar magnetic field.

To investigate the effect of the ring current field in more detail, in Figure 2.9 we plot the Roederer L values versus time at a radial distance of R=4.2R_E at midnight, for the three magnetic field models. The variations of L with time for different fields shows that the main phase and early recovery phase PSD differences are due to ring current field changes. During the main phase, the inflation of an electron drift shell is responsible for the decrease of phase space density at R=4.2R_E (but not at $L = 4.2$) as expected for the so-called Dst effect [e.g., *Kim and Chan*, 1997]. Also the T01 model displays a larger decrease in L than the Hilmer-Voigt magnetic field model which in turn produces the larger decrease of phase space density during the main phase. The dipolar field does not exhibit this Dst effect since it does not include the ring-current field.

The recovery of the inner-magnetosphere magnetic field as Dst decays back to zero brings particles to lower radial distances. Since the dipolar magnetic field does not exhibit this effect, the rate of radial transport during the recovery phase is slower for the dipole magnetic field than for the other two models. The rate of PSD increase for the T01 model is slightly larger than for the Hilmer-Voigt model. However, the overall difference in PSD between the Hilmer-Voigt and T01 magnetic field models is not large, which is expected for these moderate storms.
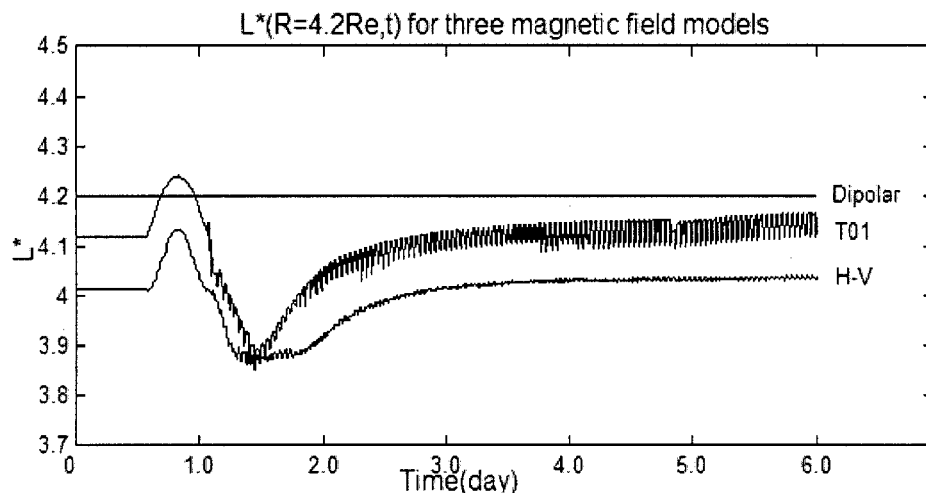
Figure 2.9 The variation of Roederer L-values (for the drift shell corresponding to R = 4.2R$_E$ at midnight) plotted during the model storm for three different magnetic field models.

2.4.5 PSD driven by real input parameters

To test the efficiency of our generic model storm as a good duplication of individual events, we reran our radial diffusion model for the two HSSWS events in section 2.4.2 with actual solar wind drivers.

Figures 2.10 and 2.11 show the solar wind conditions, magnetic indices and the simulation results of electron phase space densities for the two storms in January 1995 and July 1995. Comparing the figures with the simulation results using model input parameters (Figures 2.5 and 2.6), we find the modeled phase space densities do not come out significantly different. The main difference between the model runs is during the latter stages of the recovery phase as shown in Figure 2.6 and 2.11. The run using actual input data (Figure 2.11) shows a dropout in simulated PSD which is observed by the measured values. However, the simulated input run (Figure 2.6)

does not show the drop out of the PSD so that using solar wind drivers instead of model parameters can actually improve the agreement between model results and measured results.

Further, we explore the sensitivity of the model results to the diffusion coefficients using the January 1995 storm event. Figure 2.12 shows the simulated phase space density using the Brautigam and Albert D_{LL} divided by factors: 1.5, 2.0, and 2.5. The results show a spread in the phase space density comparable to the spread in the GPS measurements. Therefore we can conclude that good agreement between the observations and the simulation results can be obtained using the Brautigam and Albert D_{LL} reduced by a factor within the range 2 ± 0.5.
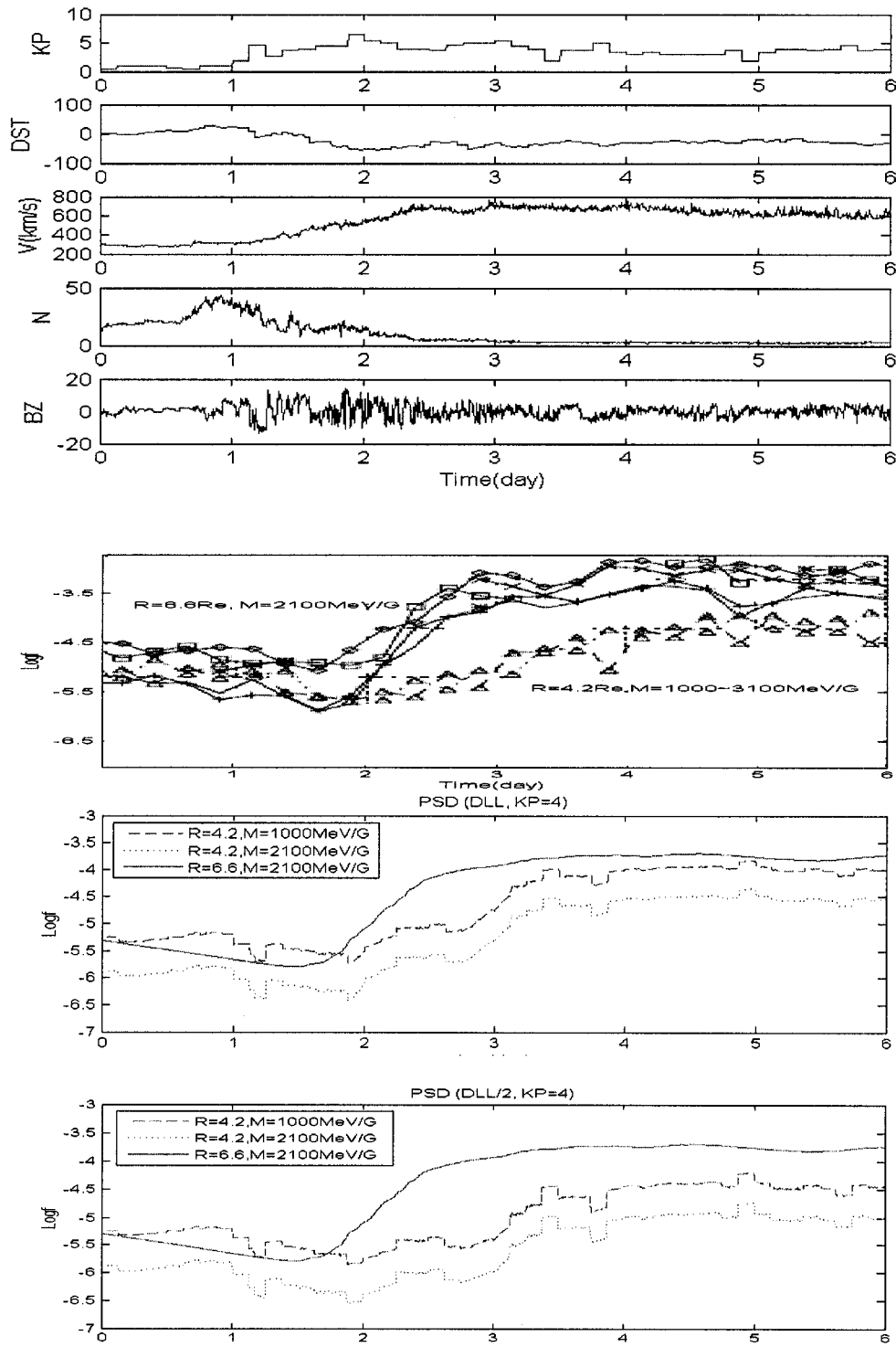
Figure 2.10 Simulation results of phase space density driven by real input parameters for the HSSWS event in January, 1995.
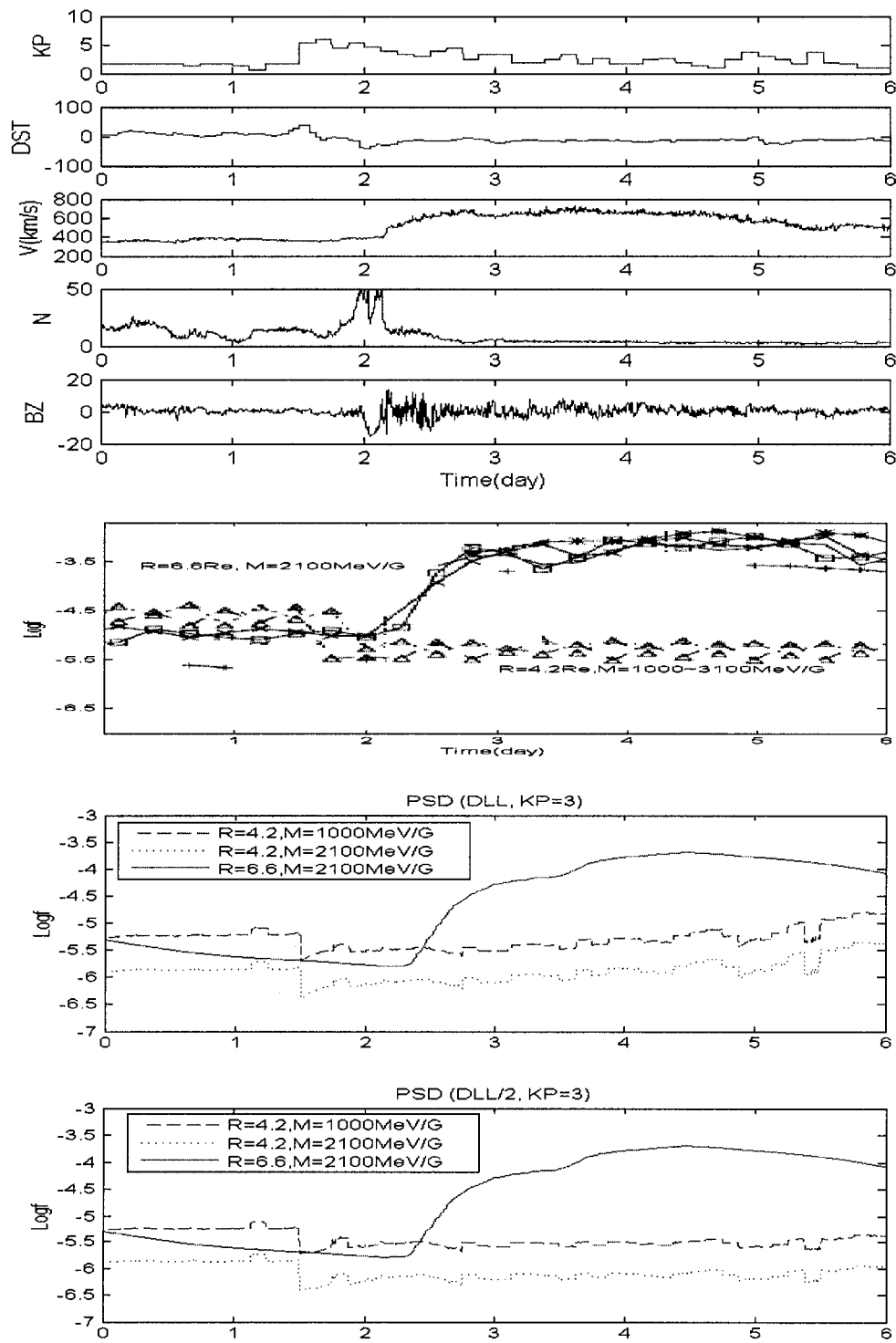
Figure 2.11 Simulation results of phase space density driven by real input parameters for the HSSWS event in July, 1995.
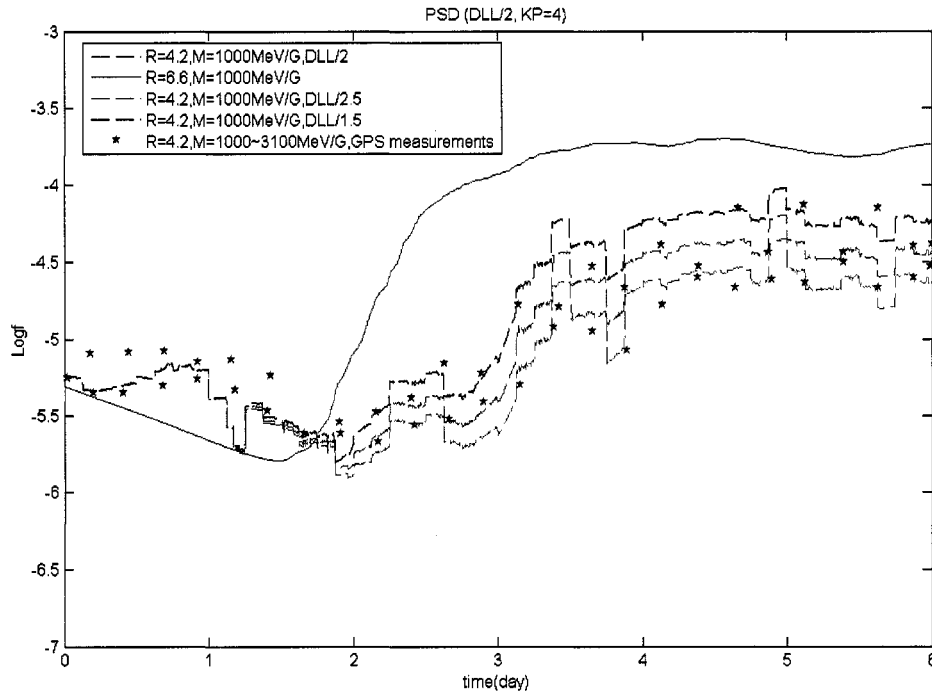
Figure 2.12 Simulation results of phase space density driven by real input parameters for the HSSWS event in January, 1995, for different diffusion coefficients.

Compared with real data, it is clear that the Brautigam and Albert formula of D_{LL}^M overestimates the diffusion rate at geosynchronous orbit for high Kp (Kp =3 and 4). To test the effect of the discrepancy between the Brautigam and Albert formula and measured results, we calculated the D_{LL}^M directly from the measured values (red symbols in Figure 2.2(a)) and reran the two events in January 1995 and July 1995. In figure 2.13, we compare new modeling PSD (red curves) with results using Brautigam-Albert formula of D_{LL}^M (blue curves). The new results are more consistent with the satellite measurements. However there is still some discrepancy between the new model results and measured PSD.
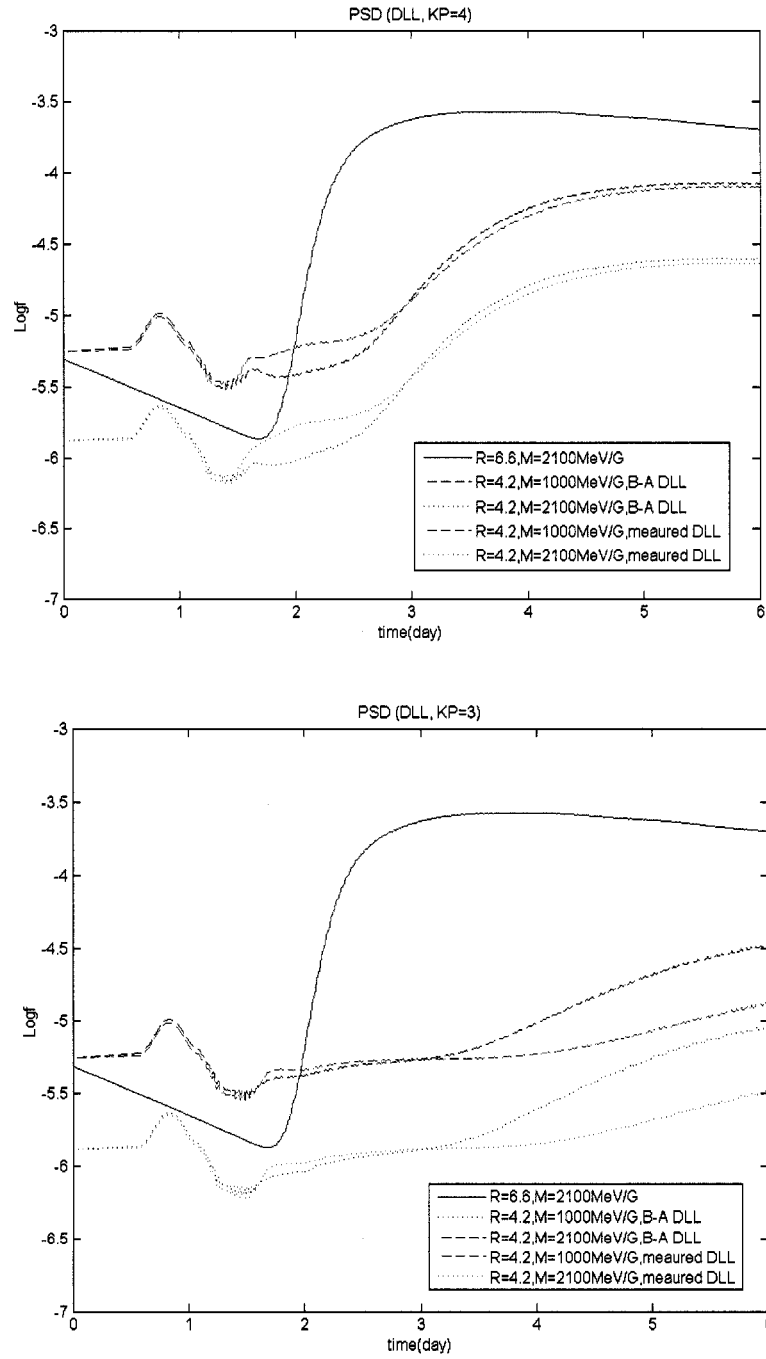
Figure 2.13 Model results of phase space density with measured D_{LL} (red curves) and Brautigam-Albert formula of D_{LL} (blue curves) are compared at L=4.2.

2.4.6 Error due to pitch angle assumptions

Though our model traces equatorially-mirroring particles, we compared with observational values from GEO and GPS spacecraft that are closer to being omni-directional fluxes than fluxes of equatorial-mirroring particles, and there is some error involved in this procedure. The error can be estimated by using another simple approximation that we could have made, namely that of an isotropic pitch-angle distribution. That is, we could have assumed that the geosynchronous pitch-angle distribution was isotropic and that the particles underwent strong, elastic pitch-angle scattering as they underwent radial transport. In the two cases, the radial diffusion equation would be exactly the same. The crucial difference in the two lies in the fact that they imply different amounts of adiabatic acceleration between the two locations.

In the isotropic-pitch-angle case, the relevant invariant [Chen and Schulz, 2001] is

$$\Lambda = P^3 \Psi , \qquad (2.8)$$

where $\Psi = \int ds / B$ and P is the relativistic momentum. The energy W_4 at $L=4$ that corresponds to the same Λ as energy $W_{6.6}$ at geo is given by

$$W_4^2 = m^2 c^4 + \left(\frac{\Psi_{6.6}}{\Psi_4} \right)^{2/3} (W_{6.6}^2 - m^2 c^4) , \qquad (2.9)$$

whereas, for equatorially-mirroring particles the corresponding expression is

$$W_4^2 = m^2 c^4 + \frac{B_{e4}}{B_{e6.6}} (W_{6.6}^2 - m^2 c^4) , \qquad (2.10)$$

where B_e is the equatorial magnetic field. To get a rough idea of the difference, consider the ultra-relativistic approximation. In that case, the isotropic-pitch-angle approximation implies that

the particles have their energies increased by a factor of $\left(\dfrac{\Psi_{6.6}}{\Psi_4}\right)^{1/3}$, whereas in the equatorial-

mirroring case, the factor is $\left(\dfrac{B_{e4}}{B_{e6.6}}\right)^{1/2}$. For a dipole magnetic field $\Psi \propto L^4$, while $B_e \propto L^3$, so

that $\left(\dfrac{\Psi_{6.6}}{\Psi_4}\right)^{1/3} \approx 1.95$ and $\left(\dfrac{B_{e4}}{B_{e6.6}}\right)^{1/2} \approx 2.12$, so the estimated energy at $L=4$, corresponding to a

given geosynchronous energy, is about 9% smaller in the case of isotropic pitch angles than in

the case of equatorially-mirroring particles. Given the general imprecision of the comparisons

due to the wide pass-bands of the GPS particle detector, this is a small error. Also, we calculated

the error using the Hilmer-Voigt magnetic fields and obtained an error of about 15%~18%,

which is still relatively small.

2.5. Summary and discussion

Geomagnetic activity in the declining phase of the solar cycle is characterized by long-lasting

high-speed solar wind streams that originate in solar coronal holes. We developed a radial

transport radiation belt model with a time-dependent outer boundary condition, time-dependent

magnetic field model, *Kp*-dependent loss rates, and a *Kp*-dependent radial diffusion coefficient to

study the changes in the phase space density of relativistic electrons for a typical high-speed-

stream model storm.

Our simulation results show that during the main phase of the storm, the phase space density

at the outer boundary exhibits a slight decrease, but during the long recovery phase there is a

large, rapid increase in PSD at the outer boundary which then quickly diffuses to lower L. Also, the loss lifetime does not have a large effect in the region $4.2<L<6.6$ at any time during the storm.

The agreement is very good between the simulation results and observations of *Hilmer et al.* [2000] during the main phase of the storm at both $R = 6.6$ R_E and $R = 4.2$ R_E. However, in the recovery phase the simulation results at $R = 4.2$ R_E show a more rapid enhancement of PSD than the observations, which indicates the need to assume a weaker radial diffusion coefficient. We found that reducing the Brautigam-Albert D_{LL} by a factor of two gives good agreement between the observations and the model results. The loss lifetime is reasonably accurate since it is based on comparisons with observations [*Shprits and Thorne*, 2004; *Meredith et al.*, 2006], and our simulation results show that they are insensitive to the loss rate.

We explored the sensitivity of our model to the input parameters and the diffusion coefficient model. We found that both using real solar wind drivers and using the measured diffusion coefficient can help to improve the discrepancy between the model results and observed PSD.

Using alternative magnetic field models we found differences that appear during the main phase and early recovery phase which suggests that the magnetic field, due to the ring current field, is playing a role. However, as would be expected for the relatively weak HSS storms, the ring current effects are not significantly large.

The effects of different magnetic field models may explain why the Brautigam and Albert formula overestimates particle diffusion. The *Brautigam and Albert* [2000] diffusion coefficient was calculated to maximize agreement with the discrete values at $L=4.0$ from *Lanzerotti and Morgan* [1973] and those at $L=6.6$ from *Lanzerotti et al.* [1978]. However *Lanzerotti et al.* based their estimate of the diffusion coefficient using the Mead magnetic field model [*Mead*, 1964],

which did not have a ring current field. When empirical diffusion coefficients were derived from data assuming a dipolar field or some other field that does not represent the ring-current inflation, the resulting diffusion coefficients combine the effects of two different mechanisms for radial transport, namely true radial diffusion that involves violation of the 3rd invariant and collapse of the field due to decay of the ring current. More quantitatively, Figure 2.10 shows that this effect is not large enough to explain a factor of two difference in D_{LL}, because it causes a change in λ (shown by the vertical lines), which is less than half of the difference in λ using D_{LL}, compared to using $D_{LL}/2$.

In addition to radial transport, local energization by cyclotron resonances with VLF waves has been proposed as a mechanism for MeV electron increases near $R{\sim}4R_E$ [e.g., *Horne and Thorne*, 1998; *Summers et al.*, 1998; *Summers and Ma*, 2000]. Results in this paper show that good agreement between observations and simulations is obtained without this process. This may be an indication that radiation belt electron transport between geosynchronous orbit and $R{\sim}4$ R_E is dominated by radial diffusion rather than by local energization, for these declining-phase high-speed solar-wind stream storms. On the other hand, chorus VLF waves are expected to be strong for these HSS storms [*Meredith et al.*, 2003] and so simulations which include local acceleration should also be performed. Similarly, radial diffusion calculations should be carried out for events other than HSS storms, including CME-driven storms, preferably also including effects of VLF waves and realistic magnetic field models, so that effects of both processes can be compared quantitatively.

Yue Chen [2006] calculated the PSD gradients using the data from multiple satellites (LANL Geosynchronous satellites, POLAR and GPS). The results showed that during storms, negative

radial gradients are observed in the L-range from 5-9 and then developed into a peak around L~6. Then inward radial diffusion could transport the PSD into the deeper inner magnetic field. Although the results are currently limited to storms during the solar maximum, local acceleration provides another possible interpretation for the temporal variation of relativistic electron fluxes during the HSSWS in the declining phase of solar cycle.

References

Albert, J. M. (1999), Analysis of quasi-linear diffusion coefficients, *J. Geophys. Res., 104(A2)*, 2429.

Baker, D. N. and J. B. Blake (1986), Highly relativistic electrons in the Earth's outer magnetosphere, 1. Lifetimes and temporal history 1979-1984, *J. Geophys., Res., 91*, 4265.

Baker, D.N., et al. (1994), Realativistic electron acceleration and decay time scales in the inner and outer radiation belts: SAMPEX, *Geophys. Res. Lett., 21*, 409.

Baker, D.N., et al. (1997), Recurrent geomagnetic storms and relativistic electron enhancements in the outer magnetosphere: ISTP coordinated measurements, *J. Geophys. Res., 102*, 14,141,.

Bourdarie, S., D. Bosher, T. Beutier, J. A. Sauvaud, M. Blanc, and R. H. W. Friedel (1996), A physics based model of the radiation belt flux at the day timescale, in Proceedings of the Symposium on Environment Modelling for Space-Based Applications, SP-392, pages 159-163, ESA, ESA Publications Division, ESTEC, Noordwijk, The Netherlands.

Brautigam, D. H. and J. M. Albert (2000), Radial diffusion analysis of outer radiation belt electrons during the October 9, 1990, magnetic storm, *J. Geophys. Res., 105(A1)*, 291.

Carpenter, D. L., and R. R. Anderson (1992), An ISEE/whistler model of equatorial electron density in the magnetosphere, *J. Geophys. Res., 97*, 1097.

Chen Y., R. H. W. Friedel, G. D. Reeves (2006), Phase space density distributions of energetic electrons in outer radiation belt during two GEM IM/S selected storms, *J. Geophys. Res.*, in press, doi: 10.1029/2006ja011703.

Freeman, J. W., R. A. Wolf, R. W. Spiro and B. Hausman (1994), A real-time magnetospheric specification model, Rice University final report on USAF contract.

Gussenhoven, M. S., D. A. Hardy, and N. Heinemann (1983), Systematics of the equatorward diffuse auroral boundary, *J. Geophys. Res., 88*, 5692.

Hilmer, R. V., and G.-H. Voigt (1995), A magnetospheric magnetic field model with flexible current systems driven by independent physical parameters, *J. Geophys. Res., 100(A4)*, 5613.

Hilmer, R. V., G. P. Ginet and T.E. Cayton (2000), Enhancement of equatorial energetic electron fluxes near L = 4.2 as a result of high speed solar wind streams, *J. Geophys. Res. ,105(A10)*, 23,311.

Horne, R. B., and R. M. Thorne (1998), Potential waves for relativistic electron scattering and stochastic acceleration during magnetic storms, *Geophys. Res. Lett., 25*, 3011..

Lanzerotti, L.J., and C.G. Morgan (1973), ULF geomagnetic power near L=4, 2, temporal variation of the radial diffusion coefficient for relativistic electrons, *J. Geophys. Res., 78*, 4600.

Lanzerotti, L.J., D.C. Webb, and C.W. Arthur, Geomagnetic field fluctuations at synchronous orbit, 2 (1978), Radial diffusion, *J. Geophys. Res., 83*, 3866.

Li, X., M. Temerin, et al. (2001), Quantitative prediction of radiation belt electrons at geostationary orbit based on solar wind measurements, *Geophys. Res. Lett., Vol 28(9)*, 1887.

Mead, G. D., Deformation of the geomagnetic field by the solar wind (1964), *J. Geophys. Res., 69*, 1181.

Meredith, N.P., M. Cain, R.B. Horne, R.M. Thorne, D. Summers, and R.R. Anderson (2003), Evidence for chorus-driven electron acceleration to relativistic energies from a survey of geomagnetically-disturbed periods, *J. Geophys. Res., 108(A6)*, 1248.

Meredith, N. P., R. B. Horne, S. A. Glauert, R. M. Thorne, D. Summers, J. M. Albert, and R. R. Anderson (2006), Energetic outer zone electron loss timescales during low geomagnetic activity, *J. Geophys. Res., 111*, A05212.

Paulikas, G. A., and J. B. Blake (1979), Effects of the solar wind on magnetospheric dynamics: Energetic electrons at the synchronous orbit, in Quantitative Modeling of Magnetospheric Processes, Geophys. Monogr. Ser., Vol. 21, edited by W. P. Olson p. 180, AGU, Washington, D. C..

Roederer, J.G. (1970), *Dynamic of Geomagnetically Trapped Radiation*, Springer-Verlag, New York.

Schulz, M. ,J. F. Lemaire, D. Heynderickx and D. N. Baker, Canonical Coordinates for Radiation-Belt Modeling. Radiation Belts: Models and Standards, Washington, D. C., Am. Geophys. Un.: 153-160.

Schulz, M., and L.J. Lanzerotti (1974), *Particle Diffusion in the Radiation Belts*, Spring-Verlag, New York.

Selesnick, R. S., J. B. Blake and R. A. Mewaldt (2003), Atmospheric losses of radiation belt electrons, *J. Geophys. Res., 108(A12)*, SMP 28.

Shabansky, V. P., Some processes in the magnetosphere (1971), *Space Sci. Rev., 12*, 299.

Summers, D., R. M. Thorne, and F. Xiao (1998), Relativistic theory of wave particle resonant diffusion with application to electron acceleration in the magnetosphere, *J. Geophys. Res., 103*, 20,487.

Summers, D., and C.-Y. Ma (2000), Rapid acceleration of electrons in the magnetosphere by fast mode MHD waves, *J. Geophys. Res., 105*, 15,887.

Tóth, G., et al. (2005), Space Weather Modeling Framework: A new tool for the space science community, *J. Geophys. Res., Vol. 110*, 12,226.

Tsurutani, B. T., W. D. Gonzalez, et al. (1995), Interplanetary origin of geomagnetic activity in the declining phase of the solar cycle, *J. Geophys. Res.,100(A11)*, 21,717.

Tsyganenko, N. A. (2002), A model of the near magnetosphere with a dawn-dusk asymmetry 2. Parameterization and fitting to observations, *J.Geophys. Res., 107(A8)*, 1176.

West, H. I., R. M. Buck and G. T. Davidson (1981), The Dynamics of Energetic Electrons in the Earth's Outer Radiation Belt During 1968 as Observed by the Lawrence Livermore National Laboratory's Spectrometer on Ogo 5, *J.Geophys. Res., 86(A4)*, 2111.

Y. Y. Shprits and R. M. Thorne (2004), Time dependent radial diffusion modeling of relativistic electrons with realistic loss rates, *Geophys. Res. Letts., Vol 31*, L08805.

Chen, Y. , G. D. Reeves, R. H. W. Friedel, A. Varotsou, T. E. Cayton,(2006), Phase space distribution of outer radiation belt relativistic electrons: From CRRES and GPS observations inside geosynchronous orbit, Cospar 2006.

Vette, J. (1991), The AE-8 trapped electron model environment, National Space Science Data Center, Report 91-24, Greenbelt, Maryland.

Chapter 3

MHD-Particle simulation of a high-speed stream storm

3.1 Introduction

Over the past few decades, many empirical and numerical models [*Li* et al., 1993; *Hudson* et al., 1997, *Elkington* et al., 2000] have been developed to trace the variations of the fluxes of outer radiation belt electrons. One important approach is to utilize numerical methods to solve the Fokker-Planck equations [*Bourdarie et al.*, 1996; *Schulz*, 1996; *Shprits et al.*, 2005]. However, as we have described in chapter two, it is usually difficult to estimate relevant transport coefficients exactly.

Another method, which is more fundamental and direct, is MHD-Particle simulation. This approach tracks radiation belt dynamics by tracing the guiding center of test particles in the MHD electric and magnetic fields and using Liouville's theorem to evolve an initial phase space density. However, even considering the great advances in computational power and parallel techniques, it is still very time consuming to trace the trajectories of a large number of particles at each time step.

In this research work, we introduce a new algorithm, adapted from Nunn's Vlasov Hybrid Simulation (VHS) method [*Nunn*, 1993], and couple it with a MHD-Particle code developed by *Elkington et al.* [2002]. The new algorithm has the advantage of making more efficient use of test particles. As a result, the computational performance has been greatly enhanced. Another positive feature is that with the new technique we can simulate the dynamic boundary conditions and loss lifetime of electrons easily.

Using the new radiation belt model, we have simulated the evolution of the outer radiation belt during one typical high-speed solar wind storm event. Good agreement between the simulation results and the satellite measurements of energetic particles in the outer radiation belt is obtained.

We have also calculated the radial diffusion coefficients from Fourier analysis of the global MHD fields. Using the newly calculated coefficients, we ran our radial diffusion model described in chapter two for this storm event. The computational results are briefly discussed.

The remainder of this chapter is organized as follows: a global MHD code, "LFM code", and a two-dimensional test-particle code are described in section 3.2. In section 3.3, we introduce Nunn's VHS method. A new method to calculate the phase space density of electrons is fully developed in section 3.4. In section 3.5, a case study of the January 1995 storm event is presented. The simulation results of this event are discussed in section 3.6. Sections 3.7 and 3.8 are mainly about the calculation of diffusion coefficients from the power spectrum of MHD fields. Further, we ran our radial transport model of chapter two using the new radial diffusion coefficients and the results are discussed in section 3.9. Finally, conclusions and discussion are presented in section 3.10.

3.2 MHD Particle Simulation Code

In this work, we use a test-particle simulation code, which was developed by *Elkington et al.* [2002] and can track the "guiding center" drift motion of relativistic particles in the magnetohydrodynamic (MHD) electromagnetic fields.

3.2.1 Lyon-Fedder-Mobarry MHD code

MHD simulation is one valid and practical approach to simulate the earth's electromagnetic fields by solving the following ideal MHD equations (for some in-depth discussion of these equations, refer to the book *Plasma Dynamics* by *R.O. Dendy* [1990]) :

$$\text{Continuity}: \frac{\partial \rho}{\partial t} + \mathbf{u} \bullet \nabla \rho + \rho \nabla \bullet \mathbf{u} = 0$$

$$\text{Momentum}: \rho \frac{\partial \mathbf{u}}{\partial t} + \rho \mathbf{u} \bullet \nabla \mathbf{u} + \nabla p - \mathbf{j} \times \mathbf{B} = 0$$

$$\text{Induction}: \frac{\partial \mathbf{B}}{\partial t} + \nabla \times \mathbf{E} = 0 \tag{3.1}$$

$$\text{Pressure}: \frac{\partial p}{\partial t} + \mathbf{u} \bullet \nabla p + \gamma p \nabla \bullet \mathbf{u} = 0$$

In order to solve the above equations, *J. G. Lyon, J. A. Fedder* and *C. Mobarry* [*Fedder et al.*, 1995a; *Mobarry et al.*, 1996] developed a three-dimensional, numerical simulation code, which is commonly called "LFM global MHD code". This code uses time-dependent solar wind data as input parameters and can reproduce the dynamic topology of the earth's electromagnetic fields from 30 to -300 R_E in the X direction of solar magnetic coordinates, 100 to -100 R_E in both Y and Z directions.

3.2.2 Guiding-Center Particle Simulation

The LFM model can provide the global MHD magnetic fields. In this section, a test particle code which traces the guiding center motion of particles in the MHD fields will be described.

As mentioned in section 3.1, test particle simulation is one method to calculate the dynamics of high energy particles in the outer radiation belt. It directly traces the trajectories of these charged particles in the electric and magnetic fields of the earth by solving guiding center

equations. Guiding center equations are used because it is impractical to integrate the full Lorentz equations of motion, due to the short period of the gyration for these energetic particles (~ ms). We use the following relativistic guiding center equations derived by *Brizard* and *Chan* [1999]:

$$\frac{d\vec{r}}{dt} = c\frac{\vec{E} \times \hat{b}}{B_{//}^*} + \frac{Mc}{q\gamma}\frac{\hat{b} \times \nabla B}{B_{//}^*} + \frac{p_{//}^2}{\gamma m_0}\frac{\vec{B}^*}{B_{//}^*},$$ (3.2)

$$\frac{dp_{//}}{dt} = \frac{B^*}{B_{//}^*}(q\vec{E} - \frac{M}{\gamma}\nabla B),$$ (3.3)

with

$$\vec{B}^* = \vec{B} + \frac{cp_{//}}{q}\nabla \times \hat{b},$$ (3.4)

$$B_{//}^* = \hat{b} \bullet \vec{B}^* = B(1 + \frac{cp_{//}}{qB}\hat{b} \bullet \nabla \times \hat{b}).$$ (3.5)

Here $\hat{b}$ is the unit vector in the direction of the local magnetic field; the three items on the right side of equation (3.2) represent "E X B" drift, "grad-B" drift and "curvature drift", respectively.

If we assume that $V_{//}$ and $\nabla_{//}$ equal zero, we can get the 2D guiding-center equations on the equatorial plane from equation (3.2) and (3.3)

$$\frac{\partial r}{\partial t} = c\frac{E_\phi}{B} + \frac{Mc}{q\gamma r}\frac{\partial_\phi B}{B},$$ (3.6)

$$\frac{\partial \phi}{\partial t} = -c\frac{E_r}{rB} - \frac{Mc}{q\gamma r}\frac{\partial_r B}{B}$$ (3.7)

In this research work, we use a 2D test particle simulation code developed by *Hudson et al.* [1996] and *Elkington et al.* [2002]. The code uses the electric and magnetic fields from LFM runs to track the motion of high energy particles on the equatorial plane.

In this code, at the initial time, test particles are distributed randomly in a polar coordinates, with $3.5\,\mathrm{Re} < r < 10\,\mathrm{Re}$ and $0 < \phi < 2\pi$.

Then at each time step, the particles are pushed by the LFM MHD fields. An adaptive 4th order Runge-Kutta method [*Cash* and *Karp*, *1990*] has been applied in this model to solve the above equations (3.6) and (3.7). Another important thing that should be noted is that the code comes with "free boundary" conditions, which means if a particle moves out of the magnetopause, we will assume it is lost and stop tracing its orbit.

3.3 Vlasov Hybrid Simulation technique

The Vlasov Hybrid Simulation (VHS) method is a new technique developed by *D. Nunn* [1993] for the numerical simulation of hot collision-free particles. Traditional particle simulation methods, particle-in-cell (PIC) or cloud-in-cell (CIC) method, put a large number of test particles into the simulation space and trace their orbits and behaviors to examine the characteristic of real particles, which is usually very time-consuming. In the VHS method, every test particle carries the information of the whole vlasov fluid at the single point and can be used to calculate the distribution function of the fluid. Nunn shows that the method makes very efficient use of these test particles and greatly enhances the computational performance.

The following features are some benefits which come from the new method:

1) Compared to other methods, VHS usually has low noise levels.

2) No numerical diffusion of the distribution function is needed in order to attain stability.

3) Dynamic boundary conditions could be realized by changing the information carried by particles at the boundary. Adding new particles or removing old particles at the boundary to change the boundary conditions is no longer necessary.

3.4 Calculation of phase space density

We have combined the novel VHS technique with the MHD-Particle simulation code to simulate the dynamics of high energy electrons in the outer radiation belt.

We construct a phase space simulation box which ranges from -10 to 10 R_E in both X and Y directions. This domain is divided into a number of squares with constant grid size of 0.1 R_E. Any particle outside the simulation box is removed from the simulation.

The initial conditions of the particles in the MHD-Particle code introduced a bias toward inner regions, which means the density of test particles decreases as the radius of the location increases. To adjust for this, we give each particle an extra weight r_0/r_i to remove the low-r bias, where r_0 is the initial radius of each particle and r_i is the minimum initial radial distance covered by the simulation (here $r_i=3.5$).

Once the initial bias has been removed, we assign each particle a phase space density f_0 from the AE8 empirical model [*Vette*, 1991]. The MHD-Particle simulation gives the positions of all these particles at subsequent time steps. By Liouville's theorem, the phase space density of these particles will be conserved along the particle trajectory. Note that it is helpful to regard these particles as "markers" which carry a certain weighted PSD, rather than as individual particles. At each time step, we interpolate the phase space density of these particles onto fixed grid points

according to an area (2D) or volume (3D) weighting algorithm. Figure 3.1 shows the PSD at one grid point, which is calculated from the PSD of particles in the four closest cells of the two dimensional phase space:

$$f_{grid} = \frac{\sum_{k=1}^{N} f_k \frac{A_k}{A} \frac{r_k}{r_i}}{\sum_{k=1}^{N} \frac{A_k}{A} \frac{r_k}{r_i}} .$$

(3.8)

Here N is the number of particles in the four closest cells. f_{grid} is the phase space density at the grid point, which is calculated from the phase space density f_k of all the N particles.
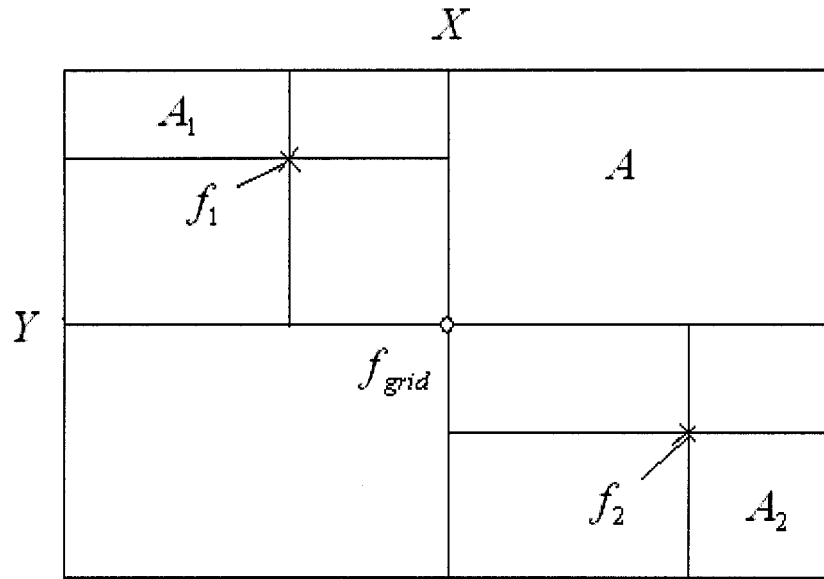
Figure 3.1 Interpolation of Phase Space Density from each particle onto the fixed grid point according to the area weighting algorithm.

3.5 High-speed solar wind stream event: the January 1995 storm

In this section, we select the January 1995 storm event as a test case since it is a fairly typical high-speed stream storm event. Although it is a moderate storm, satellite observations show sustained increase of the electron fluxes both at geosynchronous orbit and at GPS spacecraft locations.

This storm is a typical high-speed solar wind stream event, both in terms of the long lasting recovery phase (up to a few days) and high enhancement of fluxes of energetic electrons in the outer radiation belt. Figure 3.2 plots the measured solar wind conditions and geomagnetic indices during this storm.
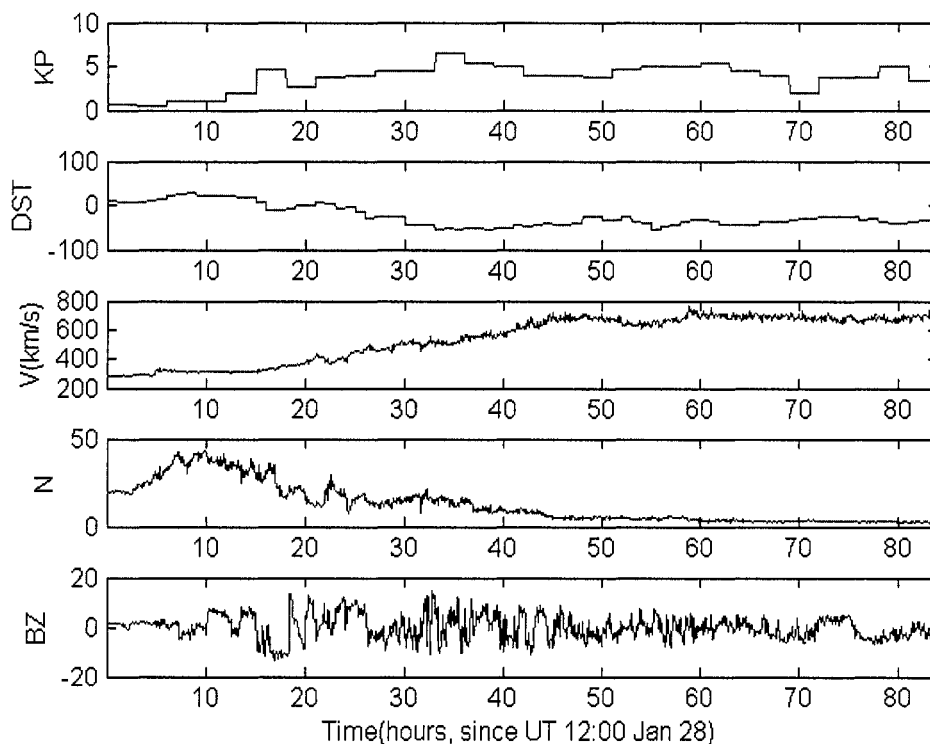
Figure 3.2 Solar wind conditions and geomagnetic indices for the high-speed-stream storm event in January, 1995.

From figure 3.2 the initial increase in *Dst* was associated with a low-speed but high-density solar wind stream, which began at about UT 13:00 on January 28, 1995 and reached the peak with the density of 44 cm^{-3} at UT 22:00. Following that high density stream, the *Kp* index gradually increased accompanied by high fluctuations of IMF *Bz*. Both of these were associated with the arrival of a high-speed, low-density solar wind stream. At the same time, the *Dst* index began to decrease and reached the minimum value at UT 3:00 on January 30. The minimum *Dst* around -55nT indicated it was only a moderate storm. Next, the long and slow recovery phase of the storm event was characterized by the long-lasting high-speed solar wind stream and high *Kp* index.

The response of energetic electrons in the outer radiation belt was observed by both GPS satellites and geosynchronous satellites. The fluxes of these particles increased several orders of magnitude during the recovery phase. In section 3.6, we will discuss these data in more detail and also compare them with our simulation results.

3.6 Simulation results

Figure 3.3 shows the MHD-Particle simulation results for radiation belt electrons with first invariant $M = 2100$ MeV/G during the 1995 January storm event [*S.R.Elkington*, 2006]. These electrons are pushed by LFM MHD fields and move on the equatorial plane. In this run, the inner boundary is fixed at 3.5 R_E and the outer boundary is set at 10 R_E. If a particle moves outside either of these boundaries, the particle trajectory is no longer calculated. In figure 3.3, the solid lines represent the contours of constant magnetic field from the LFM Model and the dashed lines are the contours of constant radial distance at 2 R_E, 5 R_E and so on. Different colors stand for

electrons of different energies. Simulation results show severe magnetopause loss events in the

early hours of January 29, 1995 (between panel b and c).
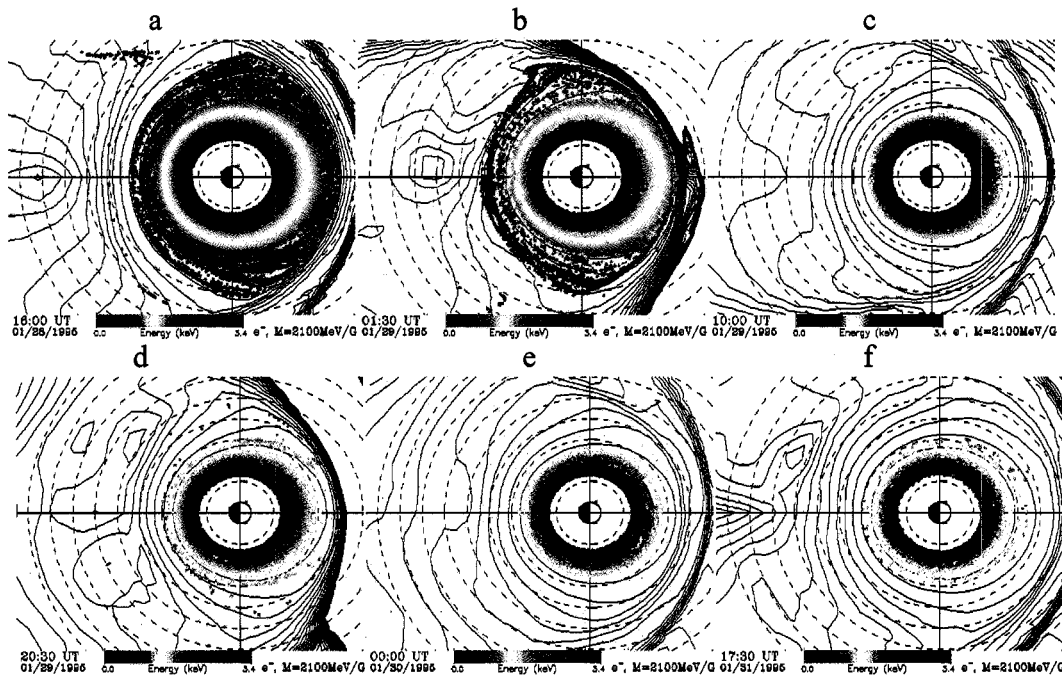
Figure 3.3   Snapshots of the MHD/Particle simulation for January 1995 storm event by *S.R. Elkington* [2006].

The top-left panel of figure 3.3, panel a, shows the distribution of these energetic electrons at

UT 16:00 on January 28. Combined with figure 3.2, we know it was in the initial phase of this

storm. These particles extended from 3.5 R_E to 10 R_E and the magnetic field was not highly

disturbed. Panel b represents the simulation results at UT 1:30 on January 29, showing the

response to the arrival of high-density solar wind stream at 10h in figure 3.2. The increase of the

plasma density led to an enhancement in the solar wind ram pressure, which caused the

compression of the geomagnetic field shown in panel b. As a result of the compression, some of

the energetic electrons in the outer magnetic field were lost outside the magnetopause. In panel c,

the loss effect is more apparent. At UT 10:00 on January 29, most of the particles that have radial distances larger than 6 R_E have been lost. Panel d shows the distribution of these particles at UT 20:30 on January 29. The distribution of the plasma outside 6 R_E has partially recovered. Since the simulation was undertaken with the condition of "free boundary" and no plasma sheet source, these electrons could only come from the outward diffusion of pre-existing particles in the inner magnetosphere. Soon after UT 20:30 (panel d), the magnetosphere was compressed again with the arrival of the high-speed solar wind stream, causing the second loss of these electrons in the outer region shown in panel e. Panel f shows the distribution of these electrons at UT 17:30 on January 31. At this stage, the storm entered the slow recovery phase. Figure 3.3 is essentially a plot of the locations and energies of the electron markers.

The calculation of phase space density for these electrons was made, using the new method described in section 3.4. Figure 3.4 plots the simulation results (red lines) both at 6.0 R_E and at 4.2 R_E. In this simulation the phase space density is averaged around a contour of constant radial distance.

linear parameters, which are calculated through solving the linear equation at R=4.2 R_E and R=6.0 R_E.

Also, it is natural to compare the simulated PSD at R=6.6 R_E with GEO satellite measurements. However, for this storm event we used the simulation results at 6 R_E instead of at 6.6 R_E for the comparison, because in the simulation, most test particles outside 6 R_E were lost due to the strong compression of the geomagnetic field. The statistical error in the calculation of the PSD at 6.6 R_E is large due to an insufficient number of particles in the cells along the geosynchronous orbit. It appears that the LFM simulation yields a magnetosphere which is smaller than the real magnetosphere and so we adjust for this by comparing simulation results at R=6 R_E rather than R=6.6 R_E.

From figure 3.4, the simulated phase space density at R=6 R_E shows a strong decrease, especially from t=15 to 23 h, which also corresponds to the severe magnetopause loss event (refer to panel c of figure 3.3). After a short while, though, the simulated phase space density at R=4.2 R_E began to increase. This increase is the result of inward diffusion of the pre-existing particles.

Also plotted in figure 3.4 are the observations from geosynchronous satellites and GPS satellites. The solid blue line is the observed phase space density for M =2100 MeV/G electrons at 6.6 R_E, which is the average value of the data collected by Los Alamos satellites: 1984-129, 1991-080, 1987-097, 1989-046, 1990-095, and 1994-084. The two blue dashed lines are the measurements at R=4.2 R_E, which show the phase space density of energetic electrons having the first adiabatic invariant M ~ 1000-3300 MeV/G, by GPS Navstar Satellites NS-24 and NS-28.

These observations show a dropout of phase space density during the main phase of the storm and enhancements during the long recovery phase.

However, the simulation results of figure 3.4 do not catch the above features of the data. Note that these simulations effectively model a free-boundary condition and have no electron loss mechanism apart from magnetopause loss. In the following sections, we present the improved results using more realistic outer boundary condition and then adding a loss lifetime model.

The model results for the same event but with dynamic outer boundary conditions from the GEO satellite measurements are presented in figure 3.5. To represent the dynamic boundary conditions, at each time step we set the phase space density of the markers with the radial distance higher than 6 R_E to be the average value measured by GEO satellites (blue solid line).

The loss event at t=20h introduced large statistical errors due to an insufficient number of particles in the cells near the outer boundary. To diminish the errors and get better statistical results, we added some new markers at t=24h. All new particles were uniformly distributed and their phase space densities were assigned the values at the preceding time step (In this case, the values at 23.5h were assigned since the time step is half an hour). Introducing new particles may disturb the profile of the PSD. To test the impact of new particles, we plot the profiles of the PSD before adding new particles and again after the insertion of these particles.
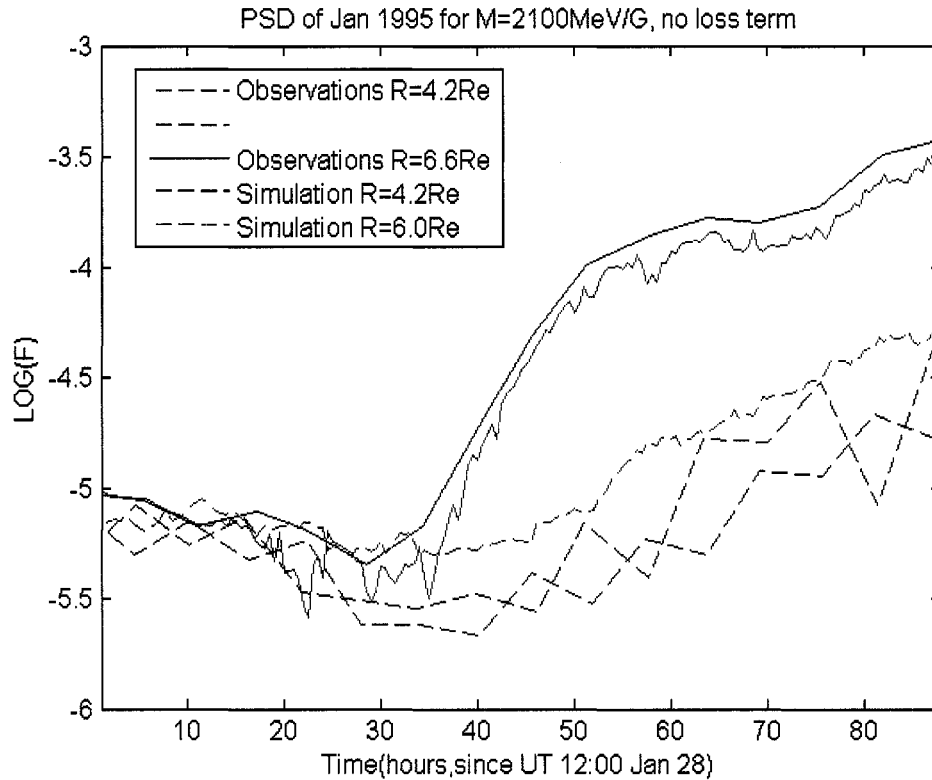
Figure 3.5 Simulated (red) and observed (blue) phase space density of the energetic electrons (M=2100 MeV/G) for the HSSWS event in January, 1995. Here the model uses the dynamic outer boundary conditions from the observations and assumes an infinite electron lifetime.

Figure 3.6 shows that the newly inserted particles did not disturb the PSD profile inside the outer boundary. The differences between the two profiles of PSD outside the boundary comes from the fact that the average PSD over the contour of constant R will decrease if some cells along the contour do not have any particles inside. Therefore, the graph also proves that adding new particles can help to remove the errors caused by an insufficient number of particles outside the simulated trapping boundary.

Figure 3.5 shows that the simulated PSD at the outer boundary (solid red line) is still slightly

smaller than the GEO observations (solid blue line) even after adding the new markers. This is

because some newly added markers near the outer boundary were lost again. We regard the

simulated PSD at R=6 R_E sufficiently close to the observed PSD at R=6.6 R_E.

The change of PSD profile before and after adding the new particles
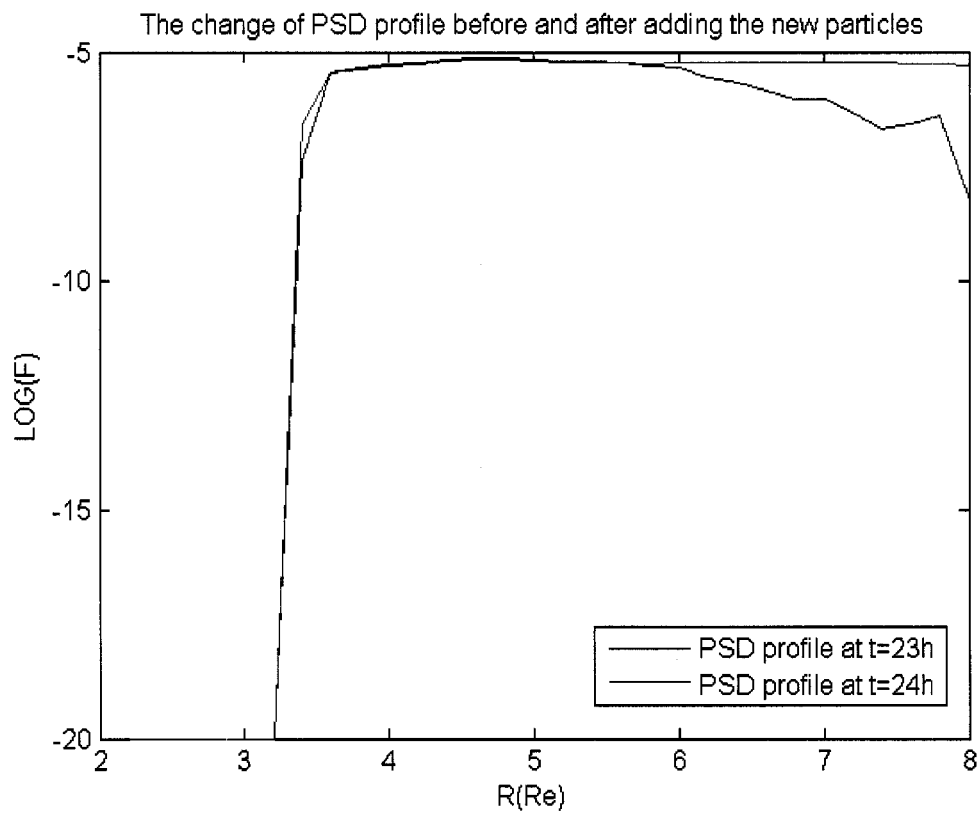
Figure 3.6 PSD profiles at t=23h (before adding new particles) and t=24h (after adding

particles).

Compared with figure 3.4, the results in figure 3.5 are more consistent with the satellite data

during the recovery phase of the storm event. However, there are still significant differences,

specifically, the simulated phase space density at R=4.2 R_E is still slightly larger than the

measurements and the drop out during the main phase, which is observed in the data, is not

reproduced in the simulation results. The latter may be due to the weak ring current in the MHD

fields; as described in chapter two, a weak ring current leads to weak "Dst effect". However,

considering that this storm is only a moderate storm, we expect the Dst effect to be fairly weak,

especially at R=4.2 R_E. Another reason for the difference, which is probably more important, is

the effect of pitch angle scattering causing loss of electrons. To correct the discrepancy, we

added the electron decay lifetime model described in section 2.4 into our model. New simulation

results are shown in figure 3.7.
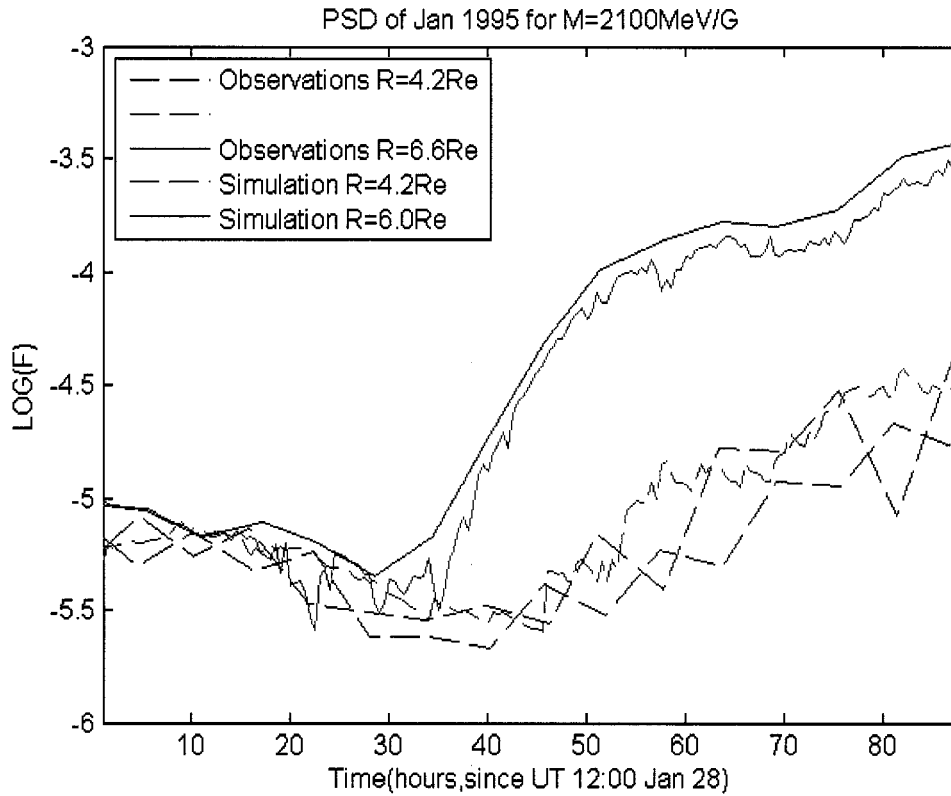


Figure 3.7 Simulated (red) and observed (blue) phase space density of the energetic electrons

(M=2100 MeV/G) for the HSSWS event in January, 1995. Here model uses the dynamic outer

boundary condition and decay lifetime of electrons based on the observations.

In figure 3.7, agreement between the simulation results and the observations is very good except that during the later recovery phase the simulated PSD at R=4.2 R_E is slightly above the GPS observation. However, considering the wide pass-bands of the GPS particle detector and no local time average of GPS data, we can still conclude that our new method is improved.

Figures 3.4, 3.5, and 3.7 indicate the importance of realistic outer boundary conditions and electron decay lifetime (loss term). Both are necessary to better reproduce the real event. The outer boundary condition plays an important role in the high enhancement of PSD in the center of the outer radiation belt. The inward diffusion of pre-existing particles may also contribute to the increase. A realistic model of electron decay lifetime is needed to better reproduce the decrease in PSD during the main phase. It is also important but not dominant during the recovery phase of the storm.

The color graph of figure 3.8 shows the same simulated phase space density as figure 3.7, but plotted as a function of radial distance and time. Between t=0 and t=40 h, an obvious decrease was observed for all locations. Just following this period, a significant increase in PSD at the outer boundary began at t=40 h. After that, we observed an apparent inward diffusion from the outer boundary to the inner magnetosphere. As the result, the PSD in the inner magnetosphere was greatly enhanced.
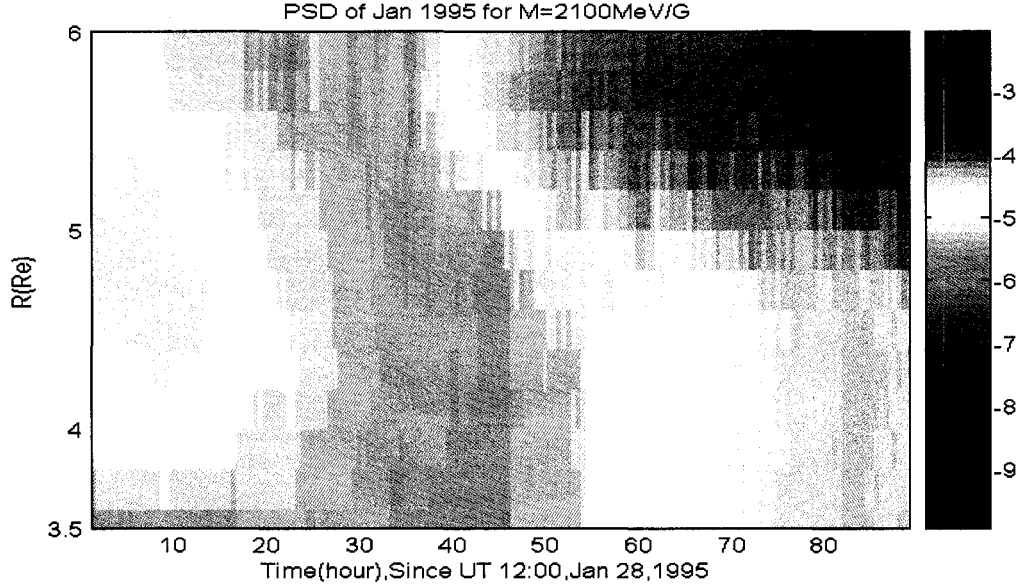
Figure 3.8 Modeling results for phase space density of electrons with M = 2100 MeV/G during 1995 January storm event.

3.7 Electric and magnetic power spectra

Besides the MHD-particle simulation, the analysis of radial diffusion processes is another valid method to study the particle dynamics in the radiation belt. One critical step in the study of radial diffusion is to estimate the radial diffusion coefficient. In 1965 and early 1970s, theoretical formulae for the calculation of radial diffusion coefficients due to the electric and magnetic fluctuations were developed [*Falthammar*, 1965; *Schulz and Lanzerotti*, 1974]. However, these formulae are based on the simple assumption of a symmetric dipole magnetic field and specific assumptions about the perturbations that produce the diffusion. Recently, *Fei et al.* [2006] extended these results. They derived analytical radial diffusion coefficients both in symmetric and asymmetric background electromagnetic fields.

In this section we use the *Fei et al.* formulae and power spectral densities of MHD waves from the LFM fields to calculate radial diffusion coefficients for this January 1995 storm event. *Fei et al.* [2006] give the following formulae for radial diffusion coefficients due to electric and magnetic field perturbations:

$$D_{LL}^{E,Sym} = \frac{L^6}{8R_E^2 B_0^2} \sum_m P_m^E (m\Omega_0),$$

$$D_{LL}^{M,Sym} = \frac{M^2}{8q^2\gamma^2 B_0^2 R_E^4} L^4 \sum_m m^2 P_m^M (m\Omega_0). \qquad (3.10)$$

Here B_0 is the magnetic field value at the surface of the earth (0.317 gauss); R_E is the earth's radius (6300 km); Ω_0 is the energy-dependent drift frequency; m is the azimuthal mode number and P^E, P^M are the power spectral density of the azimuthal electric and compressional magnetic field fluctuations evaluated at harmonics of the drift frequency. Note that Fei's formulas also have asymmetric terms, but they were shown to be small for a storm in September 1998 and they are expected to be even smaller for this January 1995 storm since it is weaker and less asymmetric.

Figure 3.9 and 3.10 respectively represent the variations of the power spectrum of the electric field, which are analyzed over the frequency range 0.14~10 mHz, as a function of time and mode number m at R=4.2 R_E and 6.6 R_E. Through the plots, the dominant terms are low mode numbers, which suggest that when we use equation (3.10) to calculate D_{LL}, the higher mode terms can be ignored. Also, the plots show the significant enhancement of the total power of electric field at roughly t = 34 h, which is also the time when the *Dst* index was at its minimum and *KP* index reached the maximum value. The large increase of the power led to a

strong inward radial diffusion at almost the same time, which is indicated by the apparent

increase of phase space density at R=4.2 R_E (refer to figure 3.7).
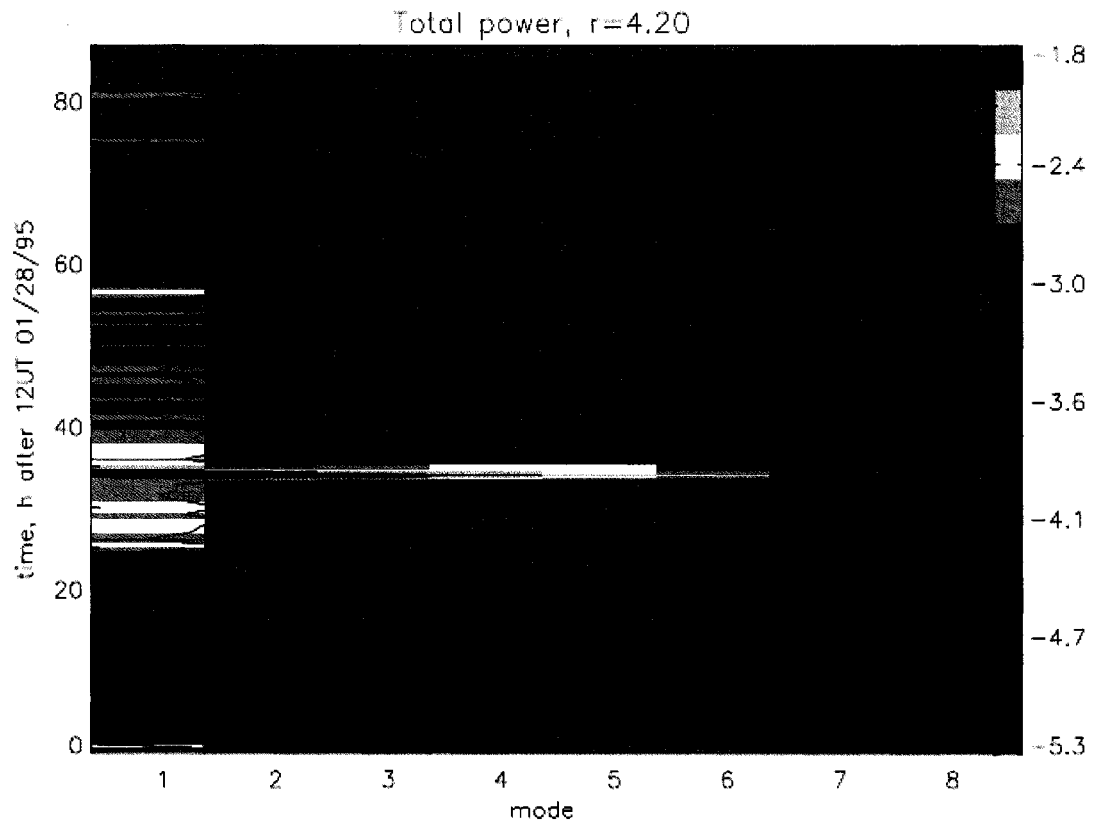
Figure 3.9 The power as a function of time and the resonant modes for the electric field at R=4.2 R_E (Log(P_m), $mV^2m^{-2}Hz^{-1}$).
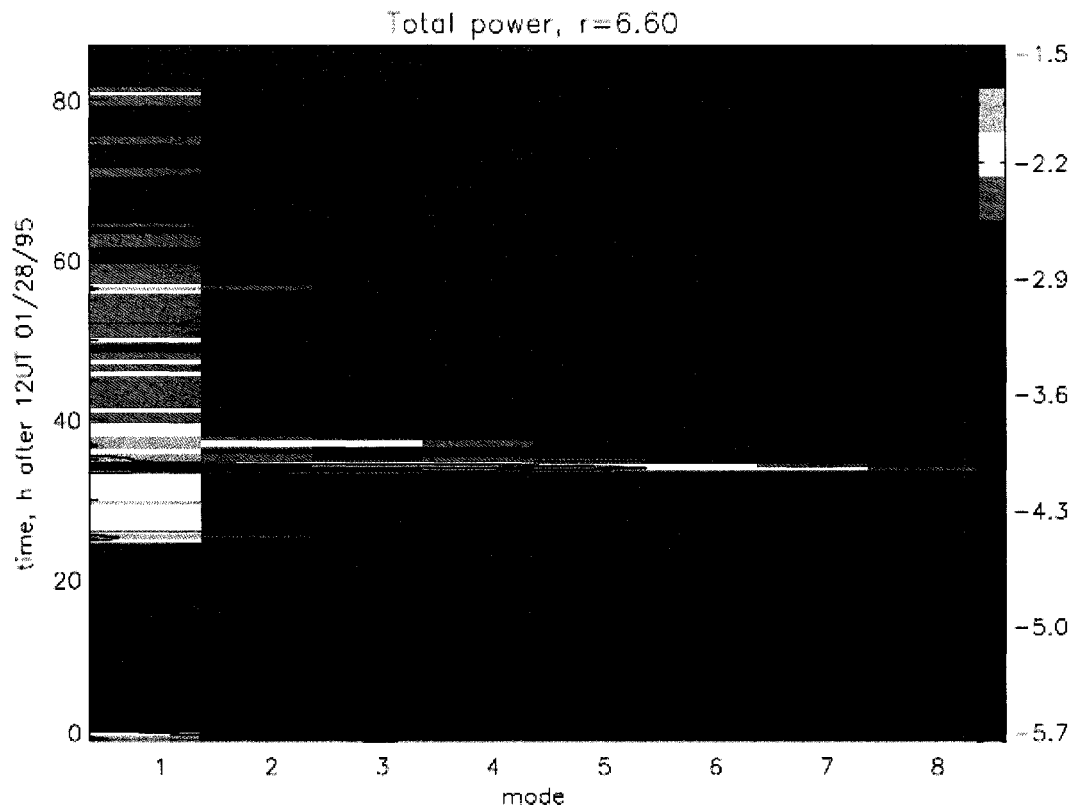
Figure 3.10 The power as a function of time and the resonant modes for the electric field at R=6.6 R_E (Log(P_m), $mV^2m^{-2}Hz^{-1}$).

The power of magnetic fields at R=4.2 R_E and 6.6 R_E are plotted in figure 3.11 and 3.12. These plots show features similar to the electric field power: the power appears dominantly in low mode-numbers and display an obvious increase at t=34 h. Figure 3.12, though, reveals a wider distribution of the power in higher mode numbers and another increase at t=16 h. The two increases in the magnetic field power at R=6.6 R_E are directly associated with the compression of the magnetic fields by the solar wind streams (refer to figure 3.2).
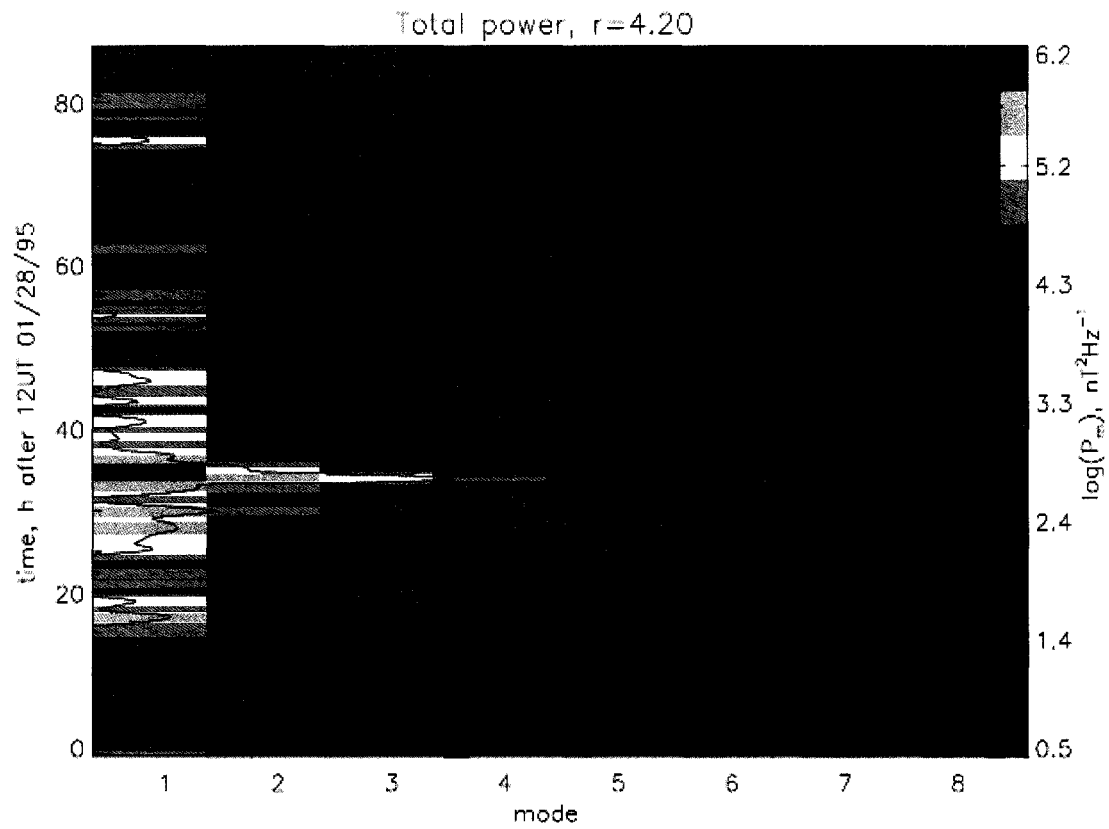
Figure 3.11 The power as a function of time and the resonant modes for the magnetic field at r=4.2 R_E (Log(P_m), nT^2Hz^{-1}).
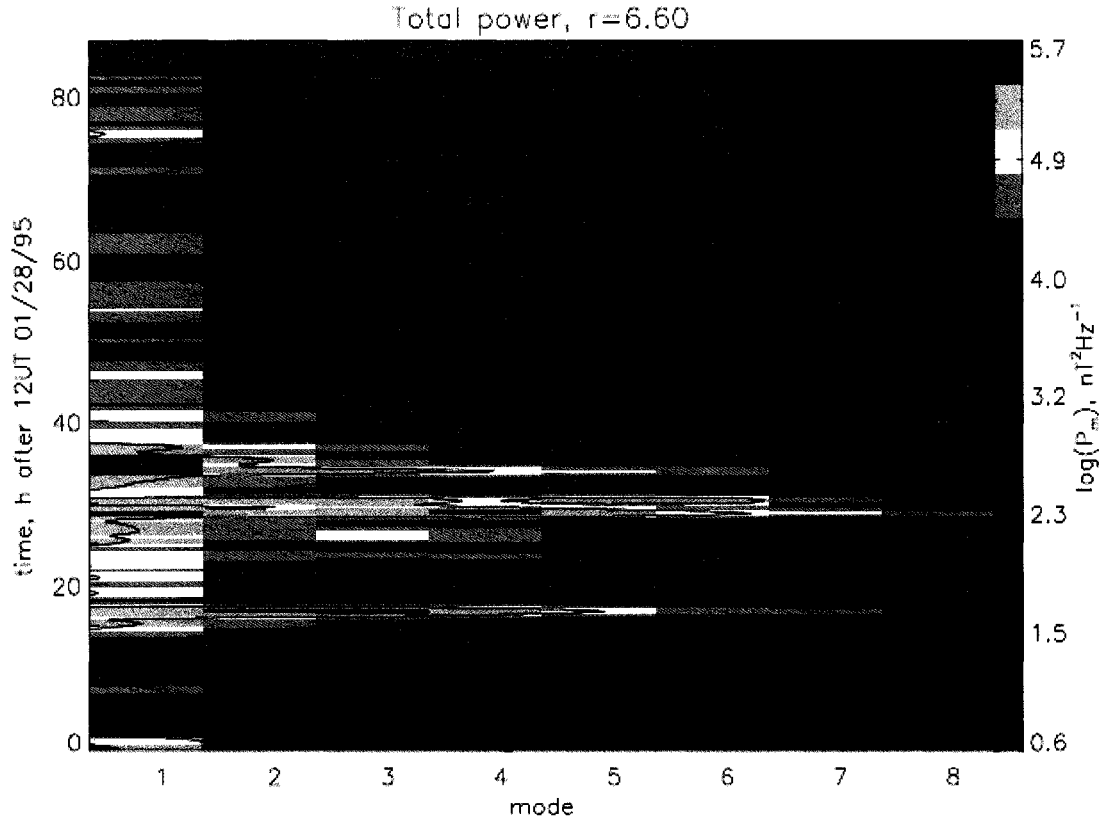
Figure 3.12 The power as a function of time and the resonant modes for the magnetic field at

r=6.6 R_E (Log(P_m), nT^2Hz^{-1}).

3.8 Radial diffusion coefficient D_{LL}

According to equation (3.10), the radial diffusion coefficient is highly dependent on the fluctuations of electric and magnetic fields. We calculated D_{LL} from the wave powers obtained from global MHD simulations. In order to do that, we need to sum the powers over all mode numbers m, which is usually impractical. Fortunately, from figure 3.9-3.12, we found most of

the powers are contained in low mode numbers, so we only sum the powers from m=1 to 3, as in *Fei et al.* [2006].

Figure 3.13 shows the calculated results at UT 22:00 on January 29, 1995, which corresponds to the main phase of the storm. As mentioned previously, the plot of power spectrums show an apparent enhancement at this time. From figure 3.13, it is apparent that D_{LL}^E has a steeper R dependence than D_{LL}^M. Compared the plot of D_{LL}^E with that of D_{LL}^M, we found that at low radial distance (R = 3.5 ~ 6 R_E), D_{LL}^M is much larger than D_{LL}^E. However, in the region of R>6 R_E, the value of D_{LL}^E is comparable to that of D_{LL}^M.

Earlier theoretical research work and particle observations have shown that the radial transport rate has a strong L-dependence. In 2000, *Brautigam* and *Albert* applied the expression $D_{LL}^M(KP,L) = 10^{aKP-b} L^{10}$ to fit D_{LL} values obtained from observations by *Lanzerotti* and *Morgan* [1973] and *Lanzerrotti et al.* [1978]. Based on the discrete observations, they derived the following analytic equation:

$$D_{LL}^M(Kp,L) = 10^{(0.506 Kp - 9.325)} L^{10} \qquad (3.11)$$

However, *Barker et al.* [2005] and *Fei et al.* [2006] found if the L-dependence of the magnetic diffusion coefficient is less steep, the simulation results are more consistent with the observations. Fitting straight lines to the values in figure 3.13 yields

$$D_{LL}^E(L) = 10^{-7.345} L^{9.488},$$

$$D_{LL}^M(L) = 10^{-4.474} L^{5.783}. \qquad (3.12)$$

In the above expressions D_{LL}^M is less steep than the formula in equation (3.11).

In figure 3.13, we also compared the simulation results with the real data (x symbol) collected

by *Lanzerotti and Morgan* [1973] and *Lanzerrotti et al.* [1978]. There is reasonable agreement

between the calculated D_{LL}^M and observations. For reference, a straight line between the two

Lanzerotti and *Morgan* points gives $D_{LL}^M(L) = 10^{-5.468} L^{6.97}$.
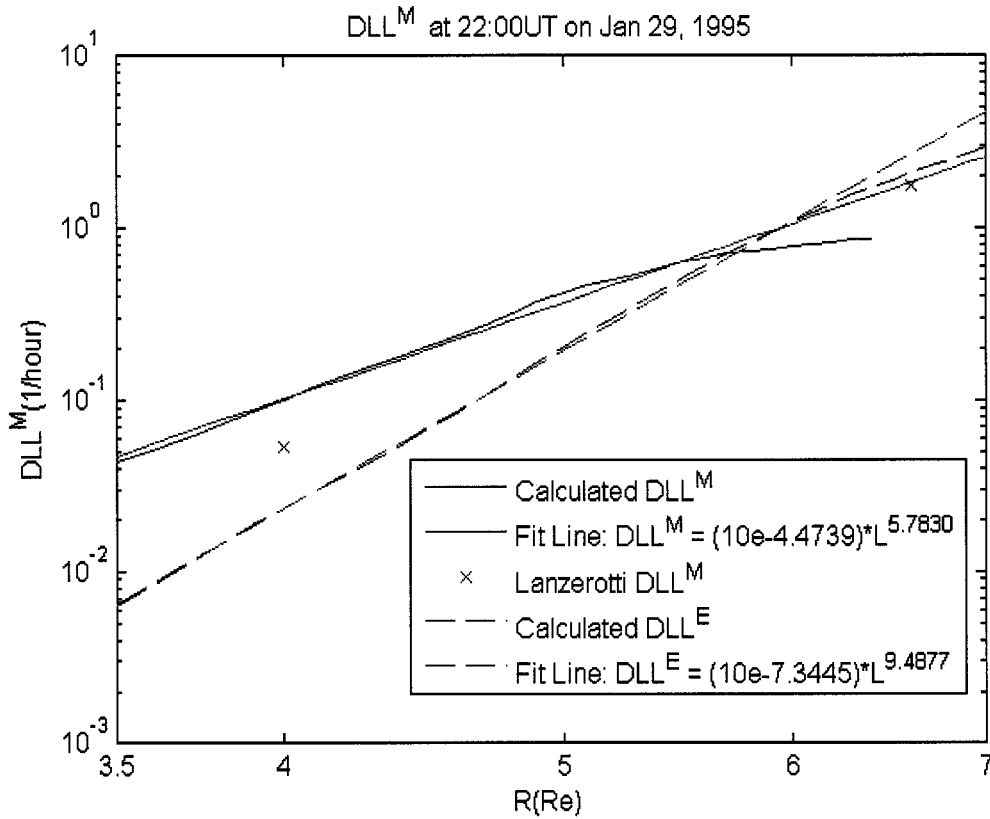
Figure 3.13 D_{LL}^E (dash blue line) and D_{LL}^M (solid blue line) at UT 22:00 on January 29, 1995

calculated using the ULF power from global LFM simulation. And the results are fitted into the

exponential function with base L (dash red line and solid red line).

In figure 3.14 the calculated diffusion coefficients are plotted at different times, corresponding

to different phases of the January 1995 storm (pre-storm, main phase and recovery phase). At UT

22:00 on Jan 29 (main phase, $Kp = 6$), the radial diffusion coefficients are 2-3 orders of

magnitude above the value at UT 15:00 on Jan 28 (pre-storm, $Kp = 1$). This increase is consistent with the *Brautigam* and *Albert* diffusion coefficients. During the recovery phase of the storm, D_{LL} values lie between the pre-storm and the main phase values. As described before, during the main phase of the storm event, D_{LL}^M dominates over D_{LL}^E for R<6 R_E. However, the pre-storm D_{LL}^E is a little larger than D_{LL}^M for all radial distance.
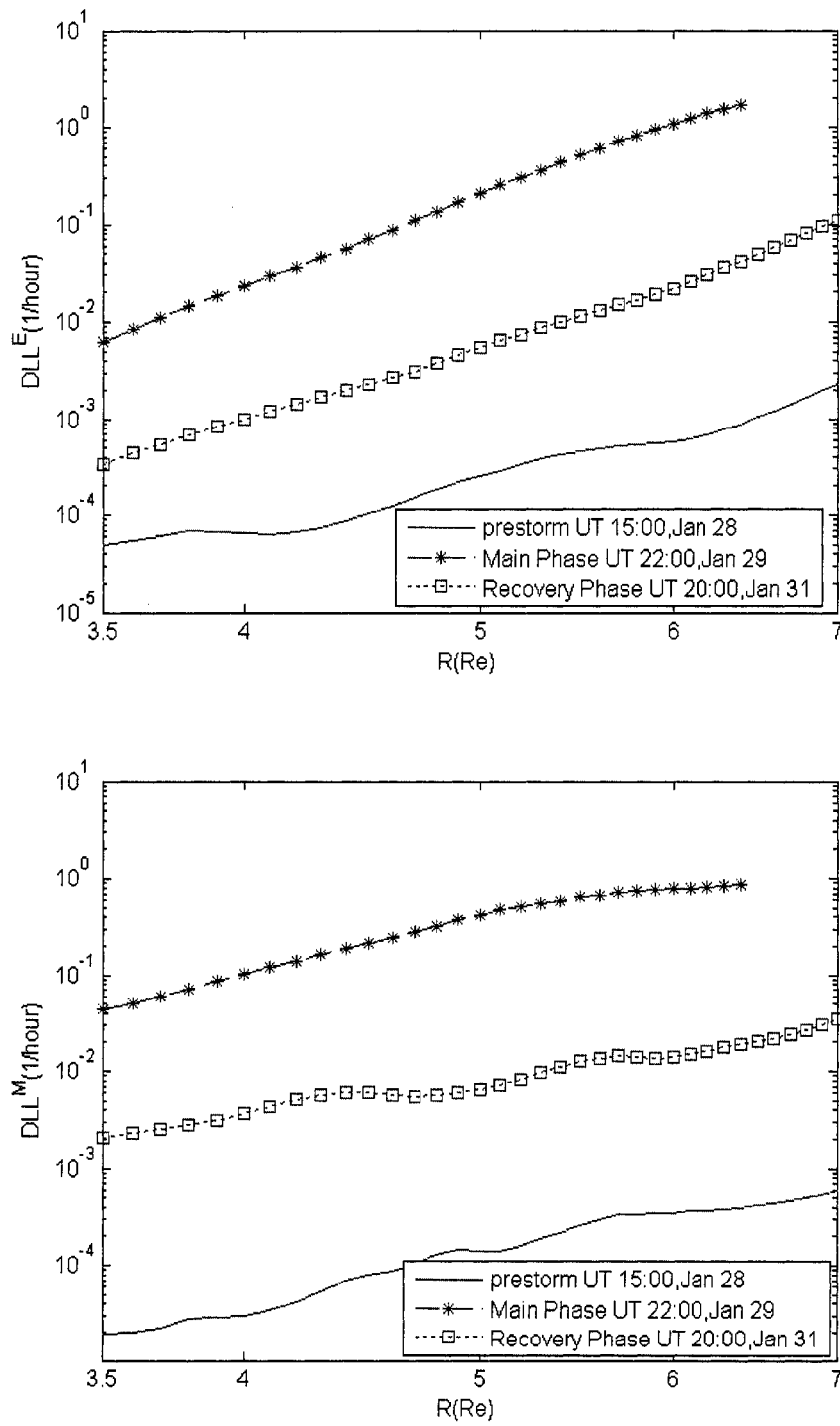
Figure 3.14 Calculated D_{LL}^E and D_{LL}^M at pre-storm, main phase and recovery phase of this storm.

3.9 Simulation results from radial diffusion model

As described in chapter two, we constructed a radial diffusion model that included dynamic boundary conditions and a time-dependent electron lifetime model. To test the validity of the diffusion coefficients calculated from the global MHD simulations in the previous section, we ran our radial diffusion model using these new diffusion coefficients and plotted the simulation results in figure 3.15.
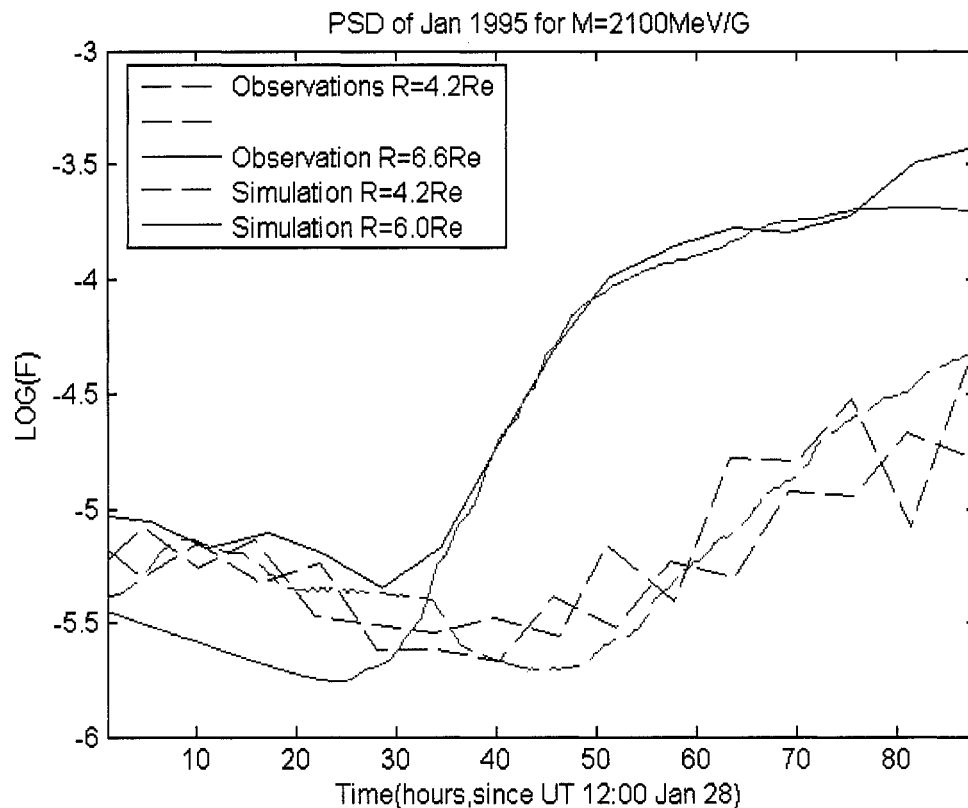
Figure 3.15 Simulated Phase space density from radial diffusion model using ULF-D_{LL} (red line) for the January 1995 storm event.

In this plot, we compare the simulated PSD to the observations and find that the simulated results capture the main features of the radiation belt observed during this storm event. Between

0 to 25 h, there was a decrease in PSD during the main phase of the storm at both R=6.6 R_E and R=6 R_E, in observations and simulations. Following that time, the simulated PSD at R=6.0 R_E began to increase quickly. This rise is due almost entirely to the rise in the PSD at R=6.6 R_E in the Li et al. [2001] model. At about t=45 h, the simulated PSD at R=4.2 R_E also began to increase slowly, which lasted through the rest time of the recovery phase.

During the main phase, the simulated PSD at R=6.0 R_E was slightly lower than the observations at R=6.6 R_E, but during most of the recovery phase, the simulated PSD is consistent with measurements.

The agreement between the simulated results from the radial diffusion model and the satellite observations indicates the radial diffusion coefficient calculated in section 3.7 is a good approximation of the radial transport rate for the January 1995 storm event.

3.10 Summary and discussion

In this chapter, we developed a method to simulate the radiation belt dynamics by coupling Nunn's algorithm [*Nunn*, 1993] with traditional MHD-Particle simulations. An important feature of our new method is that every test marker bears a special parameter, a weighted PSD, which is conserved along the trajectory of the particle. This feature enables us to simulate the boundary condition or lifetimes of particles easily by just resetting the weighted PSD and hence make more efficient use of these markers.

To test the performance of the new method, we compared the modeled PSD to satellite observations for the January 1995 high-speed-stream storm event. Good agreement was obtained between the simulation results and satellite measurements. Also, we quantified the effects of

dynamic boundary conditions and realistic decay lifetime of energetic electrons during this storm and found both terms are needed to reproduce the observed features.

Further, we calculated ULF wave power spectra from the global MHD simulation fields. The spectra for this moderate storm exhibit peaks during the main phase and the early recovery phase. These peaks are more pronounced around the time when the *Kp* index reached the maximum.

Then we converted the power spectra to radial diffusion coefficients according to the formulae derived by *Fei et al.* [2006]. The results show a less steep L-dependence than some previous formula of L^{10}. Considering the uncertainties involved, for example, the ignorance of the asymmetric diffusion coefficients, further research work needs to be done to improve this calculation.

Finally, we ran the radial diffusion model described in chapter two using the newly calculated diffusion coefficients for the high-speed-steam event. The simulated PSD is consistent with the measurements, which indicate the new diffusion coefficients provide an acceptable representation of radial transport rates during this storm.

In this research work, in order to simulate the injection of plasma sheet particles, we added new particles, which resulted in the diminution of statistical errors due to the severe magnetopause-loss events near the outer boundary. However, the difference between the simulated PSD over the outer boundary and GEO satellite observations indicated that adding new particles at one particular time can't completely remove statistical errors. A better solution to this problem is to couple our new radiation belt model with a plasma sheet model to simulate the external plasma source. An alternate method is to monitor all cells and add new particles into any empty cell, which is simpler but more time-consuming.

Finally, effects of the local acceleration by cyclotron resonances with whistle waves should be added to the simulations. It is interesting that reasonable agreement between simulations and observations has been obtained without modeling local acceleration, but this is just one storm and the GPS data is fairly noisy. Simulations should be carried out for more storms and with better GPS data and with data from more spacecraft (as for the upcoming Radiation Belt Storm Probe and ORBITALS missions).

References

Barker, A.B., Li, X., and Selesnick, R.S. (2005), Modeling the radiation belt electrons with radial diffusion driven by the solar wind, *Space Weather, Vol. 3*, S10003.

Bourdarie, S., R. H. W. Friedel, J. Fennell, S. Kanekal, and T. E. Cayton (1996), Magnetic storm modeling in the Earth's electron belt by the Salammbô code, *J. Geophys. Res., 101*, 27,171.

Brizard, A.J., Chan, A.A. (1999), Nonlinear relativistic gyrokinetic Vlasov-Maxwell equations., *Physics of Plasmas, 6(12)*, 4548.

Elkington S. R., Hudson, M. K. ,Wiltberger, M. J. , and Lyon, J. G. (2002), MHD/Particle simulations of radiation belt dynamics, *Journal of Atmospheric and Solar-Terrestrial Physics, 64*, 607.

Elkington, S.R., D.N. Baker, B. Yu, A.A. Chan, M. Wiltberger, and A. Aasnes (2006), *Injection of plasmasheet electrons into the radiation belts*. the 2006 Western Pacific Geophysics Meeting.

Fälthammar, C. G. (1965), Effects of Time-Dependent Electric Fields on Geomagnetically Trapped Radiation, *Journal of Geophysical Research, 70*, 2503.

Fedder, J. A., J. G. Lyon, S. P. Slinker, and C. M. Mobarry (1995a), Topological structure of the magnetotail as function of interplanetary magnetic field and with magnetic shear., *J. Geophys. Res., 100*, 3613.

Fei, Y., A. A. Chan, S. R. Elkiington, M. J. Wiltberger (2006), Radial diffusion and MHD-particle simulations of relativistic electron transport by ULF waves in the September 1998 storm. *J. Geophys. Res.*, in press.

Hudson, M., S. Elkington, J. Lyon, V. Marchenko, I. Roth, M. Temerin, J.B. Blake, M.S. Gussenhoven, and J. Wygant (1997), Simulations of radiation belt formation during storm sudden commencements, *J. Geophys. Res., 102*, 14087.

Li, X., I. Roth, M. Temerin, J. R. Wygant, M. K. Hudson, and J. B. Blake (1993), Simulation of the prompt energization and transport of radiation belt particles during the March 24, 1991 SSC, *Geophys. Res. Lett., 20*, 2423.

Mobarry, C., J. A. Fedder, and J. G. Lyon (1996), Equatorial plasma convection from global simulations of the Earth's magnetosphere, *J. Geophys. Res, 101*, 7859.

Nunn, D. (1993), A novel technique for the numerical simulation of hot collision-free plasma; Vlasov Hybrid Simulation, *Journal of Computational Physics, 108*, 180.

Schulz, M., and L. J. Lanzerotti (1974), *Particle Diffusion in the Radiation Belts*, Springer-Verlag, New York.

Shprits, Y. Y. R. M. Thorne, G. D. Reeves, and R. Friedel (2005), Radial diffusion modeling with empirical lifetimes: Comparison with CRRES observations, *Annales Geophys,* 23, 1467.

Vette, J. (1991), The AE-8 trapped electron model environment, National Space Science Data Center, Report 91-24, Greenbelt, Maryland.

Chapter 4

Summary and discussion

This thesis studies the variations of relativistic electron phase-space density (PSD) focusing on geomagnetic storms driven by high speed solar wind streams. This type of storm, also known as a CIR (corotating interaction region) storm, occurs more often in the descending phase of solar cycles and is characterized by a gradual initial phase, highly fluctuating IMF Bz, slow recovery phase and long-lasting fast plasma injections. Although CIR storms are usually weak or moderate, they can produce large sustained enhancement of radiation belt electrons. Therefore, compared to CME storms, CIR storms pose higher hazards to spacecraft and astronauts.

4.1 Radial Transport Model

In chapter two, we first constructed a time series of solar wind and magnetospheric parameters to represent a typical high-speed-stream model storm based on the schematic sketch presented by *Tsurutani et al.* [1995] and on typical numerical values from storm events between 1995 and 1996 from *Hilmer et al.* [2000].

Second, we developed a radial transport model with a time-dependent radial diffusion coefficient from *Brautigam and Albert* [2000], time-dependent geosynchronous orbit boundary conditions from *Li et al.* [2001], and a *Kp*-dependent loss term. The Hilmer-Voigt magnetic field model was used to calculate the phase space density from fluxes on the equatorial plane. Using the radial diffusion model, we simulated the dynamics of outer radiation belt electrons during the high-speed-stream events. Two particular events, the January 1995 storm event and the July 1995 storm event, were studied in detail. The simulated results are qualitatively consistent with

the measurements by the GEO and GPS satellites and show that inward radial diffusion can propagate the variations of PSD from the outer boundary into the inner magnetosphere. However, the growth rates of the modeled PSD at R=4.2 R_E for both cases are slightly larger than observed values, suggesting that the Brautigam-Albert formula for D_{LL} may overestimate the radial diffusion rate for high-speed-stream events.

Furthermore, we extended the calculation of the growth rates of PSD at R=4.2 R_E to several "typical" high-speed-stream events between 1995 and 1996. Compared to the measured radial diffusion rates reported by *Hilmer et al.* [2000], the results show again that decreasing the Brautigam-Albert diffusion coefficient produces better agreement between simulation results and observations.

Third, we investigated the sensitivity of our radial transport model to the underlying magnetic field model by repeating the simulations using the Tsyganenko 2001 magnetic field model and a dipolar magnetic field. The major differences in the simulated results for the three magnetic field models occur during the main phase and early recovery phase of the model storm, and are most likely due to the differences in the ring currents of the three magnetic field models.

Fourth, we ran our radial diffusion model for the January 1995 and July 1995 events, with actual solar wind input and measured radial diffusion coefficients [*Lanzerotti and Morgan*, 1973; *Lanzerotti et al.*, 1978]. The simulated results indicated that using both solar wind drivers and measured radial transport rates can partly remove the discrepancy between the modeled and measured PSD.

The model calculated the fluxes of equatorial-mirroring particles. However, the GEO and GPS spacecraft actually measured the omni-directional fluxes. Using the assumption of an

isotropic pitch-angle distribution, we calculated the errors due to pitch angle assumptions. The errors for a dipolar magnetic field and the Hilmer-Voigt magnetic field are respectively 9% and 15%. Considering the general imprecision of the comparisons due to the wide energy range of the GPS particle detectors, the errors are relatively small.

4.2 MHD-Particle simulation

Chapter three began with the introduction of a new algorithm, which is adapted from *Nunn*'s Vlasov Hybrid Simulation (VHS) method and has the advantage of making more efficient use of test particles. The critical idea of the new method is that every marker is assigned "phase space density" and will conserve the PSD along its trajectory. Then at each time step, the PSD at fixed grid points can be integrated from the PSD of the markers within the nearest cells according to an area weighting algorithm. Coupling the new method with an MHD-Particle code developed by *Elkington* [2002], the computational performance can be greatly enhanced. As an added bonus, the dynamic boundary conditions and loss lifetime of electrons can be easily realized by resetting the PSD of relevant markers.

The January 1995 storm event, a typical high-speed-stream event, was used as a test case in this work. The analysis of the MHD-Particle simulation results highlighted severe magnetopause-loss events in the early period of January 29, 1995. During that time, MHD simulation results showed a large compression on the day side of the magnetic field and most particles outside R=6 R_E were lost. First, we ran this MHD-Particle radiation belt model using free boundary conditions without any pitch-angle diffusion loss. The simulation results showed that the inward diffusion of pre-existing particles resulted in a slight increase of the PSD at

R=4.2 R_E. However, the simulated result could not reproduce the feature of the long-time increase at R=4.2 R_E during the recovery phase observed by GPS satellites. At R=6.6 R_E, the PSD measured by GEO satellites had a drop out during the main phase and a quick, large enhancement during the recovery phase. On the contrary, our simulated PSD at R=6.6 R_E decreased continuously throughout the whole storm event.

Considering the inaccuracy of free boundary conditions, we used the dynamic boundary conditions measured by GEO satellites. The new simulated results were consistent with the observations except for a discrepancy at R=4.2 R_E during the main phase. Moreover, we found that adding a finite lifetime module based on the measured decay lifetime [*Meredith et al.*, 2006] can help remove the discrepancy. Therefore, we can conclude that both the dynamic boundary conditions and a good loss lifetime model are important to reproduce the dynamic variations of energetic electrons for this storm event.

Spectral analysis of the MHD fields for this storm event indicates a significant temporal increase of the ULF wave power during the main phase. We calculated radial diffusion coefficients from the power spectra of the global MHD fields. The value of the radial diffusion coefficients reached a peak around the time when *Dst* was minimum and *Kp* arrived at the maximum value. The maximum radial diffusion coefficients were 2~3 orders of magnitude higher than the pre-storm values. The radial diffusion coefficients during the recovery phase lie between the pre-storm values and main-phase values. Furthermore, we approximated the radial diffusion coefficients during the main phase in a power-law form $D_0 L^n$. We found the

L-dependence of the magnetic diffusion coefficient is less steep than the Brautigam-Albert formula of D_{LL}^M and more consistent with the observational results of *Lanzerotti and Morgan* [1973] and *Lanzerrotti et al.* [1978].

Finally, to test the accuracy of the calculated diffusion coefficients, we reran our radial transport model with the new diffusion coefficients and adjusted initial distribution functions. Good agreement between the simulation results and observations proved the new radial diffusion coefficients are good approximations of the radial transport rates for the January 1995 storm.

4.3 Future work

This research work suggests that the radial diffusion process play a significant role in transporting the energetic particles from near synchronous orbit to GPS satellite locations during high-speed-stream storm events. We note that recent observations [*Chen et al.*, 2006; *O'Brien et al.*, 2003] indicate that another acceleration mechanism, local acceleration, may also be very important for large increases of electron fluxes at the center of the outer radiation belt. Through interaction with VLF waves, the electrons within geosynchronous orbit may be locally accelerated to relativistic energies. Coupling our radial diffusion model with the local acceleration sources presents the natural extension of this work.

Our research work focused on the study of CIR-driven storms. However, the CME-driven storms are also very important. Although the highest prolonged fluxes of energetic electrons are predominantly associated with the CIR storms, CMEs can drive extreme storms, which also result in the formation of strongly enhanced radiation belts. Using our model to study the dynamics of radiation belt during CME storm events can be another promising future work.

In our new MHD-Particle model, we added new markers to remove statistical error and to better model the phase space density near the outer trapping boundary. Coupling a good plasma sheet model with our MHD-Particle codes would be a useful extension of the model to better simulate plasma sheet sources of energetic particles.

Modeling radiation belt variations can greatly improve our understanding of radiation belt physics and also provide a basis for the prediction of global space weather. As space exploration advances, a global, dynamic and realistic radiation belt model is forthcoming.

Appendix A

The calculation of the Roederer L value

As described in chapter one, the Roederer L value can be defined as:

$$L^* = \frac{2\pi\mu_E}{\Phi R_E}.$$

Here μ_E is the earth's magnetic moment and can be assumed to be constant for the time scale we are interested in; Φ is the magnetic flux enclosed by the drift shell of particles.

Therefore, integration of the magnetic flux along the drift shell is of critical importance to the calculation of Roederer L. However it is usually not practical to directly calculate the magnetic fluxes enclosed by the drift path. Instead, we calculate the magnetic flux outside the drift shell since the divergence of magnetic field equals zero. In our radial diffusion model, we only consider the equatorially-mirroring particles, i.e., particles with pitch angle of 90^0. Hence, assuming no external electric fields and constant magnetic moment, these particles drift on the equatorial plane along the contour of constant B.

Furthermore, it is usually more convenient to trace the magnetic field line from the equatorial plane to the surface of the earth and calculate the magnetic flux over the surface of the earth.

Figure A.1 plots the drift shell of equatorially trapped particles in the geomagnetic field. Solid lines are the contours of constant radial distances, and blue dot symbols depict the electron drift shell; noon is at 0 degree and 180 degrees correspond to midnight. From this plot, the trajectories of the electrons are symmetric near the earth. In the outer magnetosphere, due to the compression of the dayside magnetic field by the solar wind stream, the drift path is asymmetric and closer to the earth at the night side.
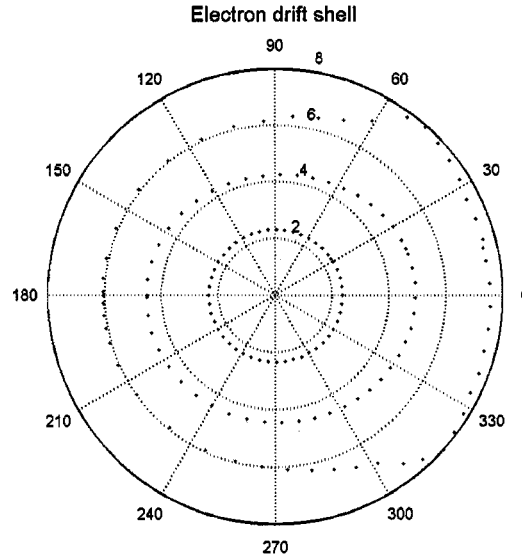
Figure A.1 Electron Drift Shell in the Hilmer-Voigt magnetic field.

Once we integrate the magnetic flux enclosed by the drift shell, Roederer L values

can be easily calculated according to the definition equation. The variations of the L values

during the September 1998 storm event are shown in Figure A.2. The L value vs. R at midnight

for a dipolar magnetic field is plotted as the red line, which is a straight line since in a dipolar

magnetic field, L is equal to the radial distance in units of R_E. The two blue dot lines denote the

L values calculated from two magnetic models: the Tsyganenko 2001 model (T01) and the

Hilmer-Voigt magnetic model (MSM).

The top panel of Figure A.2 plots the L values at UT 22:00 on September 24, 1998, which

corresponded to the pre-storm period. The L values for the Hilmer-Voigt magnetic model are

smaller than the values for the Tsyganenko 2001 model, which indicates the Tsyganenko 2001

model has a weaker ring current during quiet time.
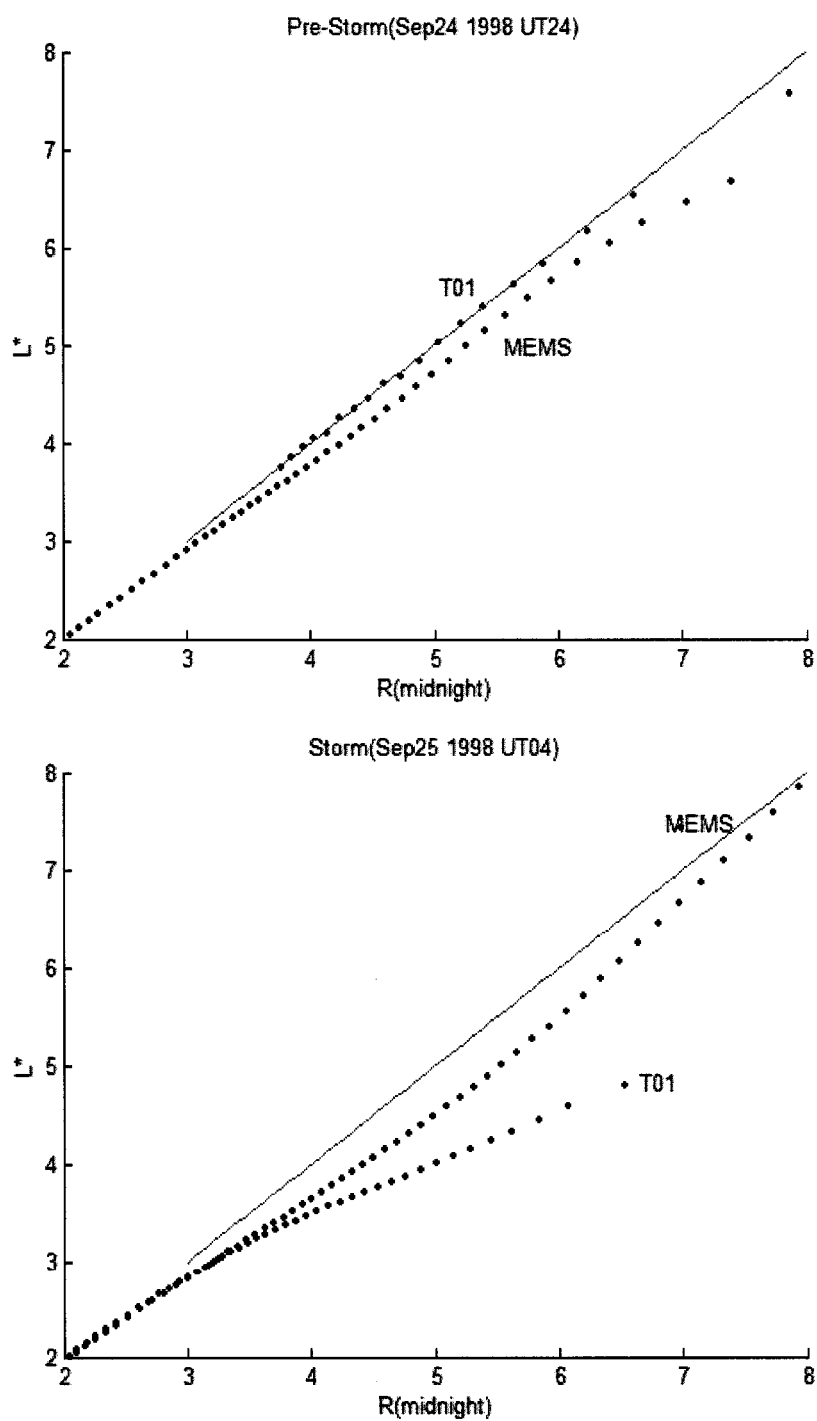
Figure A.2 The variations of L value during September 1998 storm event for different field models.

However, during the main phase of the storm, at UT 4:00 on September 25, 1998, both L

values for the T01 model and for the H-V model are smaller than the values of quiet time

because during the main phase, the intensification of the ring current leads to the decrease of the

magnetic field near the earth. The Tsyganenko 2001 model displays a larger decrease in L value

than the Hilmer-Voigt magnetic field model at large radial distance, which is consistent with the

discussion in section 2.4.4.

Appendix B

## Space Weather Modeling Framework (SWMF)

The term "Space Weather" refers to solar activity and its impact on the earth's magnetosphere.

As described in chapter one, our technology systems are vulnerable to solar activity. Recently,

with humanity's increasing dependence on these technologies, forecasting space weather has

become a central topic of the space science.

In order to deal with the impact of solar activity on our society, several government agencies

launched a national space weather program, which is aimed at providing a predictive and

physical-based space weather model. Under the cooperation of a number of groups in several

universities, a high-performance global model, Space Weather Modeling Framework, has been

developed which is divided into nine physics domains: Solar Corona, Eruptive Event Generator,

Inner Heliosphere, Solar Energetic Particles, Global Magnetosphere, Inner Magnetosphere,

Radiation Belt, Ionosphere Electrodynamics, and Upper Atmosphere. The structure of the

framework is illustrated in figure B.1.
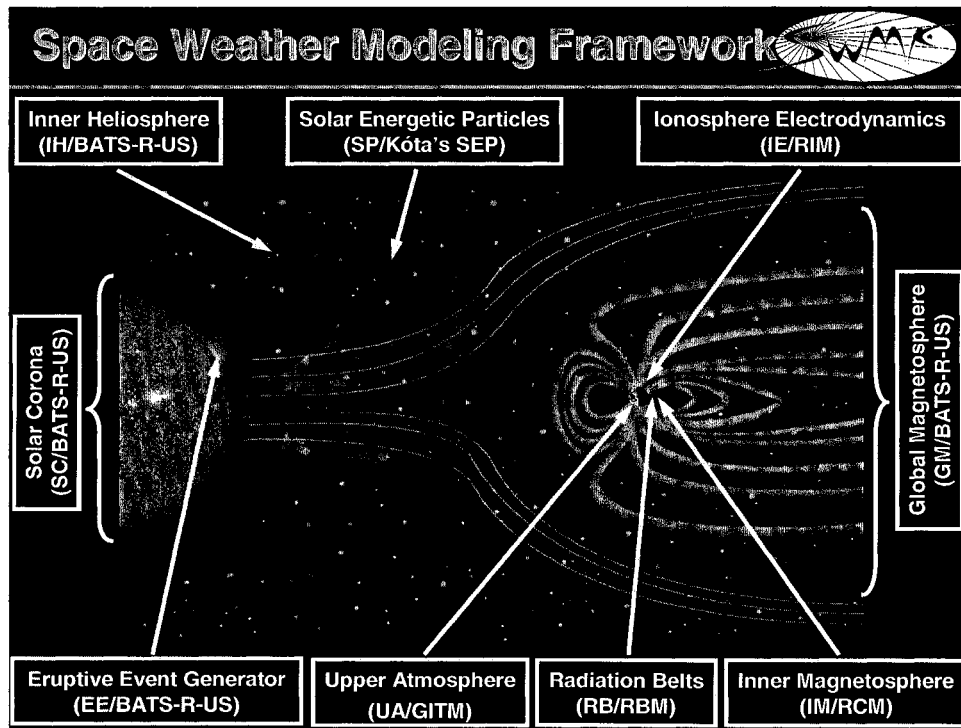
Figure B.1 Illustration of Space Weather Modeling Framework [*JiChun Zhang,* 2006].

Our main contribution to this project is to build the radiation belt model described in chapter two and couple it into the framework. Modeling the radiation belt is one important part of global space weather modeling since the variations of the outer radiation belt have direct and important effects on our society. Within the framework, the coupled the global MHD field model (BATS-R-US) and the Rice Convection Model (RCM) provide the underlying magnetic field for our radiation belt model. In the next part, we will present the simulation result of our radiation belt model with the coupled BATS-R-US/RCM magnetic field model for a small storm event.
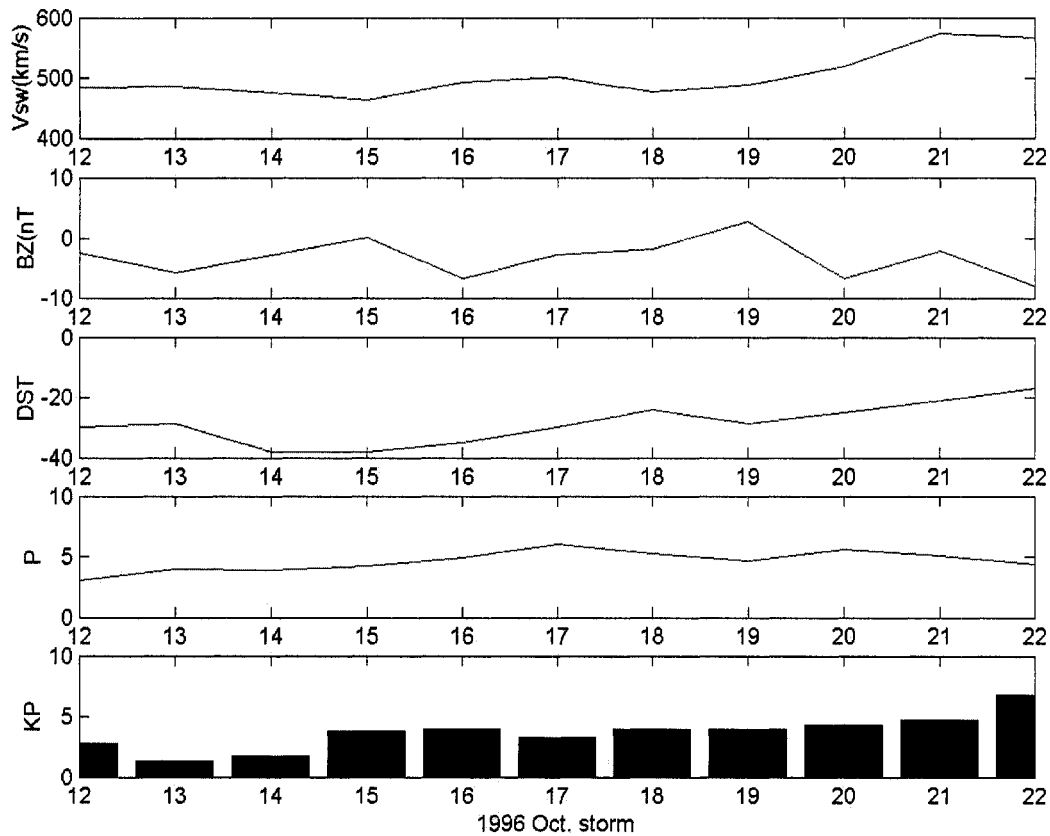
Figure B.2 Solar wind conditions and magnetic indices from UT 12:00 to UT 22:00 on October 22, 1996.

We selected a small storm event on October 22, 1996 as the test case. Figure B.2 shows the hourly averages of the solar wind data and magnetic indices for this event. The minimum value of the Dst index was around -40 at UT 14:00, which indicates it is a small storm event. During most time of the storm event, IMF Bz stayed southward. Between UT 18:00 and UT 21:00, the velocity of the solar wind stream increased slowly from 500 km/s to 580 km/s. The corresponding variations of L values are plotted in Figure B.3, which is calculated from the global MHD BATS-R-US field.
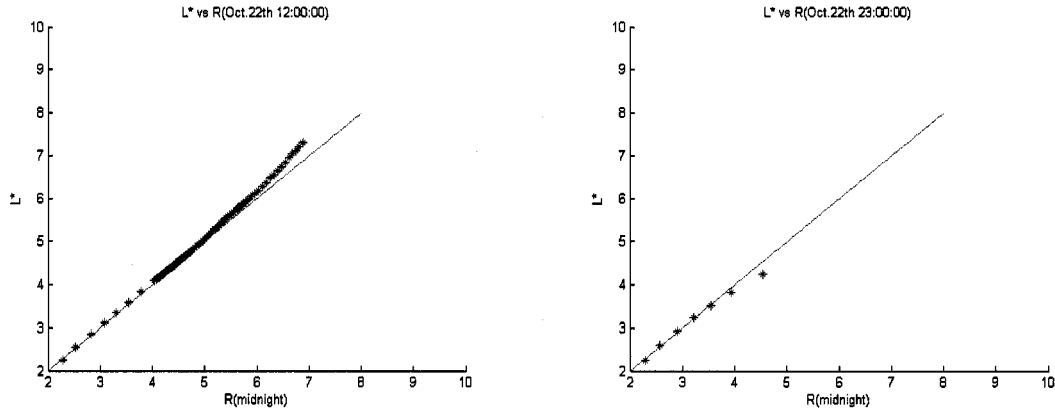
Figure B.3 The L values vs. radius at midnight at UT 12:00 and UT 23:00 on October 22, 1996.

The left panel of figure B.3 shows the L value is higher than the radial distance at midnight, which is expected since the MHD field has a weak ring current and the effects of magnetopause and tail current are dominant. From the right panel, the L value is equal to or slightly smaller than the radial distance due to the build up of the ring current during the storm time.
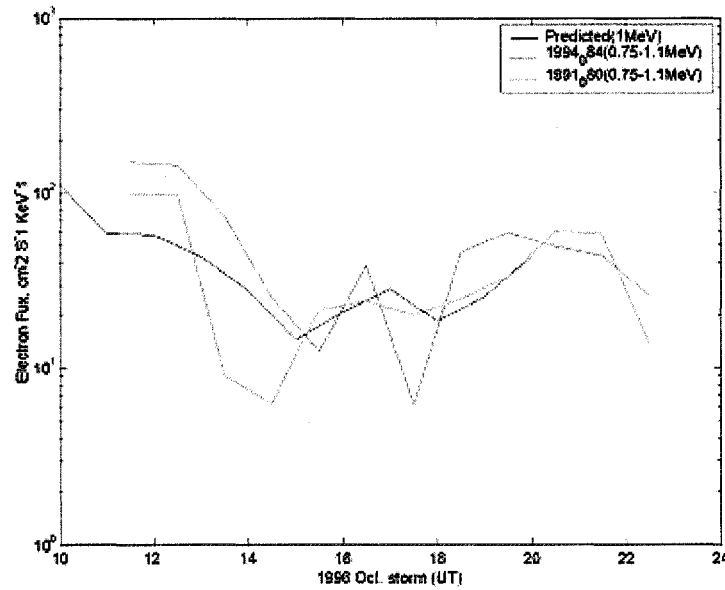
Figure B.4 The comparison of simulated fluxes (blue curve) with satellite observations (red and green curves) during the October 1996 storm event.

The simulated flux for 1 MeV electrons is represented in figure B.4 and compared with satellite observations. From this graph, we found the simulated result is quantitatively comparable to the observations, which indicated the success of the framework in predicting the flux changes for this small storm event. However, to test the ability of SWMF in forecasting space weather, we need to simulate more storm events and compare the model results with the measurements.